



UNIVERSIDAD NACIONAL AUTÓNOMA DE MÉXICO
POSGRADO EN CIENCIA E INGENIERÍA DE LA COMPUTACIÓN

**DEFORMABLE MODELS FOR MEDICAL IMAGE SEGMENTATION BASED
ON LOCAL ANALYSIS**

T E S I S

QUE PARA OPTAR POR EL GRADO DE
DOCTORA EN CIENCIAS (COMPUTACIÓN)

P R E S E N T A
JIMENA OLVERES MONTIEL

DIRECTOR DE TESIS: DR. BORIS ESCALANTE RAMÍREZ
POSGRADO EN CIENCIAS E INGENIERÍA DE LA COMPUTACIÓN
CIUDAD UNIVERSITARIA, CDMX NOVIEMBRE 2017



Universidad Nacional
Autónoma de México

Dirección General de Bibliotecas de la UNAM

Biblioteca Central



UNAM – Dirección General de Bibliotecas
Tesis Digitales
Restricciones de uso

DERECHOS RESERVADOS ©
PROHIBIDA SU REPRODUCCIÓN TOTAL O PARCIAL

Todo el material contenido en esta tesis esta protegido por la Ley Federal del Derecho de Autor (LFDA) de los Estados Unidos Mexicanos (México).

El uso de imágenes, fragmentos de videos, y demás material que sea objeto de protección de los derechos de autor, será exclusivamente para fines educativos e informativos y deberá citar la fuente donde la obtuvo mencionando el autor o autores. Cualquier uso distinto como el lucro, reproducción, edición o modificación, será perseguido y sancionado por el respectivo titular de los Derechos de Autor.

© 2017 – *Jimena Olveres Montiel*

– *All rights reserved.*

– *Todos los derechos reservados.*

Agradecimientos

A mi familia: Raul, Ana Valeria y Ella Amber Santoyo quienes siempre estuvieron a mi lado y a quienes les agradezco su comprensión, confianza y cariño durante estos años. A mi tía Sylvia y mi madre Mercedes Montiel, quienes sin su ayuda hubiese sido muy difícil continuar hasta el final.

A mi tutor el Dr. Boris Escalante quien le debo el acompañamiento y su apoyo, así como la creencia en que iba a cumplir mi meta. Muchas gracias doctor por dejarme ser parte de LaPI.

A mis amigos y compañeros de trabajo en LaPI, con quienes aprendí al convivir en el día a día: Erika, Vivian, Erik, German, Sonia, Uriel, Leiner, Lorena, Alfonso, Ernesto, Jorge y todos los demás que conocí y que aún se encuentran trabajando dentro del mismo, así como a Benjamín Gutiérrez, Verena, Cinthya, Zian, Sergio y mis compañeros del Posgrado, de quienes pude contar con su opinión enriquecedora.

A mis sinodales la Dra. Katya Rodríguez, Dr. Fernando Arámbula, Dr. Enrique Vallejo y Dr. Pablo Pérez quienes me orientaron durante el doctorado y mis evaluaciones, gracias a sus recomendaciones y comentarios.

Al Posgrado en Ciencia e Ingeniería de la Computación, en especial a Lulu, Amalia y Cecilia quienes siempre me ayudaron a resolver situaciones académicas y que también me impulsaron a ver más allá del posgrado.

También agradezco a CONACYT y a los proyectos PAPIIT IN116197 y el SECITI 110/2015, por los apoyos económicos.

Modelos Deformables para Segmentación de Imágenes Médicas basada en Análisis Local

Resumen

Las imágenes médicas son adquiridas a través de diferentes modalidades y una de las tareas más importantes a realizar, cuando se analizan estas imágenes, es la de obtener información anatómica.

Normalmente estas imágenes poseen diferencias particulares como son resolución espacial, ruido o contraste por nombrar algunas, que pueden hacer de la segmentación una tarea complicada. El análisis de imágenes médicas, especialmente al segmentar estructuras, generalmente requiere la evaluación del especialista, para el cual la tarea de segmentación suele volverse tediosa y en consecuencia resultar con inexactitudes.

Este esfuerzo se puede mejorar con el apoyo de herramientas automatizadas. Por esta razón, el área de segmentación automática de imágenes médicas se ha vuelto un soporte para la toma de decisiones, tanto para diagnóstico como para el tratamiento de enfermedades. Es por esto que han surgido múltiples técnicas, siendo mejoradas constantemente, en búsqueda de una mayor precisión. Sin embargo, la segmentación automatizada de estructuras anatómicas aun permanece como una tarea de diversas soluciones.

La presente tesis estudia algoritmos conocidos de segmentación de imágenes médicas, los cuales mejoran al incluirse en ellos descriptores de textura, como los que otorgan la transformada de Hermite y las diferentes modalidades de Patrones Binarios Locales. Esta información se incluye combinándolos con modelos deformables de segmentación, tal es el caso de los Modelos Activos de Forma y los modelos basados en Conjunto de niveles (Level sets).

La decisión de utilizar la transformada de Hermite es debido a que es una herramienta matemática útil para el análisis y síntesis de datos. Ésta se basa en el uso de descriptores que modelan los campos receptivos del Sistema de Visión Humano, además de ser direccionalmente orientada. Se realizan comparaciones con los métodos tradicionales. Los resultados son evaluados en imágenes de mesencéfalo de Resonancia Magnética, y en imágenes de ventrículo de corazón de Tomografía Computarizada.

Palabras clave: Segmentación, modelos deformables, imágenes médicas, Transformada de Hermite, descriptores de textura.

Deformable Models for Medical Image Segmentation based on Local Analysis

Abstract

Medical images can be acquired through different techniques (modalities). And one of the most important tasks when analyzing images, is to obtain the anatomic information. Usually, images have differences as spatial resolution, noise, contrast, among others. The analysis of medical images and specially when segmenting structures, often requires the evaluation of the specialists and its segmentation can be a tedious task resulting into some inaccuracies.

With support from automated tools this effort can be improved. For this reason, results obtained from automatic medical image segmentation have proved useful for decision making as well as for diagnosis and treatment of diseases. Therefore multiple techniques have emerged and been improved constantly, searching for better precisions. However automatic segmentation of anatomical structures still remains a challenging task with no general and unique solution.

In this thesis, known segmentation algorithms for medical images are improved by texture descriptors introducing directional-oriented Hermite transform and different modalities of Local Binary Patterns; they are applied on deformable models such as Active Shape Models and deformable models based on Level sets.

The choice of the Hermite transform as a mathematical tool for data analysis lies in the fact that it uses features that have been proposed to model the profiles of the receptive fields, present in the Human Visual System. A comparison with the traditional methods is included. And the evaluation is done on magnetic resonance images for midbrain and computer tomography images for heart ventricle.

Keywords: Segmentation, deformable models, medical images, Hermite Transform, texture descriptors.

Contents

| | Page |
|---|-------------|
| 1 Introduction | 1 |
| 1.1 Motivation | 1 |
| 1.2 Objective of this work - Organization and outline | 2 |
| 2 Active contours and Deformable Models | 3 |
| 2.1 Active Shape Models | 4 |
| 2.2 Level sets | 7 |
| 2.2.1 Fast Level Sets | 9 |
| 3 Hermite's Local Information | 13 |
| 3.1 Local Analysis by Perceptual based models | 13 |
| 3.2 Hermite Transform | 14 |
| 3.3 Hermite as local information | 15 |
| 4 Midbrain volume segmentation | 17 |
| 4.1 Introduction | 17 |
| 4.2 Local binary patterns | 18 |
| 4.3 Materials | 21 |
| 4.4 Proposed Method | 21 |
| 4.5 Experimental results | 22 |
| 4.6 Remarks | 26 |
| 5 Heart's left ventricle segmentation based on active contours | 31 |
| 5.1 Texture descriptor approaches to level set segmentation in medical images | 33 |
| 5.1.1 The combined proposal | 34 |
| 5.1.2 Other Texture descriptors | 35 |
| 5.1.3 Materials | 36 |
| 5.1.4 Experiments and results | 37 |
| 5.1.5 Final Comments | 38 |
| 5.2 Contour-based Hermite segmentation of heart's left ventricle | 51 |
| 5.2.1 Combining active shape models with LBPs and HCs | 51 |
| 5.2.2 Combining fast level sets with HCs | 55 |
| 5.2.3 Materials | 57 |
| 5.2.4 Experimental results | 57 |
| 5.2.5 Discussion | 63 |
| 6 A perspective on the study of Heart failure | 67 |
| 6.1 Volume segmentation over the whole left ventricle. | 68 |

- 6.2 Motion estimation of segmented ventricle 68
- 6.3 Heart Failure example 70
- 7 Conclusions** **73**
- A Appendix** **77**
- A.1 Ray Feature error 77
- A.1.1 Metric Comparison 78
- Bibliography** **81**

List of Figures

| | Page |
|--|------|
| 2.1 (a) ASM Training Shapes and creating Point Distribution Model of the left ventricle in CT. | 5 |
| 2.2 ASM Adjustment in the search phase. | 6 |
| 2.3 Curve propagation in normal direction. | 7 |
| 2.4 Representation of a boundary in the fast level set method. | 10 |
| 3.1 (a) Ensemble of spatial Hermite filters (left) and their corresponding frequency responses (right). The displayed orders go from $N = 0$ to $N = 4$ | 15 |
| 3.2 Cartesian (left) and steered Hermite coefficients (right). Note that most of the coefficient energy is concentrated in the upper row of the steered Hermite coefficients. | 16 |
| 4.1 Midbrain positioned within the human brain. Picture taken from "The Brain Muse spring 2430 lecture 15 7/12/10", http://slideplayer.com/slide/7375938/ | 18 |
| 4.2 Description of the Local Binary Pattern method | 19 |
| 4.3 Two different ways to combine LBPs with ASMs. (a) LBP's histogram for each profile landmark of the contour; and (b) Quadratic LBP's histogram for each contour landmark. | 22 |
| 4.4 Cranial MR images; the first row shows axial original view and second row shows binary midbrain segmentation; binary images were augmented 2X for a better visualization. (a) expert annotated boundary; and (b) classic ASM recognized boundary; the red contour in binary image indicates the expert boundary. | 26 |
| 4.5 Profile ASM/LBP scheme midbrain segmentation; binary images were augmented 2X for a better visualization. The red contour indicates the expert boundary. (a) ASM/LBP; (b) ASM/LBPuni; (c) ASM/LBPnum; and (d) ASM/LBPmed | 27 |
| 4.6 Quadratic ASM/LBP scheme midbrain segmentation; binary images were augmented 2X for a better visualization. The red contour indicates the expert boundary. (a) ASM/LBP; (b) ASM/LBPuni; (c) ASM/LBPnum; and (d) ASM/LBPmed | 27 |
| 4.7 Segmentation over multiple midbrain slices. | 28 |
| 4.8 ASM/LBP scheme, that does not converge correctly. | 28 |
| 5.1 CT image of the heart displayed using the short axis view where it is possible to see the right and left ventricles. The red ellipse defines the endocardium, whereas the blue ellipse defines epicardium. This segmentation resembles typical boundaries drawn by clinicians. | 32 |
| 5.2 Based on a circular mask, the LBP algorithm computes comparisons between a central pixel and its surrounding neighbors. In this example, the central value is $p_c = 10$ and the final label is 9. | 36 |

5.3 BRINT averages the sampling points around a central pixel before binarization. First, It transforms the original neighborhood (P=24) into a new one (P=8) by averaging the 3 adjacent neighbors to generate a binary pattern. 37

5.4 Segmentation comparisons between a manual contour (blue) and the level set method (red) using: GRAY (**first row**), Hermite3 + GRAY (**second row**), Hermite5 + GRAY (**third row**), Hermite9 + GRAY (**fourth row**), and LBPU + GRAY (**fifth row**). The numbers on the images indicate the percentage of the cardiac cycle. . . 39

5.4 Continuation... Segmentation comparisons between a manual contour (blue) and the level set method (red) using: LBPUM + GRAY (**first row**), BRINT + GRAY (**second row**), Image derivatives + GRAY (**third row**), and Hounsfield values + GRAY (**fourth row**). The numbers on the images indicate the percentage of the cardiac cycle. 40

5.5 Left ventricle volume comparison against manual contour (blue). Each column belongs to a different patient. The method (red) is: GRAY. 42

5.6 Left ventricle volume comparison against manual contour (blue). Each column belongs to a different patient. The method (red) is: Hermite3 + GRAY 43

5.7 Left ventricle volume comparison against manual contour (blue). Each column belongs to a different patient. The method (red) is: Hermite5 + GRAY 44

5.8 Left ventricle volume comparison against manual contour (blue). Each column belongs to a different patient. The method (red) is: Hermite9 + gray 45

5.9 Left ventricle volume comparison against manual contour (blue). Each column belongs to a different patient. The method (red) is: LBPU + GRAY 46

5.10 Left ventricle volume comparison against manual contour (blue). Each column belongs to a different patient. The method (red) is: LBPUM + GRAY 47

5.11 Left ventricle volume comparison against manual contour (blue). Each column belongs to a different patient. The method (red) is: BRINT + GRAY 48

5.12 Left ventricle volume comparison against manual contour (blue). Each column belongs to a different patient. The method (red) is: Image derivatives + GRAY. . . 49

5.13 Left ventricle volume comparison against manual contour (blue). Each column belongs to a different patient. The method (red) is: Hounsfield values + GRAY. . . 50

5.14 Overview of the experiments conducted in this study. First, feature extraction is performed and then incorporated into ASMs method to improve segmentation of cardiac walls. The assessment is conducted with three metrics: Hausdorff, Dice, and, Ray Feature error. 51

5.15 Overview of the experiments conducted in this study. First, feature extraction is performed and then incorporated into LS method to improve segmentation of cardiac walls. The assessment is conducted with three metrics: Hausdorff, Dice, and, Ray Feature error. 52

5.16 Metric of compactness. The blue numbers indicate the compactness value. A value of 1 means that the shape of the object is closer to a circle. During this step, the object with the largest compactness value is retained. 52

5.17 Two different techniques to combine ASMs and LBPs. (a) For every landmark, the LBP histograms are computed on all points of the corresponding profile of length n . (b) Quadratic-LBP histogram computes LBPs on four square regions of 5×5 pixels around each landmark, then a histogram is built by concatenating the four local histograms one after another. 54

| | | |
|------|---|----|
| 5.18 | ASM/Profile-HCs scheme. The diagram shows the construction of the histograms for each landmark. For a given point in a profile, the four histograms of the corresponding Hermite coefficients are concatenated. | 55 |
| 5.19 | ASM/Quadratic-HCs scheme. The diagram shows the construction of the histogram. For a given point, four regions around a landmark are computed. This procedure is performed on every Hermite coefficient. | 56 |
| 5.20 | Segmentation details. Ground-truth boundary (red), experimental segmentation (blue). The best segmentation cases for (a) ASM/QHCs on the epicardium and (b) FLS/HCs on the endocardium. Papillary muscles are delineated on yellow. | 58 |
| 5.21 | Plots depict the performance of FLS and FLS/HCs endocardium segmentation against the number of iterations measured with Dice index (upper row) and Ray Feature error (lower row). Dice index is between 0 and 1, values close to 1 indicate similar contours. Ray Feature error is between 0 and 1; values close to 0 indicate similar contours. The values were taken during (a) 0%, (b) 60%, (c) 20%, and (d) 90% of the cardiac cycle. | 60 |
| 5.22 | Average distances between the experimental and the expert contours with Hausdorff distance (lower values indicate more alike boundaries), Dice coefficient (values close to 1 indicate more similar contours) and Ray Feature error (values close to 0 indicate more similar contours) for endocardium segmentation. X-axis represents the percentages of the cardiac cycle (diastole-systole). | 61 |
| 5.23 | Average distances between the experimental and the expert contours with Hausdorff distance (lower values indicate more alike boundaries), Dice coefficient (values close to 1 indicate more similar contours) and Ray Feature error (values close to 0 indicate more similar contours) for epicardium segmentation. X-axis represents the percentages during the cardiac cycle (diastole-systole). | 62 |
| 5.24 | Final segmentations of endocardium (red) using FLS/HCs method, epicardium (blue) using ASM/QHC method, and papillary muscles (yellow) throughout the cardiac cycle. | 63 |
| 5.25 | Comparison of segmentation results between FLS (upper row) and FLS/HCs (lower row) on the endocardium (red contour) adding Gaussian noise with zero mean and increasing variances (var). | 64 |
| 6.1 | Volume segmentation of endocardium (red) and epicardium (blue) in (a) and only the endocardium in (b) using FLS/HCs. | 69 |
| 6.2 | Motion estimation in one cardiac cycle going from systole to diastole. | 71 |
| 6.3 | Segmentation of endocardium (red), epicardium (green) and papillary muscles (yellow) of a patient with infarction, using FLS/HCs at different percentages of the cardiac cycle. | 71 |
| 6.4 | Segmentation of cardiac muscle with overlaid motion estimation, going from systole to diastole. | 72 |
| A.1 | Ray Feature error (RFE). Given two closed overlapping objects, RFE measures similarities between them by computing and adding E_θ with $\theta = \{0, \dots, 2\pi\}$ | 78 |
| A.2 | Two examples of segmentation. Bold values represent the best results and letters in parentheses represent the corresponding case. | 79 |
| A.3 | Two examples of segmentation with the ground-truth in white and the resulted segmentations in yellow. Note that in both cases, Hausdorff distance is the same. | 80 |

List of Tables

| | Page |
|---|------|
| 4.1 Dice index and Hausdorff distance for the classic ASM. Dice value is between 0 and 1, values close to 1 indicate more similar contours. On the contrary, Hausdorff minimal values indicate more alike boundaries, in mm^2 . Bold values are the best values. . . . | 23 |
| 4.2 Dice index for the profile ASM/LBP scheme using the original LBP, uniform LBP, number LBP, and median LBP. Dice value is between 0 and 1, values close to 1 indicate more similar contours. Bold values are the best per slice | 24 |
| 4.3 Hausdorff distance for the profile ASM/LBP using the original LBP, uniform LBP, number LBP, and median LBP. Hausdorff minimal values indicate more similar boundaries, in mm^2 . Bold values are the best per slice. | 24 |
| 4.4 Dice index for the quadratic ASM/LBP scheme using the original LBP, uniform LBP, number LBP, and median LBP. Dice value is between 0 and 1, values close to 1 indicate more similar contours. Bold values are the best per slice | 25 |
| 4.5 Hausdorff distance for the quadratic ASM/LBP scheme using the original LBP, uniform LBP, number LBP, and median LBP. Hausdorff minimal values indicate more similar boundaries, in mm^2 . Bold values are the best per slice. | 25 |
| 5.1 Dice index results. Dice index is between 0 and 1, values close to 1 indicate more similar contours. Values 10, 20, 30, ..., represent the percentages of the CT volumes taken during the cardiac cycle. LBPUM represents a combination of three LBPU: {P=8,R=1}, {P=16,R=2}, and {P=24,R=3}. The values represent the average index on all the patients. | 41 |
| 5.2 Hausdorff distance results. Lowest values indicate more alike boundaries in mm^2 . Values 10, 20, 30, ..., represent the percentages of the CT volumes taken during the cardiac cycle. LBPUM represents a combination of three LBPU: {P=8,R=1}, {P=16,R=2}, and {P=24,R=3}. The values represent the average distance on all the patients. | 41 |
| 5.3 Sigma values for Active Contour methods. | 59 |

1

Introduction

1.1 Motivation

One of the main technological challenges in medical imaging is the correct visualization and diagnosis. The amount of medical image studies taken from human organs has increased over the last years and most of these studies are subjected to human expert interpretations, not always achieving optimal results. If we add the large number of technique's variations used to acquire these studies and the fact that they depend on many human factors, a need for developing more effective methods for the medical community is imperative.

Medical image analysis has become an important tool for improving medical diagnosis and planning treatments. It involves volume or still image segmentation and classification of different anatomical structures, such as heart and its cavities as mentioned in the method's reviews by [1], [2],[3] or isolated structures like ventricles as in [4], [5], [6], [7], or different analysis such as heart movement measurement [8], some other studies focused on brain's organs like mesencephalon [9], [10],[11] and other organs such as lung tissue [12], cerebellum of fetuses [13], mandibular canal [14], bones from CT and MRI [15],or more general medical image segmentation such as [16], [17], [18] that could be applied on different human organs. All of these tasks play a critical role in understanding image content and facilitating extraction of the anatomical organ or region-of-interest. They may also help towards the construction of reliable computer-aided diagnosis systems.

Defining edges and structures on human organs, is of considerable importance in medical

imaging and results are not always as expected. If in addition, we add organ movement, it increases the difficulty of the task. Such is the case of the heart, its arteries and its corresponding expansion and contraction. The visualization of human organs also depends on the type of image technology used like Magnetic Resonance (MR), Ultrasound, and Computer Tomography (CT).

Due to the fact that segmentation in medical images is still a challenging problem, numerous algorithms have been proposed in the literature. Such algorithms aim to solve this important stage for the subsequent higher-level analysis, for instance, characterization of an organ in an image. Segmentation methods can be divided in a general way into two categories: those requiring strong prior knowledge and those requiring weak or no prior knowledge. The first ones are more robust but require a learning phase which depends on the quality of the samples, making them less general. On the other hand, the second ones are in most cases less robust but they can be adapted to more general scenarios [1].

1.2 Objective of this work - Organization and outline

This thesis presents new segmentation methods that take advantage of additional image information such as texture and other inner characteristics, that combined with different active contour schemes, can improve their performance. The main model is inspired in visual perception namely the Hermite Transform.

In Chapter 2 we define the segmentation schemes to be used, Chapter 3 introduces the Hermite Transform as a local analysis tool with its advantages. Chapter 4 shows a first attempt in order to understand the combination of an Active Shape Model with a local analysis tool such as the Local Binary Pattern. Chapter 5 shows the application and comparison of two different segmentation schemes with Local Binary Patterns and the Hermite Transform as local information .

The segmentation methods are applied over complete volumes in a 2-dimensional approach, and in one of the applications, time variation is taken into account. The different schemes are applied on human organs such as midbrain or mesencephalon in MRI, as well as left ventricle's heart in CT. Performance is evaluated on these organs through the correct edge identification and on structures with movement. The combination of different schemes produces more robust analysis methods compared with the traditional ones found in the literature.

Finally Chapter 6 mentions some present clinical applications, and the last Chapter 7 summarizes the conclusions of this work.

2

Active contours and Deformable Models

This section briefly presents the mathematical foundations used in this research. As mentioned previously adequate border delineation is highly desirable in many organ structures. Some early models used for this objective were the active contours and deformable models which provide powerful advantages to the image analysis field. Segmentation tasks are still challenging because of the nature of the organ anatomy, their function and their image characteristics, such as noise, artifacts and acquisition protocols. The most common segmentation techniques can be classified in two sets [1]:

1. Segmentation techniques without previous knowledge of the segmented object or with very little information. It includes most of the basic methods based on image information or pixel classification. These techniques include algorithms like thresholding, border detection, region growing and graph-cuts, as well as basic level sets.
2. Segmentation techniques with more elaborated previous knowledge, like deformable models, active shape models, active appearance models, and atlas based methods. The prior knowledge can be a speed restriction, a maximal statistical distance between two or more organs, or a shape restriction that modifies the curve evolution.

The present work objective is to improve different schemes of segmentation techniques like active contours and deformable models, which belong to the more robust segmentation category, making use of local analysis methods. These models rely on the idea that a curve from a given image, subjected to some constraints, can evolve in order to detect objects and sometimes even

specific shapes. This thesis is focused on two different models: Active Shape models and Deformable models implemented by Level Sets.

Active Shape Models (ASM) [19] are part of the statistical deformable models; they can detect objects with specific shape boundaries. Cootes et al. argue that a shape model can deform to some extent within a certain variability. Therefore, ASMs are able to deform their shape so that they resemble the real organ. Other studies [4, 13] have applied ASMs to different anatomical organs, such as heart and pediatric cerebellum.

Deformable models and their implementation by level sets proposed in [20] have been widely used in medical image segmentation [17]. They deform according to the image features used to handle the curve evolution, and they can be categorized as edge based [21], region based [22, 23] and model shape based [18, 24]. An extension of the method for vector-value images was proposed by Chan and Vese [25] and was applied to color images. Additionally, Paraggios et al. [26] applied it to supervised texture segmentation problems. The vector value extension allows to introduce different kinds of features at the same time without requiring any prior knowledge. For example, Brox et al. [27] introduced simultaneously texture features, gray level and optic flow for the segmentation process.

2.1 Active Shape Models

In [19], Cootes et al. proposed Active Shape Models (ASM) as a refinement of statistical deformable models, as part of the method it trains a known shape, with the final purpose of recognize it in a new image. An ASM creates a point distribution model (PDM) from a certain number of similar shapes and from here obtains an average shape, \bar{X} . The goal of the approach is based on the idea that it is possible to deform \bar{X} to some extent in order to produce certain variability until the ASM meets the boundaries of the object of interest.

The algorithm consists basically of two steps: **build a statistical shape model** from a set of aligned shapes and at the same time compute a gray level appearance model to obtain specific characteristics of boundary points; and execute an **ASM search**, to recognize a similar model shape. For the set of aligned shapes of an organ, ASM method uses pose transformations (rotation, translation, and scaling).

More details are as follows:

- **Statistical Shape model** is obtained by executing a statistical shape and a gray-level profile model.
 1. A set of M aligned shapes is built. We use manual annotations for each volume to be involved in the training phase, delineating contour lines of the shape for each image. An alignment is applied to each shape involving translation, rotation, and size transformations. For each training shape, a vector of landmarks is obtained

$S_i = ((x_0, y_0), \dots, (x_{n-1}, y_{n-1}))^T$. So that, the average shape is the mean shape, \bar{X} , is the average of all landmarks $\bar{X} = \frac{1}{M} \sum_{k=0}^{M-1} S_k$.

- The variations of the mean shape are obtained by computing principal component analysis [19], and single value decomposition is used to find the Point Distribution Model (PDM) parameters [14]. The less significant eigenvalues and eigenvectors are removed to avoid singular correlation matrix and data over-fitting [28]. The number of training datasets is often (very) small in comparison to the number of landmarks and they can lead to a singular correlation matrix and over-fitting of the training data. To reduce such effects it is necessary to crop the number of eigenvalues keeping between 90% and 99.5% of the variance in the training data. This is done by removing the lowest eigenvalues and corresponding eigenvectors computed for the PCA analysis, see Fig. 2.1. The mean shape is deformed within certain limits to recognize a new shape according to $\hat{X} = \bar{X} + P\mathbf{b}$, where P is the matrix of the t first principal components, \mathbf{b} is the weight vector, and \hat{X} is the estimated shape.

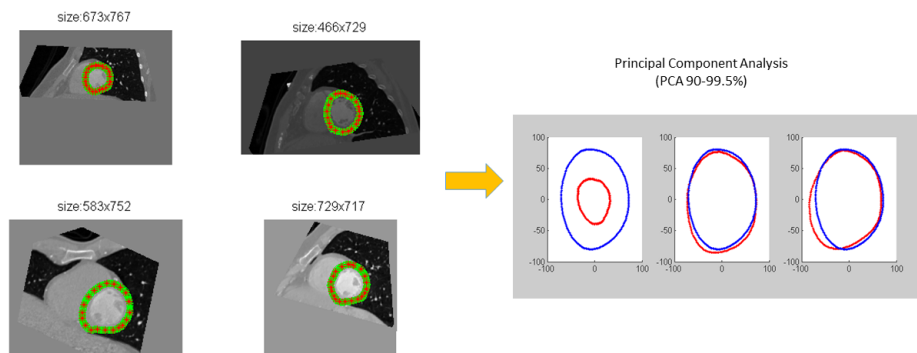


Figure 2.1: (a) ASM Training Shapes and creating Point Distribution Model of the left ventricle in CT.

The gray-level profile model is also part of the training statistical model construction. Since shapes are described by points enclosing a contour, gray-level profiles normal to each landmark point are calculated. First and second moments are obtained by calculating the mean and covariance matrix from the training set. Either the gray profile or its normalized derivative can be employed. Using derivatives of the gray profile may be advantageous because it avoids the problem of contrast invariance in the images but, at the same time they are more sensitive to noise.

● ASM search

- In the search phase \bar{X} is placed close to the object of interest manually. The mean shape

is deformed within certain limits to recognize a new shape as follows:

$$\hat{X} = \bar{X} + Pb \quad (2.1)$$

where \bar{X} is the average shape $\bar{X} = \frac{1}{s} \sum_{i=0}^{s-1} x_i$, P is the matrix of the t first principal components, b is a vector of weights and \hat{X} is the estimated shape. Eq. (2.1) is known as Point Distribution Model (PDM). Each landmark in \bar{X} is compared against its corresponding profile, which is a line of pixels that is perpendicular to the landmark. Then, the landmarks are moved iteratively towards those that obtain the lowest distance, using for example the Mahalanobis distance. The new contour coordinates, \hat{X} , are an estimate of the original contour, \bar{X} . It is possible to generate new shapes by modifying a parameter b within certain limits to obtain similar shapes of the object to be recognized [29]. Here, b is constrained to the range $\pm m \sqrt{\lambda_i}$ with m between 2 and 3. This restriction limits shapes within 2 or 3 standard deviations of the distribution of shapes in the training data.

2. When new positions for the landmarks are found, an aligning process must be computed to adjust the shape. Pose parameters are used to calculate final deformations to move the current estimate to a new position. The process is iterative and stops when a specific number of iterations or a threshold is reached.

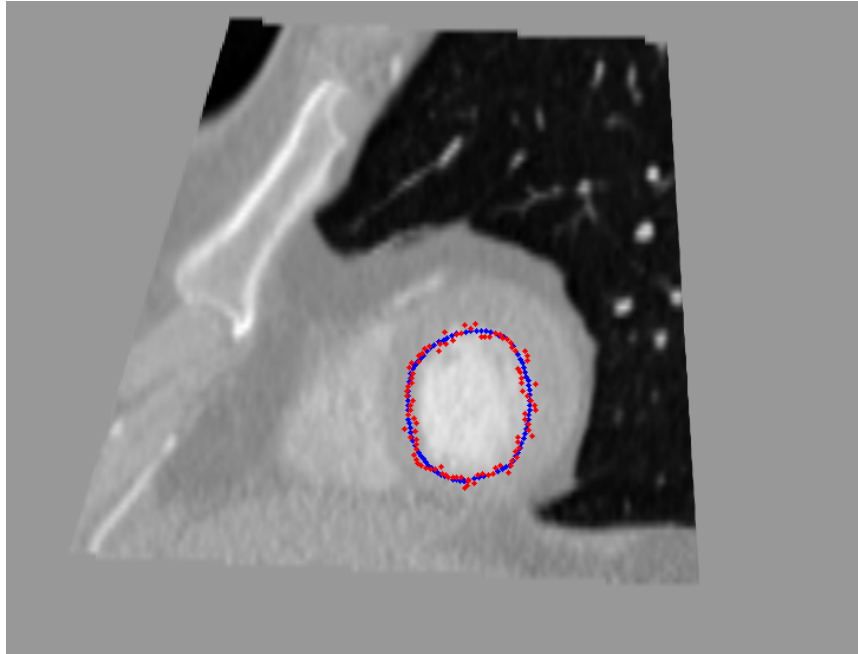


Figure 2.2: ASM Adjustment in the search phase.

It is well-known that ASMs are often limited when dealing with texture segmentation because they model contours using only shape. Typically, gray level information is included in the functional that drives the fitting of the contour. In contrast, Active Appearance Model (AAM)

proposes an alternative to represent contours using shape and texture parameters. Similarly to ASM, the joint model is constructed with eigenvalue analysis, however, this is more complicated and time consuming than an only-shape-based approach because it requires training. In our ASM proposal, texture characterization is computed using either Hermite coefficients or LBPs, and included within the functional that drives the contour. It is easier and faster to include texture information in a functional than in a parametric model because the functional does not need training [30, 31].

2.2 Level sets

The main idea of Active Contours is to evolve a curve so that it leads to a desired border object, according to an energy functional. Osher and Sethian [32] demonstrated that minimizing this energy functional of the contour C is equivalent to finding the minimum length of this curve, and the desired border is obtained during this time propagation as shown in Figure 2.3. In most cases a direct solution cannot be found, instead the active contour uses level sets as a numeric technique that starts with an initial curve as the zero level, and iteratively converges to the border based on a speed function called gradient flow. Osher and Sethian introduced this level set technique and represented the contour C as the function:

$$\phi(C(s, t)) = \phi(x(s), y(s), t) = 0 \text{ and } C = \{x \in \Omega : \phi(x) = 0\} \quad (2.2)$$

During implementation it is necessary to use an Euler-Lagrange discrete approximation, taking into account a distance function. This distance modifies the contour flow until it reaches the border.

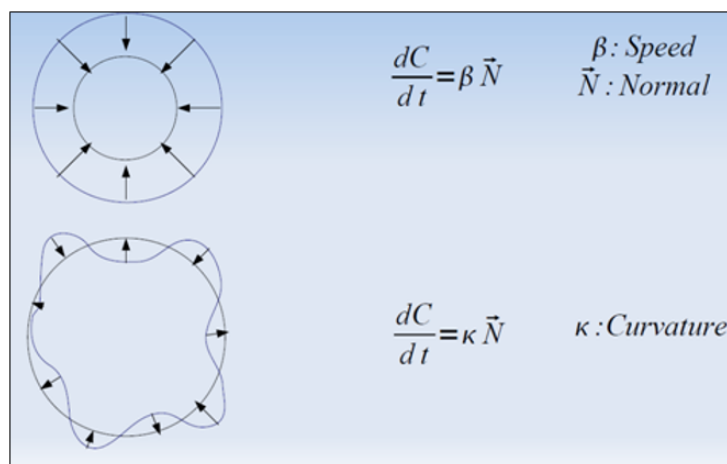


Figure 2.3: Curve propagation in normal direction.

Nowadays, a multitude of deformable models based on level set exists in the literature. The active contour without edges model was proposed by Chan-Vese [22] and it is inspired by the Mumford-Shah method for image segmentation which evolve an object by minimization of an

energy functional [33]. The original definition of the 2-dimensional Chan-Vese model (CV) is to let Ω be a bounded open set of \mathbb{R}^2 , with $\partial\Omega$ as the boundary. We define an image as $I : \Omega \rightarrow \mathbb{R}$. Now let C be an involving curve in Ω as a boundary between two regions in such a way that $\Omega = \Omega_1 \cup C \cup \Omega_2$, where Ω_1 and Ω_2 represent the inner and outer region of C , respectively. Finally, the formulation of the energy functional tries to identify the best partition on I as follows:

$$\inf_{c_1, c_2, C} F(c_1, c_2, C), \quad (2.3)$$

where c_1 and c_2 are the two average regions of intensity values inside and outside the contour, respectively. The energy is minimized if the contour C is located at the boundary of the object of interest. The 2-dimensional energy functional of the CV model in the domain $\bar{x} \in \mathbb{R}^2$ is defined as:

$$F(c_1, c_2, C) = \mu \int_C ds + \lambda_1 \int_{\Omega_1} (I - c_1)^2 \bar{x} + \lambda_2 \int_{\Omega_2} (I - c_2)^2 \bar{x}, \quad (2.4)$$

where λ_1, λ_2 are fixed non-negative constants for data fitting and μ is introduced to regularize the surface C . The minimal partition problem given by Equation (2.3) can be solved using the level set method [32]. The contour C can be represented by the non zero level set of a Lipschitz function, called $\phi : \Omega \rightarrow \mathbb{R}$, such that $C = \{\bar{x} \in \Omega | \phi(\bar{x}) = 0\}$. This approach has many advantages because it allows a wide study of topologies, which is made on a rectangular grid. The functional in Equation (2.4) can be written in terms of the level set as:

$$\begin{aligned} F(c_i, c_o, \phi) = & \mu \int_{\Omega} \delta(\phi(\bar{x})) (\nabla \phi(\bar{x})) d\bar{x} \\ & + \int_{\Omega} \lambda_1 (I(\bar{x}) - c_1)^2 H(\phi(\bar{x})) \bar{x} \\ & + \int_{\Omega} \lambda_2 (I(\bar{x}) - c_2)^2 (1 - H(\phi(\bar{x}))) \bar{x}. \end{aligned} \quad (2.5)$$

Considering the approximations of the Heaviside H and Dirac δ functions [22], as specified in the original paper, the minimization is solved with the Euler-Lagrange equation for an artificial time $t \geq 0$:

$$\frac{\partial \phi}{\partial t} = \delta(\phi) \left[\mu \operatorname{div} \left(\frac{\nabla \phi}{|\nabla \phi|} \right) - \lambda_1 (I(\bar{x}) - c_1)^2 + \lambda_2 (I(\bar{x}) - c_2)^2 \right]. \quad (2.6)$$

The Equation (2.6) is implemented as a discrete model through finite differences. The vector-value model for Chan-Vese (VVCV) proposed in [25] uses K -extra information in order to obtain a

better segmentation.

$$\begin{aligned} \frac{\partial \phi}{\partial t} = \delta(\phi) \left[\mu \operatorname{div} \left(\frac{\nabla \phi}{|\nabla \phi|} \right) - \frac{1}{K} \sum_{i=1}^K \lambda_i^+ (I_i(\bar{x}) - c_i^+)^2 \right. \\ \left. + \frac{1}{K} \sum_{i=1}^K \lambda_i^- (I_i(\bar{x}) - c_i^-)^2 \right], \end{aligned} \quad (2.7)$$

where c^+ and c^- are constant vectors that represent the average value of one of the K layers of I_i inside and outside the curve C , respectively. The parameters λ_i^+ and λ_i^- are constant weights defined manually for the user and further discussed in the experimental results section.

The model is useful when an image does not contain well-defined boundaries; furthermore, it is less sensitive to noise. In summary this model extension, called vector-value model [25] uses complimentary information of the image, that can be considered to obtain an improved segmentation.

To obtain c_i^+ and c_i^- we use the next equations:

$$\begin{aligned} c_i^+ &= \frac{\int_{\Omega} u_{0,i}(x,y)H(\phi(x,y))dxdy}{\int_{\Omega} H(\phi(x,y))dxdy} && \text{average } (u_{0,i} \text{ on } \phi \geq 0), \\ c_i^- &= \frac{\int_{\Omega} u_{0,i}(x,y)(1-H(\phi(x,y)))dxdy}{\int_{\Omega} H(\phi(x,y))dxdy} && \text{average } (u_{0,i} \text{ on } \phi < 0) \end{aligned} \quad (2.8)$$

Equation 2.7 is implemented as a discrete model through finite differences. However, this method is computationally demanding [34, 35].

The advantage of using Eq. 2.7 along with texture descriptors, as components of an image vector, is that the level set will use more information such as texture and contour which results in a better segmentation than if it uses only a single dimension of the original image.

An important step in the algorithm is to construct the vector features. Different strategies are possible; one way is to take each vector component and apply a classical Gaussian kernel. However, the major problem with this approach is the attenuation of edges due to the smoothing of Gaussian Kernels that leads to an inaccurate results.

2.2.1 FAST LEVEL SETS

The main problem of the Chan-Vese vector value approach is that it needs heavy computational cost in some cases, and is hard to be implemented because implies a long time when solving the partial differential equation (PDE). Also it may need extra precision not so desirable at the pixel level. To overcome this problem exists the Fast Level Sets (FLS) model.

The FLS [15] is a variation of the classic Chan-Vese algorithm, where the discrete implementa-

tion of eq. 2.7 is:

$$\begin{aligned} \phi^{n+1} = \phi^n - \Delta t \left[\delta(\phi) \left[\mu \operatorname{div} \left(\frac{\nabla \phi}{|\nabla \phi|} \right) - \frac{1}{K} \sum_{i=1}^K \lambda_i^+ (I_i(\bar{x}) - c_i^+)^2 \right. \right. \\ \left. \left. + \frac{1}{K} \sum_{i=1}^K \lambda_i^- (I_i(\bar{x}) - c_i^-)^2 \right] \right], \end{aligned} \quad (2.9)$$

FLS aims to improve performance and reduce computational complexity by avoiding the iterative solution of the partial differential equation, Eq. (2.7). It has a simple discrete representation that reduces computational complexity by simplifying the speed function. An important characteristic is that the initial level set approximates the distance function with a similar sign to the narrow band method. This fact implies more movement control. In the representation of a boundary in the fast level set method, each pixel is assigned a level set function value. Two sets of neighboring grid points L_{in} and L_{out} are defined. The motion of the curve is implicitly represented by maintaining the point sets L_{in} and L_{out} see Fig. 2.4.

The idea of FLS is to represent the zero level set as a list of boundary points that moves towards a discrete edge without computing Eq. (2.7). At the same time, FLS preserves the advantages of traditional methods and it is not necessary recalculate the PDE.

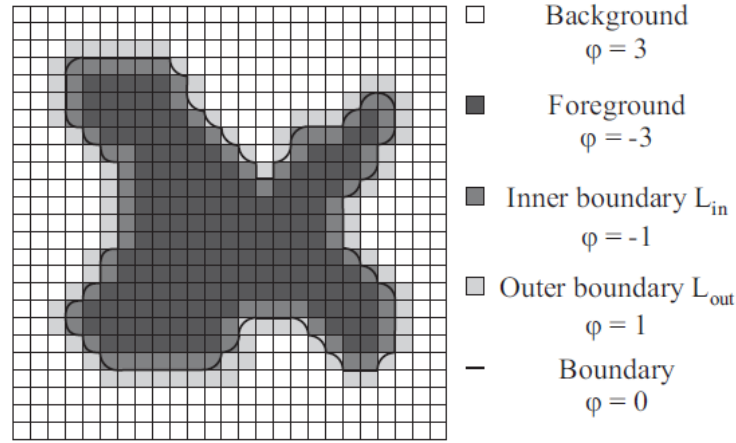


Figure 2.4: Representation of a boundary in the fast level set method.

Further simplifications come from the the fact that the evolution of FLS needs binary information that derives into a speed function $v(x)$ as follows, for the case of only one image component ($K = 1$) from equation 2.9:

$$v(x) = \begin{cases} 1 & \text{if } -\lambda^+(I(x) - c^+)^2 + \lambda^-(I(x) - c^-)^2 \geq 0 \\ -1 & \text{if } -\lambda^+(I(x) - c^+)^2 + \lambda^-(I(x) - c^-)^2 \leq 0 \end{cases} \quad (2.10)$$

The FLS algorithm depends mainly on the initial speed field that:

- reflects only external forces of the image
- is positive on the contour's inside and viceverse
- uses a segmentation criteria similar to the Chan Vesse modified

The algorithm includes a regularization term, that is worked as an additional step, not inside the algorithm. In this term an anisotropic Gaussian filter is applied to the level set function.

The evolution of the boundary is driven by a scalar velocity field v . It reflects the image based external force. Positive $v(x)$ value stands for a foreground image pixel and indicates that the boundary is to be moved outwards and vice-versa. Interface evolution is realized by updating the L_{in} and L_{out} sets. However, the main drawback is that the initial regions must be well defined in order to create the initial speed. The algorithm inputs are the image I , an initial level set function v , a number of evolution Ne and smoothing steps Ng , a standard deviation σ of the Gaussian kernel G , the Chan-Vese criteria, a maximum number of iterations $Nmax$ and the maximum percentage of changed boundary pixels for the stopping criterion. The output is the final level set function ϕ , as the next summary shows. The reference is taken from Kratky et al. [15].

Algorithm 2.1: FLS algorithm

```

1 Compute the velocity field  $v$  ;
2 Create the Gaussian mask  $G$  ;
3 Create the  $L_{in}$  and  $L_{out}$  from  $\phi$  ;
4 while the stopping criterion is not reached do
5   for  $i \leftarrow 2$  to  $Ne$  (evolution iterations) do
6     Outward evolution;
7     Eliminate redundant points in  $L_{in}$ ;
8     Inward evolution;
9     Eliminate redundant points in  $L_{out}$ ;
10  end
11  for  $i \leftarrow 2$  to  $Ng$  (smoothing iterations) do
12    Outward evolution smoothing ;
13    Eliminate redundant points in  $L_{in}$  ;
14    Inward evolution smoothing ;
15    Eliminate redundant points in  $L_{out}$  ;
16  end
17 end
18 Return final  $\phi$  ;

```

3

Hermite's Local Information

3.1 Local Analysis by Perceptual based models

The human brain divides the human vision signal into many channels that stream different kinds of information into our brain. Our brain has an attention system that identifies, in a task-dependent way, important parts of an image to examine while suppressing examination of other areas. There is massive feedback in the visual stream that is little understood. The feedback loops in the brain go back to all stages of processing including the hardware sensors themselves (the eyes), which mechanically control lighting via the iris and tune the reception on the surface of the retina [36].

Just like human perception, image processing requires image data to be interpreted with visually significant patterns. This requires to determine spatio-temporal relations among the intensities. This includes a local analysis that implies a multiplication of the signal by a window. The window determines the information in the basic processing operation and establishes the relative contribution weight for each point. In order to describe the image in a complete way, the local processing has to be repeated a sufficient number of window positions [37]. An expansion of the image into basis functions is done on the windowed signal in order to identify relevant visual patterns [38].

Initially Gabor functions have been used as a reference of the Human Visual system to model receptive fields and important cells within the visual cortex. More recent studies have shown that Gaussian derivatives also provide a good approximation of this receptive fields, with the advantage of requiring less parameters and possessing better orthogonality conditions. For all this properties

the Hermite Transform (HT) is an efficient model for image analysis. The relevance of HT relies on the fact that its basis functions mimic receptive fields of the human visual system and reproduce relevant image structures efficiently [39, 40].

3.2 Hermite Transform

Over the last decades, many computational methods have incorporated simple biological properties of vision. One example is the Hermite transform [38] that allows us to perform local orientation analysis by windowing an image with a Gaussian function. On each window position, an expansion using orthogonal polynomials, is calculated; such an expansion is called Hermite coefficients.

HT is a special case of the Polynomial transform [38, 41] and analyzes pixel information using a window function $v^2(x, y)$ in order to expand the information in terms of a family of polynomials $G_{m,n-m}(x, y)$, where they are orthogonal with respect to the window function. From a perceptual point of view, adjacent Gaussian windows separated by twice the standard deviation σ represent a good model of the overlapping receptive fields found in physiological experiments [42]. Therefore $v(x, y) = \frac{1}{\sigma\sqrt{\pi}} \exp(-\frac{x^2+y^2}{2\sigma^2})$ represents a Gaussian window with a normalization factor that defines a unitary energy for $v^2(x, y)$. The HT is obtained by performing a convolution of the image $L(x, y)$ with the filter functions:

$$D_{m,n-m}(x, y) = G_{m,n-m}(-x, -y)v^2(-x, -y) \quad (3.1)$$

as follows:

$$L_{m,n-m}(x_0, y_0) = \int_{-\infty}^{\infty} \int_{-\infty}^{\infty} L(x, y)D_{m,n-m}(x_0 - x, y_0 - y)dx dy \quad (3.2)$$

where m and $(n - m)$ denote the analysis order in X and Y respectively with $n = 0, \dots, \infty$ and $m = 0, \dots, n$.

The HT is associated with a class of orthogonal polynomials called Hermite polynomials, $H_n(x)$, defined as follows:

$$H_n(x) = (-1)^n e^{x^2} \frac{d^n(e^{-x^2})}{dx^n} \quad (3.3)$$

where n denotes the order of the polynomial.

Then the polynomials $G_{m,n-m}(x, y)$ are defined as:

$$G_{m,n-m}(x, y) = \frac{1}{\sqrt{2^n m!(n-m)!}} H_m\left(\frac{x}{\sigma}\right) H_{n-m}\left(\frac{y}{\sigma}\right) \quad (3.4)$$

where $H_n\left(\frac{x}{\sigma}\right) = (-1)^n \exp\left(-\frac{x^2}{\sigma^2}\right) \frac{d^n}{dx^n} \exp\left(-\frac{x^2}{\sigma^2}\right)$ represents the generalized Hermite polynomials with respect to the Gaussian function (with variance σ^2).

An advantage of the Hermite filters is that they are separable because the Gaussian window is

rotationally symmetric and can be computed by eq. 3.5, as illustrated in Fig. 3.1:

$$D_n(x) = \frac{(-1)^n}{\sqrt{2^n n!}} \frac{1}{\sigma \sqrt{\pi}} H_n\left(\frac{x}{\sigma}\right) \exp\left(-\frac{x^2}{\sigma^2}\right) \quad (3.5)$$

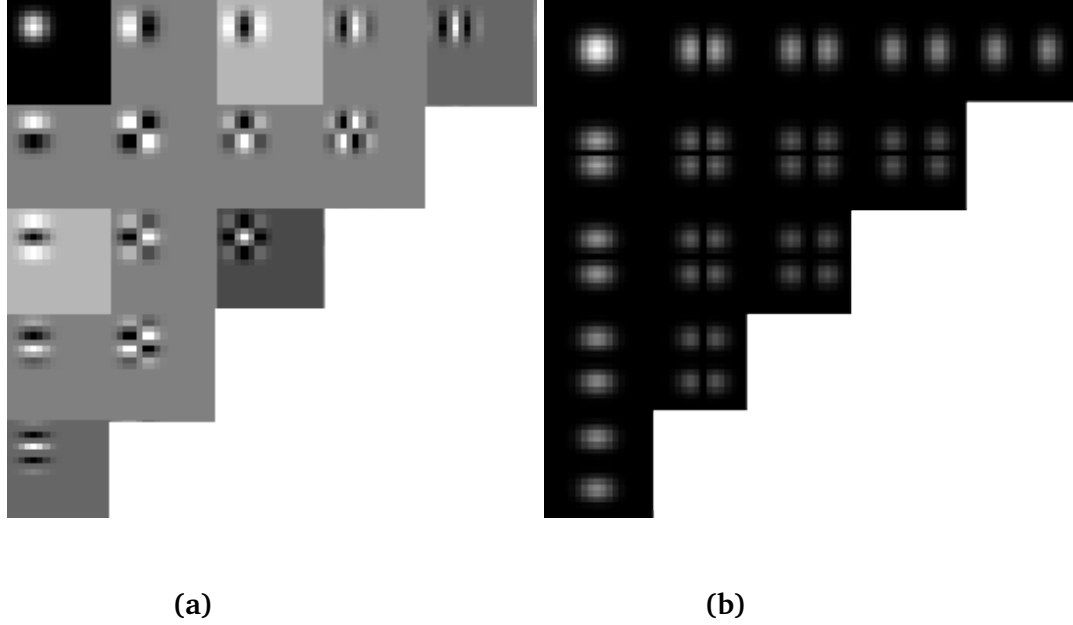


Figure 3.1: (a) Ensemble of spatial Hermite filters (left) and their corresponding frequency responses (right). The displayed orders go from $N = 0$ to $N = 4$.

The Cartesian Hermite coefficients, $L_{n-m,m}$, can be directly obtained by convolving the image, $I(x, y)$, with the Hermite analysis functions, D_n as follows:

$$L_{n-m,m}(x_0, y_0) = \int \int I(x, y) D_{n-m,m}(x_0 - x, y_0 - y) dx dy \quad (3.6)$$

with $D_n = H_n(-x) \cdot G^2(-x)$. The variable $G^2(-x)$ represents a Gaussian function, (see Fig. 3.1).

3.3 Hermite as local information

An improvement of the HT is the steered Hermite transform (SHT). This transform uses filters that belong to a class of rotated filters constructed as a linear combination of the original basis [43, 44]. The orientation selectivity property of the Hermite filters explains why they are products of polynomials with a radially symmetric window function (Gaussian function).

The steered Hermite transform (SHT) is derived from a linear combination of rotated Cartesian Hermite coefficients (see Fig. 3.2). The rotation follows a maximum energy criteria [45]. SHT produces a new and reduced set of Hermite coefficients oriented over the angle θ .

The $N + 1$ Hermite filters of order n form a steerable basis for each individual filter of order n .

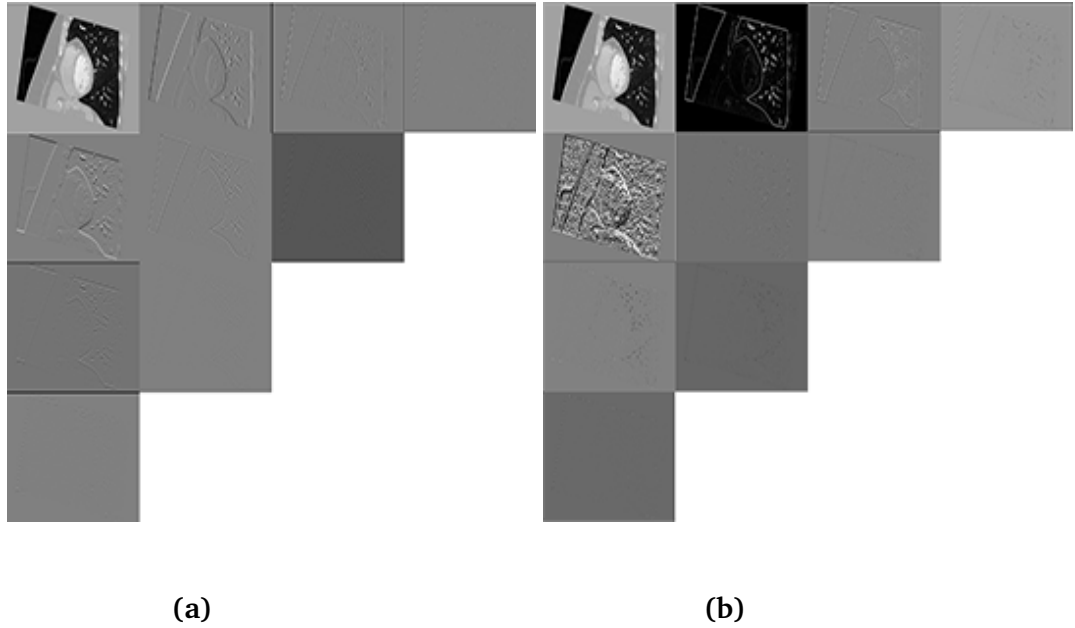


Figure 3.2: Cartesian (left) and steered Hermite coefficients (right). Note that most of the coefficient energy is concentrated in the upper row of the steered Hermite coefficients.

The resulting filters can be interpreted as directional derivatives of a Gaussian function. In this way, a more general expression of the Cartesian Hermite coefficients can be written in terms of the orientation selectivity:

$$l_{m,n-m,\theta}(x_0, y_0) = \sum_{k=0}^n L_{k,n-k}(x_0, y_0) g_{k,n-k}(\theta) \quad (3.7)$$

where $l_{m,n-m,\theta}(x_0, y_0)$ are the steered Hermite coefficients and $g_{m,n-m}(\theta) = \sqrt{\binom{n}{m}} (\cos^m(\theta)) (\sin^{n-m}(\theta))$ are the Cartesian angular functions of order n that express the directional selectivity of the filter.

For local 1D patterns, the SHT is an efficient way to compactly describe image features into a smaller number of coefficients that represent the profile of the pattern perpendicular to its orientation (θ) see Figure 3.2 [46]. Since the steering angle depends on the local maximum energy, it is possible to obtain image descriptors that are invariant to the image orientation [45].

SHT has proven to be effective in texture analysis [37, 45]. It is well suited for multi-resolution analysis and can be easily implemented using properties of steerable filters [37].

In this thesis the Hermite Transform is used as an additional local information, that helps improve the results of segmentation techniques based on Deformable Models, such as ASM and Level Sets algorithms. Another tool that gives local information, Local Binary Patterns, is referenced by chapter 4, as the first attempt to incorporate it into the segmentation technique, and also compare it in chapter 5 against the Hermite transform.

4

Midbrain volume segmentation

This chapter describes an application that adds local information to an active contour model. Local Binary Patterns are used as the local analysis tool and it is combined on the segmentation method, as an initial research of this thesis. The method is assessed on mesencephalon. The proposal aims to evaluate different combinations of ASM/Local Binary Pattern algorithms to segment the mesencephalon.

Midbrain or mesencephalon is an approximately $2 \times 2 \times 1$ cm sized region near the center of the brain that serves as a relay center for visual, auditory, and motor system information, see Figure 4.1. It controls many important functions such as pupil diameter, eye movement, and hearing. Two structures can be identified in the interior of the midbrain: the *red nucleus*, which is involved in motor coordination and the *substantia nigra*, a dark area related to learning process and motor control [47]. The *substantia nigra* contains high levels of melanin and dopamine-containing neurons, which are severely affected by the degenerative process of Parkinson's disease (PD) [48].

4.1 Introduction

In 2010, Sakal et al. [49] proposed a technique based on echoscopy for supporting the clinical diagnosis of PD; they have claimed that the initial assessment of the neurological condition of a patient should be performed by estimating the area of the *substantia nigra*. A recent non-invasive tool for analyzing midbrain is MRI, which offers the possibility of a deeper study of this organ by obtaining a series of images with the capability to segment and build a volume or a 3D

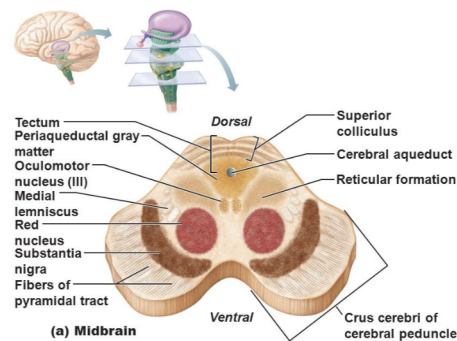


Figure 4.1: Midbrain positioned within the human brain. Picture taken from "The Brain Muse spring 2430 lecture 15 7/12/10", <http://slideplayer.com/slide/7375938/>

representation. However, visualization of inner structures, which helps diagnosis of PD, can not be achieved so easily. Chen et al. [10] addressed this issue and proposed affine registration of two modalities of MRI: T1 and SWI.

Precisely, because of the fact that PD is associated with destruction of neurons in the midbrain, its segmentation has become an important issue in neurological applications. Currently, midbrain segmentation is a manual process where experts delineate the contours of the organ from MRI images. State-of-the-art approaches to segment midbrain automatically are mainly based on active models applied on ultrasound and sonographic modalities [9, 11]. These studies use different variants of Active Contour Models (ACM) and Active Appearance Models (AAM) and even make use of the toolbox SPHARM [50]. However, automatic segmentation of the midbrain and *substantia nigra* area still poses a challenge. One important drawback is the lack of databases available for this type of research.

Midbrain normally has a typical shape which can be obtained by statistical methods see Figure 4.1. Nevertheless, noise and lack of contrast are two frequently problems that hamper the final segmentation. To overcome this issue, an automatic method for segmenting midbrain, based on the combined use of Active Shape Models (ASM) and Local Binary Patterns (LBP), is proposed. The joint-model considers both global and local statistics to improve the final shape. LBPs are used to detect midbrain boundaries correctly; LBPs add to ASMs the robustness needed to detect non-salient boundaries in the presence of noise that some other methods lack. The result was a statistical model able to improve structure resolution because of the LBPs.

4.2 Local binary patterns

- The original **Local Binary Pattern** (LBP) descriptor [51] was proposed by Ojala et al. It is based on the idea that textural properties within homogeneous regions can be mapped into patterns that represent micro-features. This proposal uses a fixed rectangular 3×3 mask, which represents a neighborhood around a central pixel. The values within the rectangular

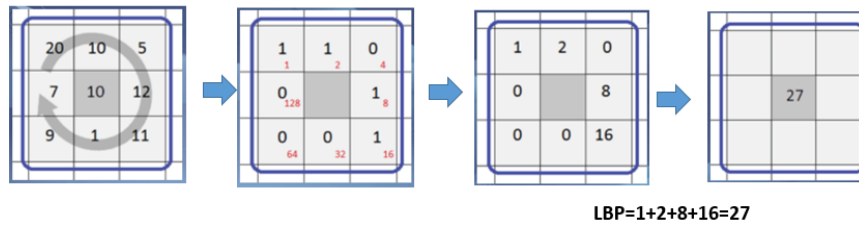


Figure 4.2: Description of the Local Binary Pattern method

mask are compared with their central pixel; those ones lesser than the central value are labeled with “0” otherwise they are labeled with “1”. The labeled pixels are multiplied by a weighting function according with their positions to form a pattern chain. Afterwards, the sum of the eight pixels replaces the value of the central pixel. This method describes differences of intensities and produces 2^8 possible labels. See Figure 4.2.

In addition, it has very low computational and space complexity. Ojala et al. have claimed that this type of threshold operations provide a robust way for describing local texture patterns.

Further generalizations use a circular neighborhood instead of a fixed rectangular region. The sampling coordinates of the neighbors are calculated using the expression: $(x_c + R \cos[\frac{2\pi p}{P}], y_c - R \sin[\frac{2\pi p}{P}])$. If a coordinate does not fall on an integer position then the intensity values are bi-linearly interpolated. Such implementations allow us choosing the spatial resolution (R) and the number of sampling points (P) as follows:

$$LBP_{P,R}(g_c) = \sum_{p=0}^{P-1} s(g_p - g_c) 2^p \quad (4.1)$$

where P is the number of sampling points, R represents the radius of the neighborhood, g_c , is the central pixel at (x_c, y_c) , and $\{g_p | p = 0, \dots, P-1\}$ are the values of the neighbors whereas the comparison function, $s(x)$, is defined as:

$$s(x) = \begin{cases} 1 & \text{if } x \geq 0 \\ 0 & \text{if } x < 0 \end{cases} \quad (4.2)$$

LBP's possess known characteristics, such as:

- They are operators that transform images into labels and these labels can be represented as histograms (fingerprints)
- They are invariant to rotations and monotonic gray level changes
- They work with different contrast distributions
- They can be used in different angles of an image, light changes, noise or occlusions

- They are used for detection and classification tasks. Such as texture classification, facial recognizing and object categorization

Also other variations of LBPs exist.

- **Uniform Local Binary Patterns** ($LBP_{P,R}^{uni}$) [52]. Over 90% of LBP texture patterns can be described with few spatial transitions, which are the changes (0/1) in a pattern chain. Ojala et al. introduced a measure of uniformity, $U(LBP_{P,R}(g_c)) = |s(g_{p-1} - g_c) - s(g_0 - g_c)| + \sum_{p=1}^{P-1} |s(g_p - g_c) - s(g_{p-1} - g_c)|$, which corresponds to the number of spatial transitions. So that, $LBP_{P,R}^{uni}$ can be obtained as:

$$LBP_{P,R}^{uni}(g_c) = \begin{cases} \sum_{p=0}^{P-1} s(g_p - g_c) & \text{if } U(LBP_{P,R}(g_c)) \leq 2 \\ P + 1 & \text{otherwise} \end{cases} \quad (4.3)$$

then, the pixel-wise information is encoded as a histogram, H_i , so that it can be interpreted as a fingerprint or a signature of the analyzed object.

- Yan Ma [53] proposed the **Number LBP** ($LBP_{P,R}^{num}$) as an extension of the Eq. (4.3) by dividing the non-uniform patterns into groups based on the number of “1” or “0” bits as follows:

$$LBP_{P,R}^{num}(g_c) = \begin{cases} \sum_{p=0}^{P-1} s(g_p - g_c) & \text{if } U(LBP_{P,R}(g_c)) \leq 2 \\ Num_1\{LBP_{P,R}(g_c)\} & \text{if } U(LBP_{P,R}(g_c)) > 2 \text{ and } \\ & Num_1\{LBP_{P,R}(g_c)\} \geq Num_0\{LBP_{P,R}(g_c)\} \\ Num_0\{LBP_{P,R}(g_c)\} & \text{if } U(LBP_{P,R}(g_c)) > 2 \text{ and } \\ & Num_1\{LBP_{P,R}(g_c)\} < Num_0\{LBP_{P,R}(g_c)\} \end{cases} \quad (4.4)$$

where $Num_1\{\bullet\}$ is the number of “1” and $Num_0\{\bullet\}$ is the number of “0” in the non-uniform pattern.

- The presence of noise can seriously impair the performance of the LBP operator. Zabih’s proposal [54] replaces the central pixel with the median of itself and the P neighbors. This implementation is called **median LBP**.

$$LBP_{P,R}^{med}(g_c) = \sum_{p=0}^{P-1} s(g_p - \tilde{g}) \quad (4.5)$$

where \tilde{g} represents the median of the P neighbors and the central pixel. This modification is still invariant to rotation but less sensitive to noise. It is also invariant to monotonic illumination changes.

Keomany and Marcel [55] proposed a method that combines ASM and LBP using what is

known as Extended LBP and Square-based LBP. They concluded to have better results with the ASM/LBP approach than with the ASM algorithm alone.

4.3 Materials

The experiments used a dataset labeled by an experienced image neurologist. This dataset was selected randomly by Dr. García at Hospital Interlomas (Mexico) using MRI scans. It consists of cranial annotated midbrain studies from 10 normal subjects. The T2 images were obtained on a 3 Tesla scanner, (TR = 3200 ms, TE = 409ms, flip angle = 120), obtaining volumes of $512 \times 448 \times 176$ pixels with a resolution of $0.44921 \times 0.44921 \times 0.9$ mm.

The volume images were preprocessed with a normalization of gray intensities and the midbrain area of interest is approximately 70×70 pixels per image. The algorithms were run on a Intel Xeon Quad Core workstation with 2.40Ghz and 6GB of RAM memory.

4.4 Proposed Method

Different combinations of ASM/LBP algorithms are evaluated inspired in the Keomany and Marcel model, adding new types of LBPs to test, and at the same time improve midbrain segmentation. We also tested the simple ASM algorithm in order to have a comparison base for our improvements. We used cranial magnetic resonance images containing the midbrain volume. One of the main problems we found was the lack of sufficient data in order to train the ASM according to the estimates mentioned by Cootes. Ten segmented volumes were available at the moment and a Leave One Out validation method was executed. The computed ASM/LBP algorithm differs from Keomany in the way that they first obtained their LBP's image and then apply the ASM Algorithm.

In the initial **training phase**, the LBP operator evaluates each landmark point on a window of 5×5 pixels. This is accomplished instead of the gray profiles of the traditional method. An LBP analysis is computed for each pixel of the window, and at the end a histogram is calculated per landmark. The result is a characteristic histogram of the surrounded region of the landmarks. This fact implies that instead of evaluating over one central pixel, the LBP evaluates over a whole region. Hence, more information of the area is saved in the training phase and used for recognition.

The **ASM search** phase examines the LBP's normal profiles of the contour, a histogram is obtained per landmark of the profile, the histograms are compared against the histogram of the trained model see Fig. 4.3(a), and the one with the minimum distance is used to obtain the correct boundary adjustment.

A second approach, is to take into account a bigger divided quadratic region, where the central pixel is the landmark point and its surrounding area is divided into 4 windows of size 5×5 pixels and an LBP was computed for each window, each window possess a histogram. And a resulting histogram of each quadratic zone is concatenated to produce a single one, see Fig. 4.3(b). And this

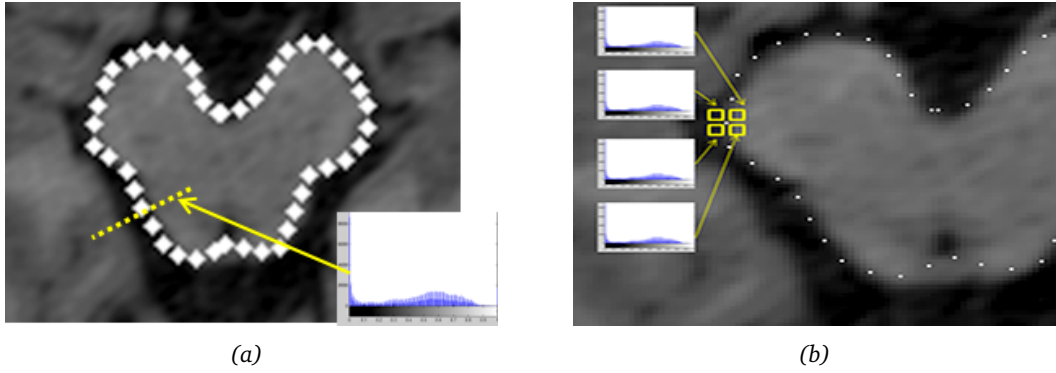


Figure 4.3: Two different ways to combine LBPs with ASMs. **(a)** LBP's histogram for each profile landmark of the contour; and **(b)** Quadratic LBP's histogram for each contour landmark.

is the histogram used to modify the landmark position to the desired border based on a histogram's distance.

Both methods take into account the original ASM's profile-based search but instead of getting a distance of the gray values or combination of derivative gray values, the histograms are compared against the one of the PDM training model. Chi distance is used to compute similarities between the new test object histogram, H and the training histogram, \bar{H} . The smallest distance is where the point boundary moves. The smaller the distance, the more similar is the test region where the boundary is located, and it leads to a better segmentation as follows:

$$X^2(H, \bar{H}) = \sum_i \frac{(H_i - \bar{H}_i)^2}{(H_i + \bar{H}_i)} \quad (4.6)$$

The simplest algorithm starts by obtaining the profile of the landmark point and then calculates its LBP histogram for each profile point. The point with the smallest Chi distance is to where the contour moves.

In addition, we also evaluated the behavior of three LBP techniques: the uniform LBP, Eq. (4.3), the number LBP, Eq. (4.4), and the median LBP, Eq. (4.5) with the ASM to compare their performance with the simple LBP defined in the Eq. (4.1). The LBP methods perform a 360 degrees calculus of each pixel inside the evaluated area. This means that all the pixels supply component values to the resulting histogram, independently if it is profile or divided quadratic region. The result is a more thorough histogram of the gray values existent within the area.

4.5 Experimental results

The proposal was evaluated on 10 slices of the midbrain volume using both the ASM/LBP profile and ASM/LBP quadratic schemes explained in the previous section. Once the volume is segmented, the results are compared against the expert segmented data. Dice index, Eq. (4.7), and Hausdorff

Table 4.1: Dice index and Hausdorff distance for the classic ASM. Dice value is between 0 and 1, values close to 1 indicate more similar contours. On the contrary, Hausdorff minimal values indicate more alike boundaries, in mm^2 . Bold values are the best values.

| ASM | | |
|---------------|-------------------------|-------------------------|
| slice | Dice | Hausdorff |
| 1 | 0.6619 | 3.6936 |
| 2 | 0.8441 | 2.6402 |
| 3 | 0.6652 | 3.7170 |
| 4 | 0.8342 | 1.9328 |
| 5 | 0.8984 | 1.9681 |
| 6 | 0.4632 | 5.1787 |
| 7 | 0.5044 | 3.9688 |
| 8 | 0.4604 | 6.8810 |
| 9 | 0.7563 | 2.9580 |
| 10 | 0.8833 | 1.6156 |
| $\mu(\sigma)$ | 0.6971 (± 0.1730) | 3.4553 (± 1.6303) |

distance, Eq. (4.8), were chosen as the comparison measures, and they obtained a value for each ASM/LBP scheme and for the ASM algorithm, as well as for each slice of the volume. The Dice index, d_D , uses the intersected area between the expert and recognized contours divided by the sum of both areas. The result is a normalized value between 0 and 1 that indicates how similar are both contours. The closest the value is to 1 the more similar the shapes are. The equation is defined as follows:

$$d_D = \frac{2 \times (|A \cap B|)}{(|A| + |B|)} \quad (4.7)$$

The Hausdorff distance, d_H , measures how close a point from a first set is from another point of the second set in a metric space –in our case between two sets of points, P and Q (or boundaries). It is defined as follows:

$$d_H(P, Q) = \max \{d(P, Q), d(Q, P)\} \quad (4.8)$$

where $d(P, Q) = \min \{\|p_{max} - q\| \mid p_{max} \in \max \{\|p - q\|\}, q \in Q, p \in P\}$; intuitively, $d(P, Q)$ finds the p point from the set P that is the farthest from any point in Q and measures the distance from p to its closest neighbor in Q .

Table 4.1 shows both Dice index and Hausdorff metric for the ASM algorithm. Note that the slice 8 provided the largest error.

Table 4.2 and Table 4.3 summarize the results of Dice index and Hausdorff metric obtained for the profile ASM/LBP scheme, respectively; whereas Table 4.4 and Table 4.5 summarize the results

Table 4.2: Dice index for the profile ASM/LBP scheme using the original LBP, uniform LBP, number LBP, and median LBP. Dice value is between 0 and 1, values close to 1 indicate more similar contours. Bold values are the best per slice

| slice | ASM/LBP | ASM/LBP _{P,R} ^{uni} | ASM/LBP _{P,R} ^{num} | ASM/LBP _{P,R} ^{med} |
|---------------|------------------------|---------------------------------------|---------------------------------------|---------------------------------------|
| 1 | 0.9500 | 0.9468 | 0.9359 | 0.9535 |
| 2 | 0.9376 | 0.9474 | 0.9434 | 0.9066 |
| 3 | 0.9494 | 0.9441 | 0.9199 | 0.9452 |
| 4 | 0.9661 | 0.9497 | 0.9456 | 0.9618 |
| 5 | 0.9469 | 0.9353 | 0.9363 | 0.8658 |
| 6 | 0.9605 | 0.8851 | 0.8856 | 0.9560 |
| 7 | 0.9391 | 0.9357 | 0.9305 | 0.7320 |
| 8 | 0.9162 | 0.5949 | 0.7149 | 0.8921 |
| 9 | 0.9183 | 0.8918 | 0.6572 | 0.9478 |
| 10 | 0.9294 | 0.8878 | 0.8953 | 0.9391 |
| $\mu(\sigma)$ | 0.9414(± 0.0166) | 0.8919(± 0.1076) | 0.8765(± 0.1032) | 0.9100(± 0.0700) |

Table 4.3: Hausdorff distance for the profile ASM/LBP using the original LBP, uniform LBP, number LBP, and median LBP. Hausdorff minimal values indicate more similar boundaries, in mm². Bold values are the best per slice.

| slice | ASM/LBP | ASM/LBP _{P,R} ^{uni} | ASM/LBP _{P,R} ^{num} | ASM/LBP _{P,R} ^{med} |
|---------------|------------------------|---------------------------------------|---------------------------------------|---------------------------------------|
| 1 | 0.8312 | 0.8415 | 1.0646 | 0.7687 |
| 2 | 1.1979 | 0.9812 | 1.0474 | 1.7953 |
| 3 | 0.9872 | 1.0121 | 0.9548 | 1.2126 |
| 4 | 0.7408 | 0.7249 | 0.8460 | 0.8060 |
| 5 | 1.2643 | 1.3455 | 1.1682 | 1.9938 |
| 6 | 0.6104 | 1.9661 | 1.8745 | 0.7254 |
| 7 | 1.0025 | 1.0241 | 0.9421 | 3.8828 |
| 8 | 1.3612 | 3.9407 | 4.4649 | 1.3170 |
| 9 | 1.5335 | 1.4980 | 5.1571 | 1.1066 |
| 10 | 1.1597 | 1.3497 | 1.9533 | 0.8370 |
| $\mu(\sigma)$ | 1.0688(± 0.2886) | 1.4683(± 0.9415) | 1.9473(± 1.5652) | 1.4445(± 0.9605) |

of Dice index and Hausdorff metric obtained for the quadratic ASM/LBP scheme, respectively.

Fig.4.4 to Fig.4.6 show as a representative set, the resulted segmentation for slice 4 on each of the proposed methods.

One remark from this research is that while the ASM sometimes fails due to the lack of enough

Table 4.4: Dice index for the quadratic ASM/LBP scheme using the original LBP, uniform LBP, number LBP, and median LBP. Dice value is between 0 and 1, values close to 1 indicate more similar contours. Bold values are the best per slice

| slice | ASM/LBP | ASM/LBP _{P,R} ^{uni} | ASM/LBP _{P,R} ^{num} | ASM/LBP _{P,R} ^{med} |
|---------------|------------------------|---------------------------------------|---------------------------------------|---------------------------------------|
| 1 | 0.9561 | 0.9583 | 0.9517 | 0.9567 |
| 2 | 0.9518 | 0.9475 | 0.9513 | 0.9527 |
| 3 | 0.9479 | 0.9476 | 0.9294 | 0.9318 |
| 4 | 0.9642 | 0.9583 | 0.9636 | 0.9628 |
| 7 | 0.9382 | 0.9393 | 0.8729 | 0.9382 |
| 6 | 0.9605 | 0.9619 | 0.9499 | 0.9615 |
| 7 | 0.9445 | 0.9407 | 0.7624 | 0.9458 |
| 8 | 0.9212 | 0.9188 | 0.9201 | 0.9199 |
| 9 | 0.9405 | 0.9278 | 0.9352 | 0.9399 |
| 10 | 0.9563 | 0.9539 | 0.9515 | 0.9562 |
| $\mu(\sigma)$ | 0.9481(± 0.0127) | 0.9454(± 0.0140) | 0.9188(± 0.0607) | 0.9465(± 0.0140) |

Table 4.5: Hausdorff distance for the quadratic ASM/LBP scheme using the original LBP, uniform LBP, number LBP, and median LBP. Hausdorff minimal values indicate more similar boundaries, in mm². Bold values are the best per slice.

| slice | ASM/LBP | ASM/LBP _{P,R} ^{uni} | ASM/LBP _{P,R} ^{num} | ASM/LBP _{P,R} ^{med} |
|---------------|------------------------|---------------------------------------|---------------------------------------|---------------------------------------|
| 1 | 0.7332 | 0.7148 | 0.7944 | 0.7349 |
| 2 | 0.8897 | 0.9873 | 0.9167 | 0.8906 |
| 3 | 0.9800 | 0.9857 | 1.3927 | 1.3362 |
| 4 | 0.8565 | 0.7364 | 0.8748 | 0.8724 |
| 7 | 1.4730 | 1.4694 | 2.1317 | 1.4796 |
| 6 | 0.6145 | 0.5916 | 0.7467 | 0.5909 |
| 7 | 1.1109 | 1.0065 | 3.8951 | 1.0915 |
| 8 | 1.1999 | 1.1888 | 1.2018 | 1.2010 |
| 9 | 1.2096 | 1.1768 | 1.0661 | 1.2027 |
| 10 | 0.8931 | 0.8681 | 0.9943 | 0.9270 |
| $\mu(\sigma)$ | 0.9960(± 0.2547) | 0.9725(± 0.2614) | 1.4014(± 0.9648) | 1.0326 (± 0.2775) |

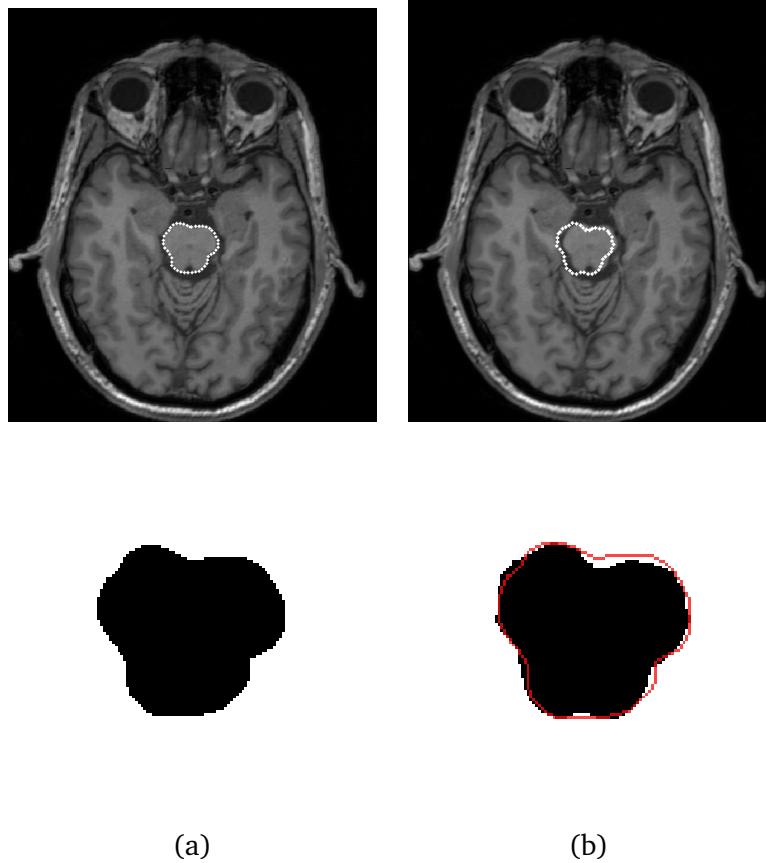


Figure 4.4: Cranial MR images; the first row shows axial original view and second row shows binary midbrain segmentation; binary images were augmented 2X for a better visualization. **(a)** expert annotated boundary; and **(b)** classic ASM recognized boundary; the red contour in binary image indicates the expert boundary.

training set and parameters variance, the ASM/LBP improves its result with more certainty and less iterations. This is due to the deeper analysis of the surrounding texture of the boundary and the way we move the final points to the desired boundary.

In both cases, profile and quadratic schemes, the join model provides a better adjustment starting from the initial iterations. And it does not need as many initial training data and/or diminishes the number of iterations compared to the traditional ASM.

Figure 4.7 shows the segmentation of 10 frames correspondant to the mesencephalon.

4.6 Remarks

In this chapter an improved algorithm based on ASMs is proposed, which incorporates the use of LBPs in order to obtain a better segmentation of midbrain volumes. Four different LBP approaches are created and tested: original LBP, uniform LBP, numeric LBP, and median LBP. An evaluation compared their performance using midbrain's Magnetic Resonance images. Obtaining the best



Figure 4.5: Profile ASM/LBP scheme midbrain segmentation; binary images were augmented 2X for a better visualization. The red contour indicates the expert boundary. (a) ASM/LBP; (b) ASM/LBPuni; (c) ASM/LBPnum; and (d) ASM/LBPmed



Figure 4.6: Quadratic ASM/LBP scheme midbrain segmentation; binary images were augmented 2X for a better visualization. The red contour indicates the expert boundary. (a) ASM/LBP; (b) ASM/LBPuni; (c) ASM/LBPnum; and (d) ASM/LBPmed

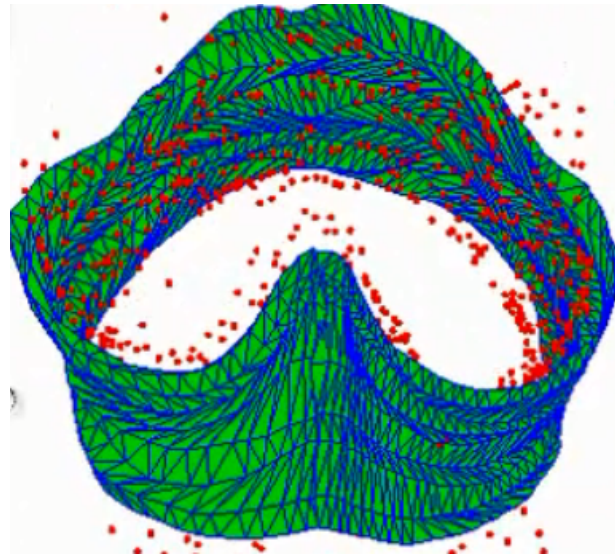


Figure 4.7: Segmentation over multiple midbrain slices.

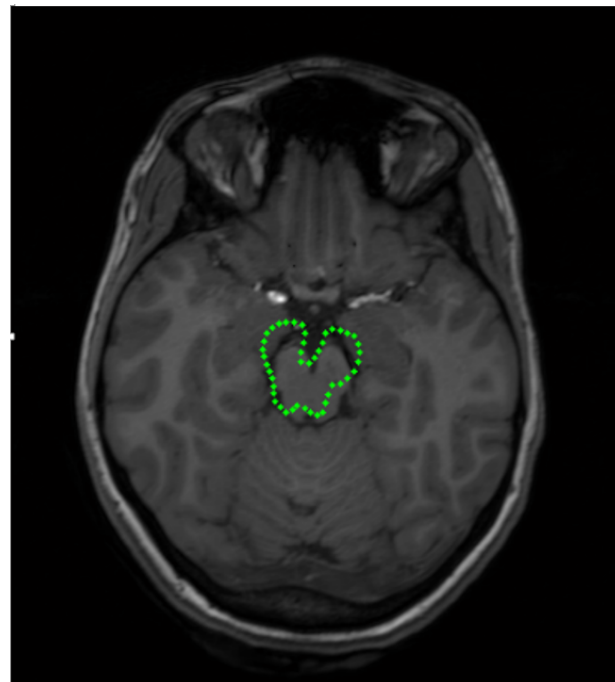


Figure 4.8: ASM/LBP scheme, that does not converge correctly.

results using first the quadratic LBP algorithm, second the profile LBP, and lastly the classic ASM method. Also can be noticed that in the case of the profile ASM/LBP scheme the semiautomatic process for the initial position is very important and can vary the results, which did not happen in the quadratic ASM/LBP scheme. For the ASM, this fact causes not to converge correctly as can be seen in Figure 4.8. Even though there was not enough data to test the algorithm, the quadratic ASM/LBP shows a major performance compared to the other methods. This is due to the fact that a bigger area that characterizes the midbrain contour is analyzed.

This chapter showed an advance on how to combine textural information with the ASM algorithm in order to improve results. The next chapter shows the main alternative to include local information, that is based on the Hermite Transform and it is also compared against LBPs performance. These methods are applied on the segmentation of Left ventricle's heart.

5

Heart's left ventricle segmentation based on active contours

Cardiac computed tomography (CT), nuclear cardiology, echocardiography, cardiovascular magnetic resonance (CMR), positron emission computed tomography (PET), and coronary angiography are imaging modalities that have been used to measure myocardial perfusion, left ventricular function, and coronary anatomy for clinical management and research. The practical clinical application of these modalities depends heavily on their specific inherent strengths and weaknesses. This large variety of imaging techniques has resulted in a lack of standardization and has made accurate intra- and cross-modality comparisons for clinical patient management and research very difficult.

MR technology offers high resolution and SNR among other characteristics, however it is an expensive alternative that few hospitals can afford. Computer tomography has the advantage of being more accessible. In the X-ray technology the calibration curves needed are well known, while in MR there are large characteristic variations to take into account for its procedures.

One of the most important tasks in cardiology is the left ventricle segmentation. Its segmentation is traditionally made manually by an expert looking at gray intensity changes to define a contour. This is the case in ultrasound, CT, MRI, or PET. However manual segmentation of heart cavities is a difficult and time-consuming task.

Some of the more difficult problems of automatic segmentation include poor image quality, low contrast and poor structure border detection. Moreover cardiac anatomy and gray value

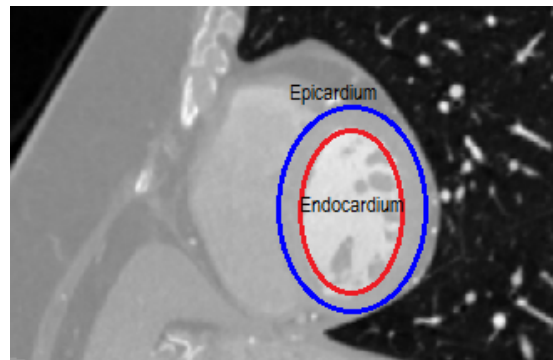


Figure 5.1: *CT image of the heart displayed using the short axis view where it is possible to see the right and left ventricles. The red ellipse defines the endocardium, whereas the blue ellipse defines epicardium. This segmentation resembles typical boundaries drawn by clinicians.*

distribution of the images varies from person to person, especially when a cardiopathy exists. These facts represent a difficult challenge for the development of more sophisticated tools.

As a prerequisite for Left Ventricle (LV) visualization, the heart must be oriented in order to obtain a canonical view: horizontal, long, and short axis views. The short axis view shows a plane that is perpendicular to the long axis and gives a suitable cross-sectional view of both ventricles [56, 57]. On the short axis view, the LV is aligned vertically from the base of the heart to the apex, see Figure 5.1.

Most medical segmentation algorithms are created for magnetic resonance images because of the good contrast offered by this technology. Although CT imaging does not provide suitable contrast resolution in comparison with MRI, it is far more accessible and has enough spatial resolution to distinguish adjacent organs [58]. In addition, is a growing tendency for the cardiac CT studies because of its cost [59] and other advantages.

Several techniques have been developed for epicardium and endocardium segmentation using the short axis view. Petitjean and Dacher [2] presented a review of a large group of automated and semi-automated segmentation methods. The review includes methods based on atlases, deformable models such as level sets (LS) and statistical models with prior knowledge such as active shape models (ASM). However, these methods are focused on MRI. Kang et al. [1] also wrote a review about the most used methods in cardiac segmentation. However, classic active contours and level sets are associated with a minimum functional, which often leads to over-segmentation [60].

It is well-known that CT-based heart segmentation is sensitive to initialization, noise, and image characteristics. Therefore, other studies have suggested that the combination of different techniques may improve organ segmentation [16, 61–63]. For instance, in [6], the authors improved the weighted C-means clustering [64] with a fitting model. In [16], Kronman et al. proposed an adjustment to the segmentation by using active contours based on level sets and a correction of the segmentation leaks using a ray casting method. Ma et al. [5] used a Haar classifier to detect the heart area. Then, the segmentation is performed with an ASM. Dolz et al. [65]

5.1 Texture descriptor approaches to level set segmentation in medical images

showed a hybrid approach combining a watershed transformation with graph-cut segmentation in order to delineate organs such as the spinal canal, lungs, heart, and pericardium. Antunes et al. [7] used level sets to extract the cardiac surface from multi-detector computed tomographic data. The authors coupled a 3D level set with a stopping function based on a multi-scale second derivative Gaussian filter. The results show that the combination of methods outperforms single approaches.

Local binary patterns (LBPs) have proven to be a suitable tool when they are used in combination with active contours because LBPs are able to model local structures in a robust way against illumination changes, while ASMs take advantage of the velocity of local variations to localize landmarks [55]. Features such as texture, color, or morphology should be included in a deeper analysis in order to enhance the performance of the final segmentation (e.g. in Olveres et al. [66] an application to mesencephalon segmentation).

On the other hand, methods that resemble the human visual system have increased in popularity because they allow images to expand into a local decomposition that describes intrinsic attributes related to important cues and highlights structures that are useful for segmentation [45]. The Hermite transform (HT) [38, 41] has been used successfully as a texture descriptor in [67, 68]. HT is a special case of the Polynomial transform and is based on Gaussian derivatives, thus, it is possible to compute local orientation analysis.

On this chapter two approaches are proposed in order to improve actual segmentation on cardiac computed tomography studies with local analysis. Now instead of using ASMs and in order to research new segmentation methods, the first approach applied Chan Vese level sets to endocardium, using steered Hermite information. The second approach was applied on endocardium and epicardium, and is based on various active contour algorithms also using steered Hermite coefficients as local information.

The resulted paper [69] of this section was published as one of the problems address in the present PhD project.

5.1 Texture descriptor approaches to level set segmentation in medical images

The left ventricle (LV) inner wall or endocardium segmentation is frequently executed by an expert to quantify left ventricular blood flow. This is an important issue because changes of volume or flow are related to cardiac function and can imply –under certain conditions– a disease. In cardiovascular physiology, the volume of blood pumped from a heart’s ventricle is generally calculated using measurements from an echo-cardiogram. The volume of blood in the ventricle at the systolic phase is subtracted from the volume of blood just prior to the beat (called end-diastolic phase). The stroke volume is a measure usually taken on the left ventricle. The left ventricular outflow view delineates the inflow and outflow tracts and is useful to assess motion of the mitral and aortic valves or septum changes in some obstructive cardiomyopathies [57]. One way to

extract such a volume in cardiac computed tomography is measuring the area of the ventricle cavity for each slice created of the volume and then calculate the total volume. However, noise inherent to computerized tomographic images and the lack of contrast may hamper the final segmentation, thus, it is necessary to include more characteristics that support the algorithm decision.

Texture plays an important role in distinguishing one region from another because intensity variations may reflect different areas, shapes, or objects. Based on the fact that texture possesses spatial continuity at both local and global scales and can exhibit a large number of features, it has been widely used to perform segmentation. The occurrence of texture in an image is useful because when two or more regions meet an edge is formed. This fact was used as an advantage by using a combined approach of level sets and local texture descriptors. In general, CT possesses homogeneous textures within organs, and this fact supports good definition of borders, but in some occasions this textures can look very similar.

Heart left ventricle has a circular aspect from the short axis view. Also right and left ventricular motions can be visualized from the short axis view and it is the basis for volumetric measurements used in global ventricular function evaluation. Typical segmentation of the inner part of the ventricle includes papillary muscles which leads to an incorrect measure of the ejected volume. If the final segmentation excludes most part of such muscles, specially those next to the endocardium, it could get to a more precise measure of the total blood volume. The level set vector value approach is used without any prior information, for LV segmentation in CT images, and propose a novel strategy that combines level sets and Hermite features that are included in the evolving equation to refine the segmentation of the endocardium wall. In this work, a nonlinear diffusion strategy is chosen for building the vector features that are introduced into the level set equation as in [27]. Also an evaluation of several alternative texture descriptors was performed in order to compare the proposal.

Another work to mention is the one of Barba et al. [70], their study is posterior to this proposal, but is worth to mention that they use Active Shape Models to create an spatio-temporal point distribution model. However the deformable scheme combines the three types of image features in order to correct errors, not as part of the algorithm, the posterior improvement of the segmentation performance uses local histograms, gradients and binary patterns.

5.1.1 THE COMBINED PROPOSAL

The main purpose is to obtain a segmentation of the left ventricle, and level sets were used to evolve an active contour and to find a desired boundary within an image. Active contours for vector-valued images were introduced by Chan and Vese and they used level sets [25], see Chapter 2, which is important to describe the development of this theory. The Hermite transform (HT) is proposed as a texture descriptor that can be included as in the next Eq. 5.1.

The vector-value model for Chan-Vese (VVCV) proposed in [25] uses K -extra information in

order to obtain a better segmentation.

$$\begin{aligned} \frac{\partial \phi}{\partial t} = \delta(\phi) & \left[\mu \operatorname{div} \left(\frac{\nabla \phi}{|\nabla \phi|} \right) - \frac{1}{K} \sum_{i=1}^K \lambda_i^+ (I_i(\bar{x}) - c_i^+)^2 \right. \\ & \left. + \frac{1}{K} \sum_{i=1}^K \lambda_i^- (I_i(\bar{x}) - c_i^-)^2 \right], \end{aligned} \quad (5.1)$$

where c^+ and c^- are constant vectors that represent the average value of one of the K layers of I_i inside and outside the curve C , respectively. The parameters λ_i^+ and λ_i^- are constant weights defined manually for the user and further discussed in the experimental results section. We will consider in this study planar images.

The solution of Equation (5.1) achieves a convergence by checking whether the solution is stationary. Setting a threshold is used to verify if the energy is not changing or if the contour is not moving too much between two iterations, such threshold can be found intuitively or experimentally. Another very used criterion to stop the curve evolution is to manually define a stopping term with a large number of iterations, this assumption considers that the desired contour will be obtained at the end of the process, similarly to obtaining a global minima.

In this case, the K layers of I_i will be composed by the Hermite Coefficients obtained from the Hermite Transform, and/or the proposed texture descriptors described in the next sections.

5.1.2 OTHER TEXTURE DESCRIPTORS

Gray level information (GRAY) is the initial feature vector and its performance is compared against Hermite features. The experiments also included other texture descriptors such as image derivatives, local binary patterns, and Hounsfield values as components of the feature vector. The following paragraphs show their description.

- *Hounsfield information.* As part of the nature of the images in cardiac computed tomography, the attenuation values given by Hounsfield information are of great interest. Such values depend on the CT attenuation method and the contrast agent. Low attenuation values of left ventricle may vary between 300 and 600 Hounsfield units (HU), thus, a method that segments left ventricle by using a threshold based on Hounsfield values is proposed. Pixels between 300 and 600 HU are marked as left ventricle; otherwise are set to zero.
- *Image derivatives* [27] are used as part of a linear structure tensor that defines texture features as follows:

$$\mathbf{J}_0 = (\nabla I \nabla I^T) = \begin{bmatrix} I_x^2 & (I_x I_y) \\ (I_x I_y) & I_y^2 \end{bmatrix} \quad (5.2)$$

where I is the given image and the subscripts denote partial derivatives.

- **Uniform Local Binary Patterns (LBPU)** [52]. This approach is based on the idea that textural properties within homogeneous regions can be mapped into patterns that represent micro-features. It uses a circular mask denoted by the subscript (P, R) where P is the number of sampling points around a central pixel, g_c , and R is the radius of the neighborhood, (see Figure 5.2). If the sampling coordinates, $(x_p, y_p) = (x_c + R \cos(\frac{2\pi p}{P}), y_c - R \sin(\frac{2\pi p}{P}))$, do not fall at integer positions then the values are bilinearly interpolated.

Since over 90% of such patterns can be described with few spatial transitions, that are the changes (0/1) in the pattern chain, the descriptor introduces a uniformity measure $U(g_c) = |s(g_{P-1} - g_c) - s(g_0 - g_c)| + \sum_{p=1}^{P-1} |s(g_p - g_c) - s(g_{p-1} - g_c)|$ where $\{g_p | p = 0, \dots, P-1\}$ are the neighbors of g_c and $s(x) = \begin{cases} 1 & \text{if } x \geq 0 \\ 0 & \text{if } x < 0 \end{cases}$.

So that, the LBPU can be obtained as:

$$LBPU_{P,R}(g_c) = \begin{cases} \sum_{p=0}^{P-1} s(g_p - g_c) & \text{if } U(g_c) \leq 2 \\ P + 1 & \text{otherwise} \end{cases} \quad (5.3)$$

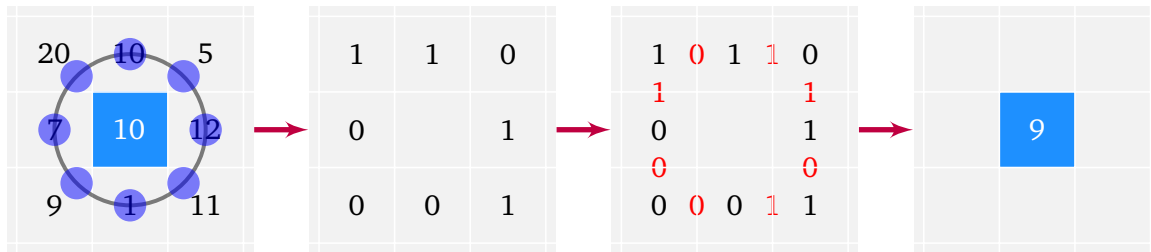


Figure 5.2: Based on a circular mask, the LBPU algorithm computes comparisons between a central pixel and its surrounding neighbors. In this example, the central value is $p_c = 10$ and the final label is 9.

- **BRINT.** An important disadvantage of CT images is the random noise, due to the fact that X-ray photons strike on a surface, such as an image detector, in a random pattern. That limits the ability of the radiologist to discriminate between two regions of different density. Since LBPs and its variants are very sensitive to noise, Liu et al. [71] proposed a simple modification based on the LBPU called Binary Rotation Invariant and Noise Tolerant (BRINT) that averages the sampling points before binarization. The authors transformed the neighbor vector in order to reduce the effects of noise, (see Figure 5.3).

5.1.3 MATERIALS

Five cardiac computed tomography studies from 5 different patients were used. Such studies were performed on a CT Siemens dual source scanner with 128 channels. Each study contains 10 volumes that correspond to time percentage of the cardiac cycle. None of them contain personal

5.1 Texture descriptor approaches to level set segmentation in medical images

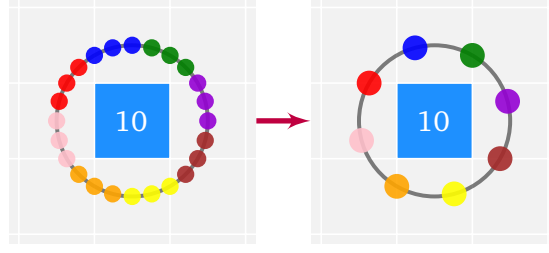


Figure 5.3: BRINT averages the sampling points around a central pixel before binarization. First, It transforms the original neighborhood ($P=24$) into a new one ($P=8$) by averaging the 3 adjacent neighbors to generate a binary pattern.

information. Originally, the volumes were not aligned with the traditional short axis view. However, the volumes need to be aligned with respect to axial and sagittal human body's axes [57]. To obtain these views it is necessary at least rotate 2 of the axes of the tomographic representation and execute a series of translations. In a mathematical form this representations are defined by 6 parameters in matrix operations: 3 for translations and 3 for rotations on the orthogonal axes. The matrix defined for translation is given by:

$$S_{m,n} = \begin{bmatrix} 1 & 0 & 0 & xtrans \\ 0 & 1 & 0 & ytrans \\ 0 & 0 & 1 & ztrans \\ 0 & 0 & 0 & 1 \end{bmatrix} \quad (5.4)$$

while the matrices defined for rotations with θ radians on the X, Y, and Z axes are:

$$X_{m,n} = \begin{bmatrix} 1 & 0 & 0 & 0 \\ 0 & \cos(\theta) & \sin(\theta) & 0 \\ 0 & -\sin(\theta) & \cos(\theta) & 0 \\ 0 & 0 & 0 & 1 \end{bmatrix}, Y_{m,n} = \begin{bmatrix} \cos(\theta) & 0 & \sin(\theta) & 0 \\ 0 & 1 & 0 & 0 \\ -\sin(\theta) & 0 & \cos(\theta) & 0 \\ 0 & 0 & 0 & 1 \end{bmatrix}, Z_{m,n} = \begin{bmatrix} \cos(\theta) & \sin(\theta) & 0 & 0 \\ -\sin(\theta) & \cos(\theta) & 0 & 0 \\ 0 & 0 & 1 & 0 \\ 0 & 0 & 0 & 1 \end{bmatrix} \quad (5.5)$$

note that the order of the matrix operations affects the result. So it is important to take it into account while transforming the volumes.

5.1.4 EXPERIMENTS AND RESULTS

In order to assess the performance of this proposal the SHT, namely Hermite filter is used as a texture descriptor on the left ventricle endocardium. Several texture descriptors were reviewed in combination with the original image (or plain level set) called "GRAY". The combinations employed were: 1) gray values belonging to the original image; 2) Image derivatives + GRAY; 3) Hermite filter with $N = 3$ + GRAY; 4) Hermite filter with $N = 5$ + GRAY; 5) Hermite filter with $N = 9$ + GRAY; 6) Uniform LBP with ($P=16, R=2$) + GRAY; 7) Multiresolution LBP with (P, R) values of (1,8), (2,16) and (3,24) + GRAY; 8) BRINT + GRAY; and 9) Hounsfield values + GRAY.

A comparison with the performance of the proposal is included (Hermite filters with different window sizes) with a manual segmentation along the cardiac cycle, (see Figure 5.4) and also included segmentation results of the descriptors previously presented in Section 5.1.2. The computation was performed using a middle slice, and each percentage of the cardiac cycle is processed sequentially, followed by sequential processing of each algorithm. The images for each cardiac phase are calculated independently. First, the myocardium is located by calculating the centroid of the LV blood pool on the middle slice at the first phase. Second, the algorithm is applied through all the phases.

In general a better performance was obtained using Hermite filters. Notice that the endocardial and papillary muscles are detected by applying this proposal, (see Figure 5.4); the boundaries are more adjusted and give the robustness needed to detect non-salient boundaries in the presence of noise. The result was a contour boundary able to enhance the structure adjustments to the endocardium walls.

A manual segmentation is created as a *ground truth* and compared it with all the methods using the Dice index and Hausdorff distance. Dice metric d_D is a measure of contour overlap given by the equation Eq. (4.7) from chapter 4. And as it was also mentioned the Hausdorff distance, d_H , measures how close a point from a first set is from another point of the second set in a metric space, in this case between two sets of points, P and Q (or boundaries). It was defined by Eq. (4.8).

The results across all subjects using Dice index are shown in Table 5.1, while the results using Hausdorff distance are shown in Table 5.2. The tables also present specific values to each percentage time of the cardiac cycle. Even when there are good results in some of the experiments, notice how the values improve when texture descriptors are applied. Regarding LBPs and Hounsfield based methods, they did not work as expected. Specially attention is taken at the ones obtained for the Hermite9 and GRAY in order to compare it.

In order to quantitatively evaluate the automatically detected endocardium, the volume (blood volume) for the analyzed slide was computed. All of the descriptor method results are compared against a manual boundary contour, see from Figure 5.5 to Figure 5.13. Also plotted results of all the cardiac cycle percentages or time phases for one patient are shown, notice where the blood pool is correctly localized and distinguished. Similar results were obtained for the rest of the patients.

5.1.5 FINAL COMMENTS

The segmentation of the left ventricle presented in this work constitutes a way to understanding the complex heart dynamics by segmenting the left ventricle endocardium and obtaining precise quantitative measures by taking advantage of the temporal information. And more comments about the work are given on the final Conclusions, Chapter 7.

5.1 Texture descriptor approaches to level set segmentation in medical images

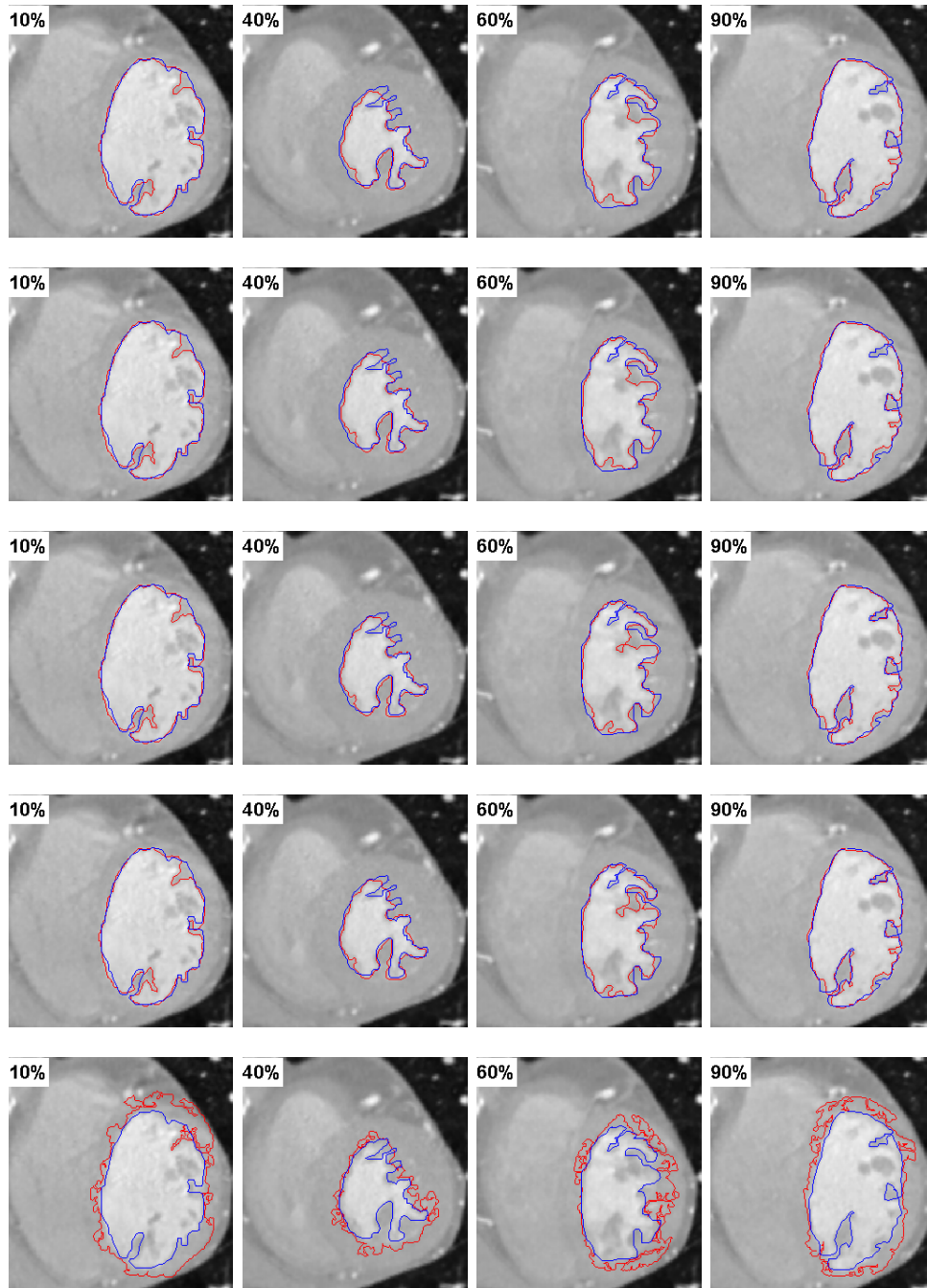


Figure 5.4: Segmentation comparisons between a manual contour (blue) and the level set method (red) using: GRAY (first row), Hermite3 + GRAY (second row), Hermite5 + GRAY (third row), Hermite9 + GRAY (fourth row), and LBPU + GRAY (fifth row). The numbers on the images indicate the percentage of the cardiac cycle.

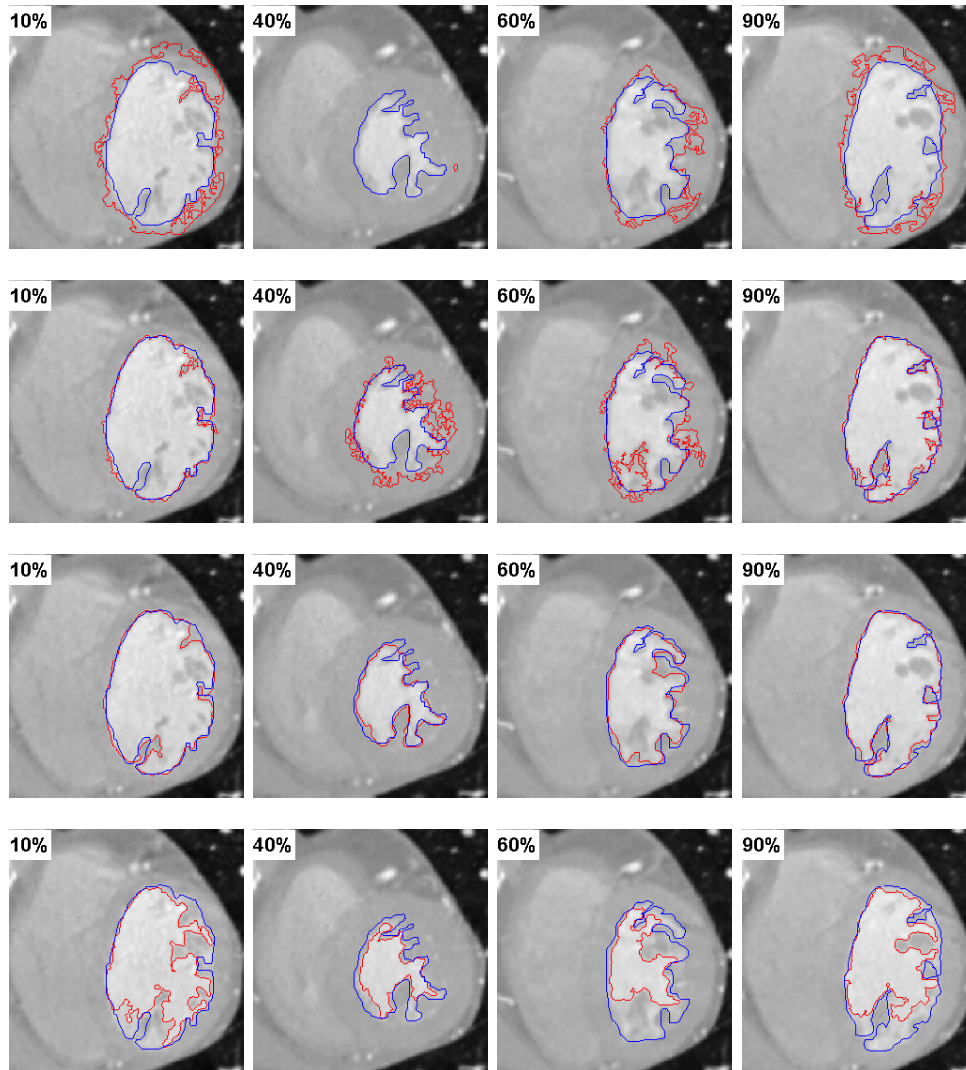


Figure 5.4: Continuation... Segmentation comparisons between a manual contour (blue) and the level set method (red) using: LBPUM + GRAY (**first row**), BRINT + GRAY (**second row**), Image derivatives + GRAY (**third row**), and Hounsfield values + GRAY (**fourth row**). The numbers on the images indicate the percentage of the cardiac cycle.

5.1 Texture descriptor approaches to level set segmentation in medical images

Table 5.1: Dice index results. Dice index is between 0 and 1, values close to 1 indicate more similar contours. Values 10, 20, 30, ..., represent the percentages of the CT volumes taken during the cardiac cycle. LBPUM represents a combination of three LBPU: {P=8,R=1}, {P=16,R=2}, and {P=24,R=3}. The values represent the average index on all the patients.

| Method | Cardiac Cycle (%) | | | | | | | | | |
|-------------|-------------------|---------------|---------------|---------------|---------------|---------------|---------------|---------------|---------------|---------------|
| | 10 | 20 | 30 | 40 | 50 | 60 | 70 | 80 | 90 | 100 |
| Gray | 0.9555 | 0.9354 | 0.9101 | 0.9196 | 0.9261 | 0.9005 | 0.9033 | 0.9268 | 0.9404 | 0.9362 |
| Hermite3 | 0.9543 | 0.9484 | 0.9129 | 0.9220 | 0.9254 | 0.9090 | 0.9027 | 0.9333 | 0.9380 | 0.9351 |
| Hermite5 | 0.9525 | 0.9483 | 0.9111 | 0.9208 | 0.9257 | 0.9105 | 0.9015 | 0.9337 | 0.9377 | 0.9348 |
| Hermite9 | 0.9533 | 0.9486 | 0.9144 | 0.9218 | 0.9246 | 0.9121 | 0.8998 | 0.9346 | 0.9371 | 0.9336 |
| LBPUM | 0.8169 | 0.6922 | 0.6303 | 0.7250 | 0.5863 | 0.7752 | 0.7823 | 0.6671 | 0.8181 | 0.8517 |
| LBPUM | 0.6470 | 0.7798 | 0.7446 | 0.5843 | 0.7605 | 0.8057 | 0.7860 | 0.8374 | 0.8244 | 0.8262 |
| BRINT | 0.7190 | 0.8704 | 0.7659 | 0.5656 | 0.7621 | 0.8234 | 0.8243 | 0.8466 | 0.8744 | 0.8758 |
| Derivatives | 0.9551 | 0.9383 | 0.9111 | 0.9205 | 0.9262 | 0.9063 | 0.9028 | 0.9277 | 0.9371 | 0.9359 |
| Hounsfield | 0.7228 | 0.6935 | 0.7225 | 0.7786 | 0.8366 | 0.7626 | 0.6894 | 0.7817 | 0.8354 | 0.7213 |

Table 5.2: Hausdorff distance results. Lowest values indicate more alike boundaries in mm^2 . Values 10, 20, 30, ..., represent the percentages of the CT volumes taken during the cardiac cycle. LBPUM represents a combination of three LBPU: {P=8,R=1}, {P=16,R=2}, and {P=24,R=3}. The values represent the average distance on all the patients.

| Method | Cardiac Cycle (%) | | | | | | | | | |
|-------------|-------------------|---------------|---------------|---------------|---------------|---------------|---------------|---------------|---------------|---------------|
| | 10 | 20 | 30 | 40 | 50 | 60 | 70 | 80 | 90 | 100 |
| Gray | 2.8854 | 3.0465 | 3.1575 | 1.9582 | 2.0806 | 3.4555 | 3.0240 | 3.7724 | 2.6179 | 3.4750 |
| Hermite3 | 2.5847 | 2.3205 | 2.8517 | 1.9238 | 1.7440 | 3.1670 | 2.9193 | 3.7129 | 2.5775 | 3.5003 |
| Hermite5 | 2.7134 | 2.4376 | 2.8395 | 2.0690 | 1.7489 | 3.4164 | 2.9080 | 3.3441 | 2.1589 | 3.1869 |
| Hermite9 | 2.7088 | 2.4715 | 2.6186 | 2.0367 | 1.7618 | 3.4937 | 2.9212 | 3.3767 | 2.1686 | 3.7777 |
| LBPUM | 5.8222 | 8.6218 | 7.2552 | 4.9062 | 6.6065 | 5.1270 | 4.8705 | 7.2012 | 6.8517 | 5.7507 |
| LBPUM | 9.4675 | 6.8102 | 5.4290 | 7.1672 | 4.2299 | 4.7647 | 5.1470 | 5.0158 | 6.2481 | 6.5403 |
| BRINT | 7.9923 | 3.5218 | 4.2532 | 8.4240 | 3.5333 | 4.2317 | 4.1693 | 3.7411 | 4.4484 | 5.0129 |
| Derivatives | 2.9443 | 3.0233 | 3.1579 | 1.9588 | 1.9543 | 3.2197 | 2.9834 | 3.7482 | 2.5772 | 3.4599 |
| Hounsfield | 7.2849 | 8.1037 | 6.0732 | 4.3212 | 3.0081 | 5.1040 | 7.3877 | 5.8386 | 5.3513 | 7.5457 |

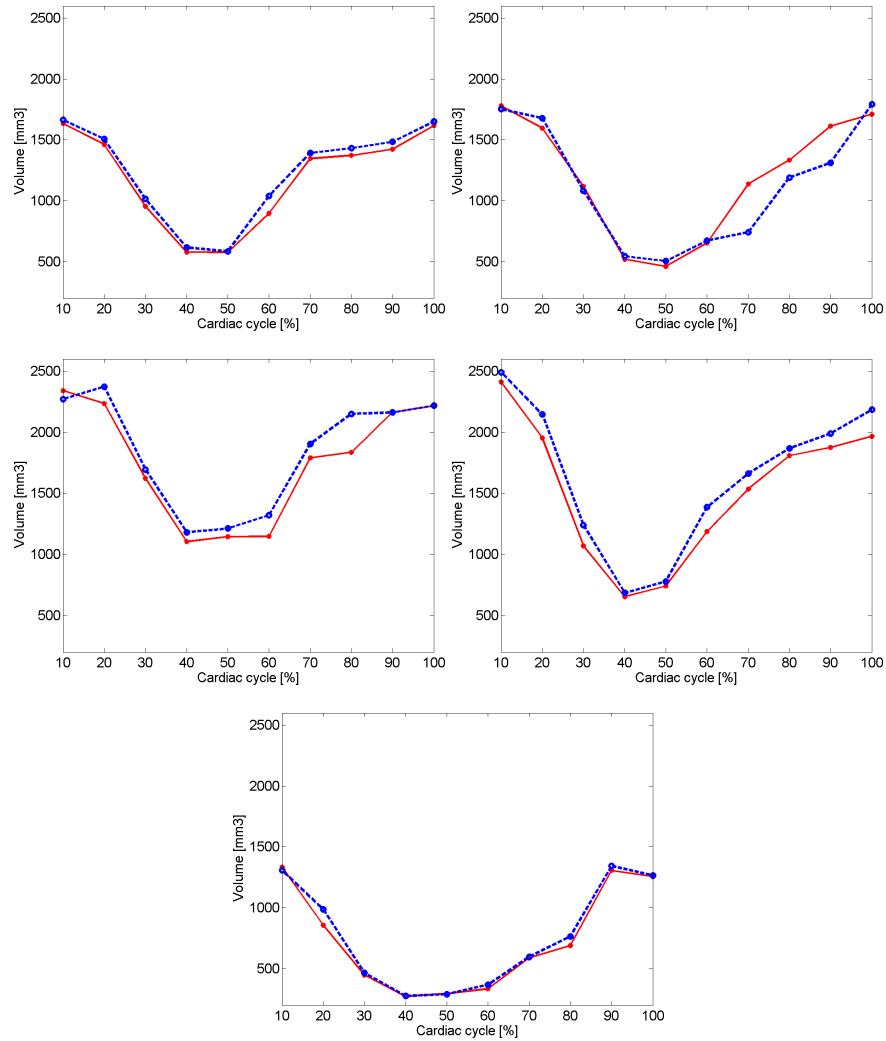


Figure 5.5: Left ventricle volume comparison against manual contour (blue). Each column belongs to a different patient. The method (red) is: GRAY.

5.1 Texture descriptor approaches to level set segmentation in medical images

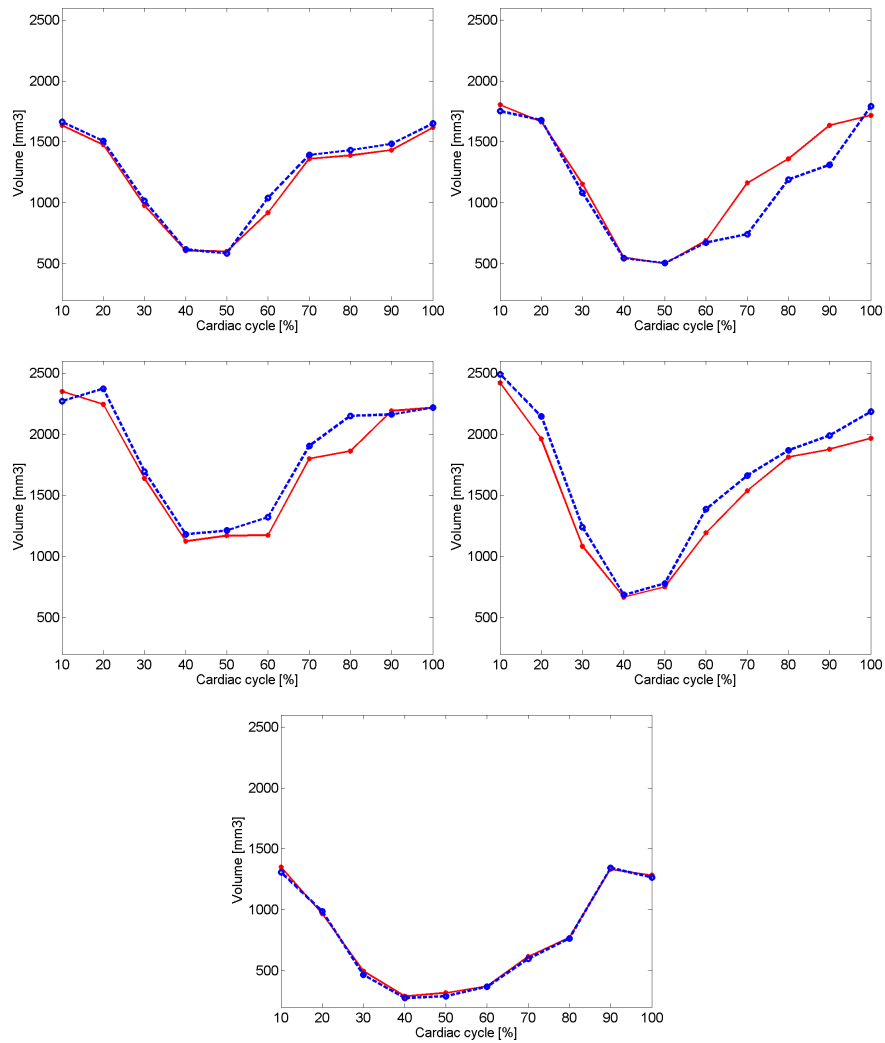


Figure 5.6: Left ventricle volume comparison against manual contour (blue). Each column belongs to a different patient. The method (red) is: Hermite3 + GRAY.

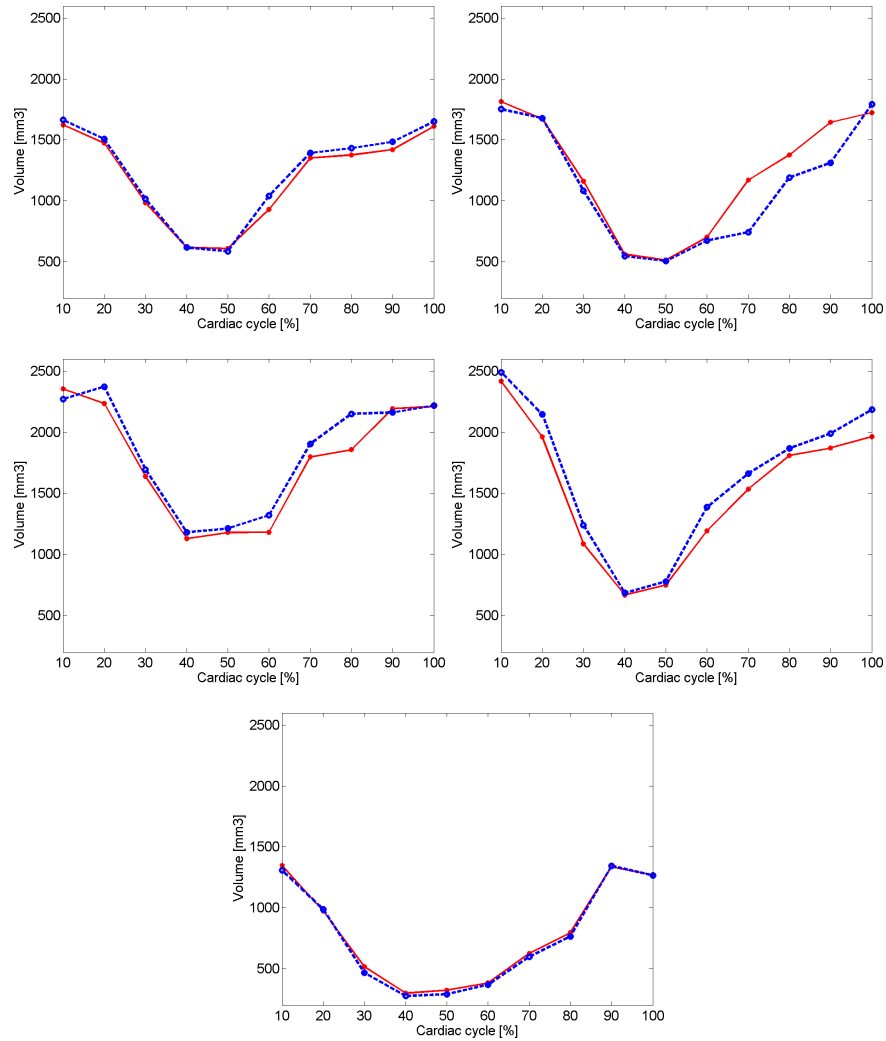


Figure 5.7: Left ventricle volume comparison against manual contour (blue). Each column belongs to a different patient. The method (red) is: Hermite5 + GRAY .

5.1 Texture descriptor approaches to level set segmentation in medical images

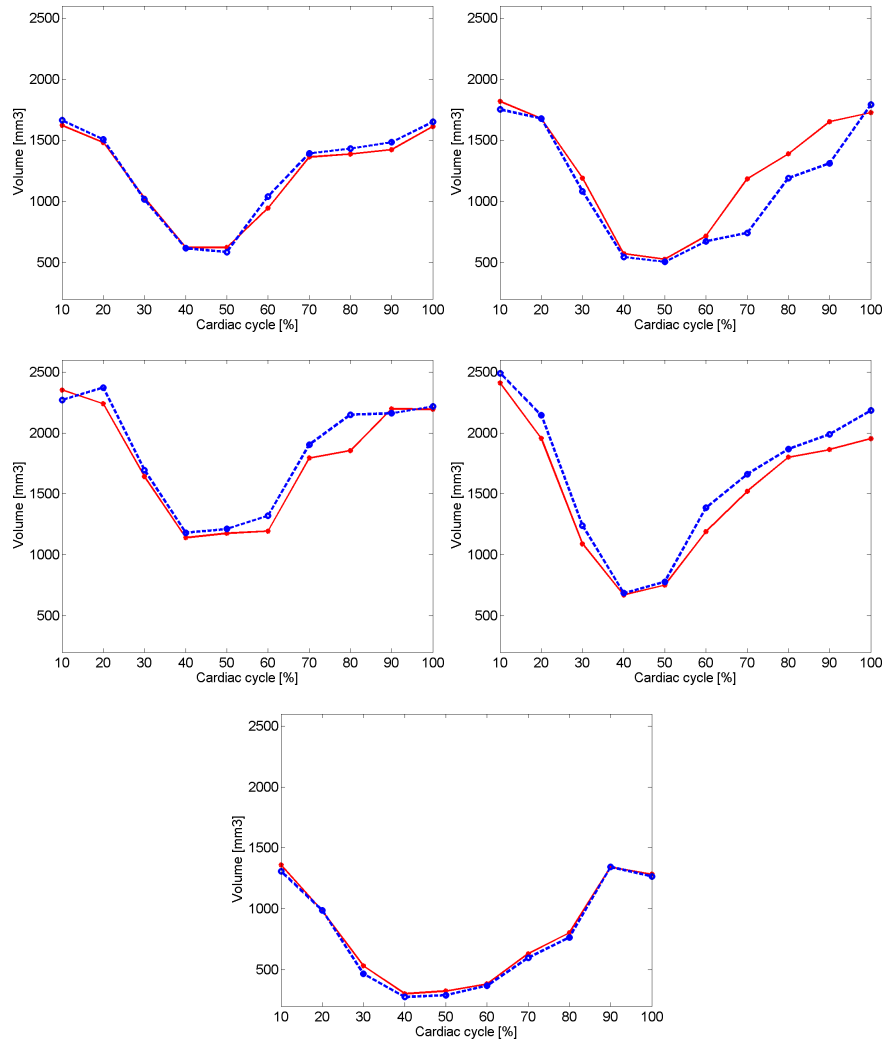


Figure 5.8: Left ventricle volume comparison against manual contour (blue). Each column belongs to a different patient. The method (red) is: Hermite9 + gray .

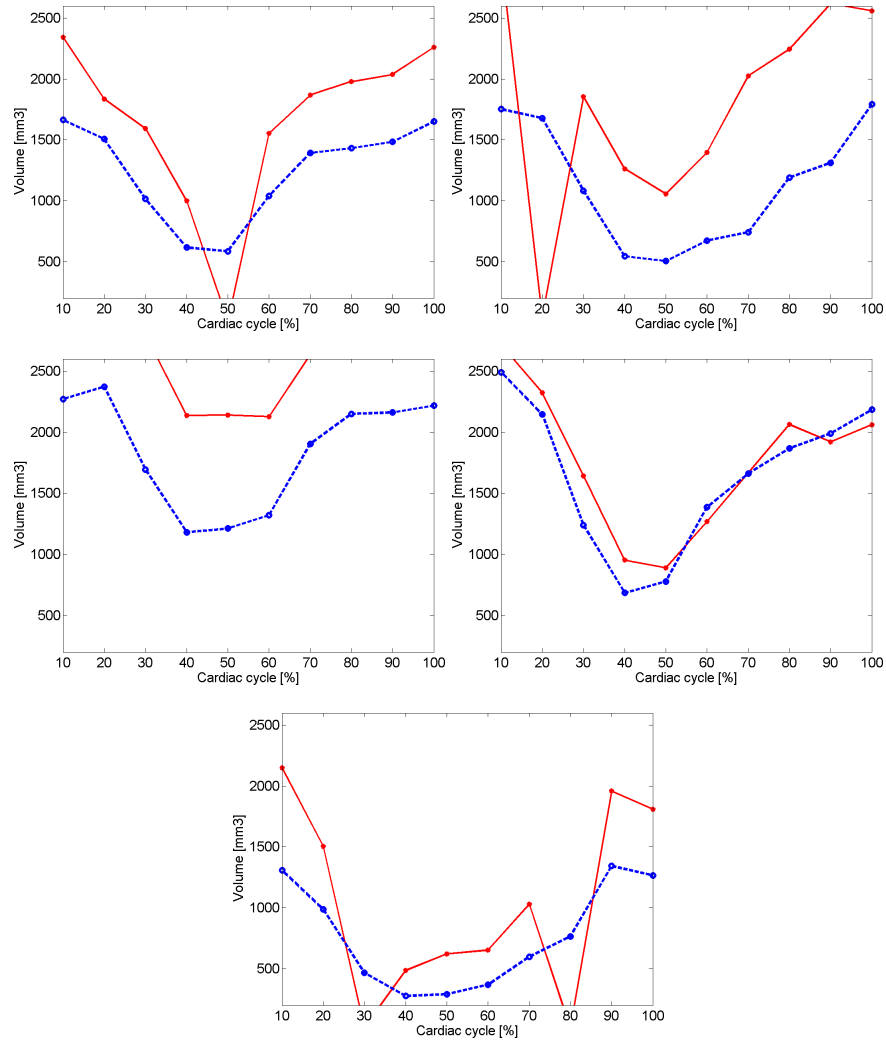


Figure 5.9: Left ventricle volume comparison against manual contour (blue). Each column belongs to a different patient. The method (red) is: LBP + GRAY.

5.1 Texture descriptor approaches to level set segmentation in medical images

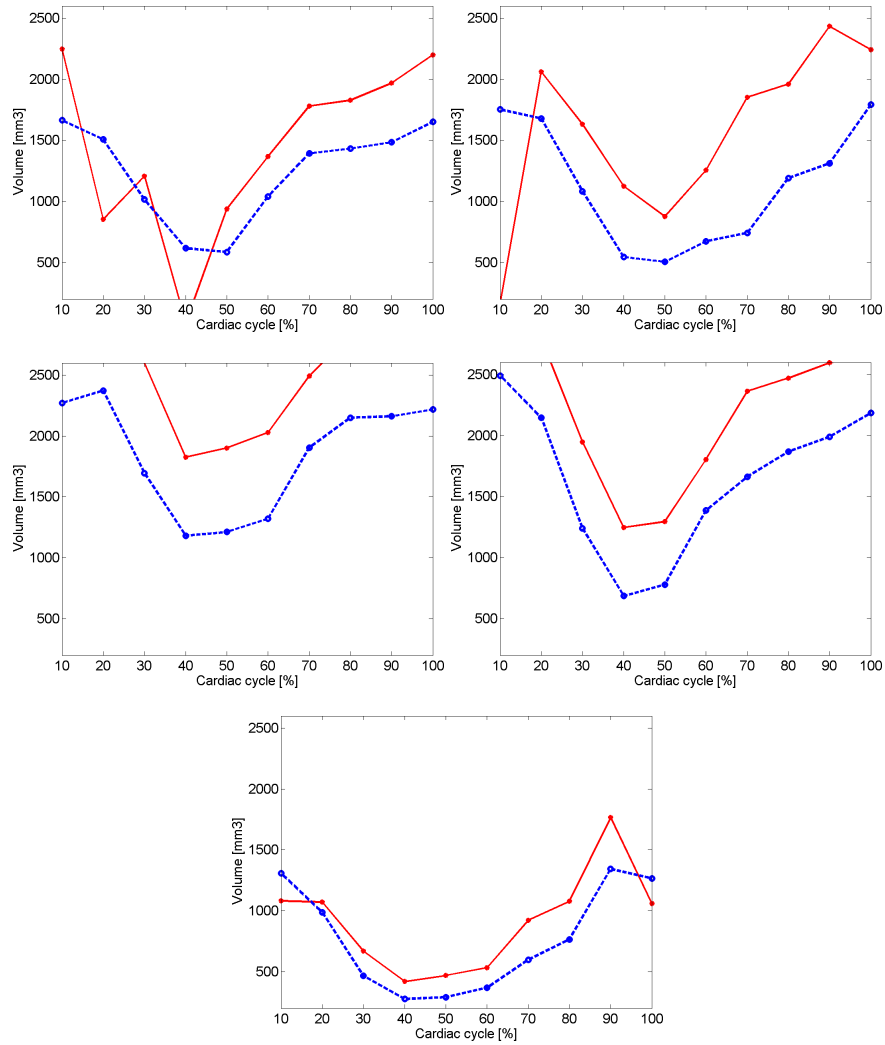


Figure 5.10: Left ventricle volume comparison against manual contour (blue). Each column belongs to a different patient. The method (red) is: LBPUM + GRAY .

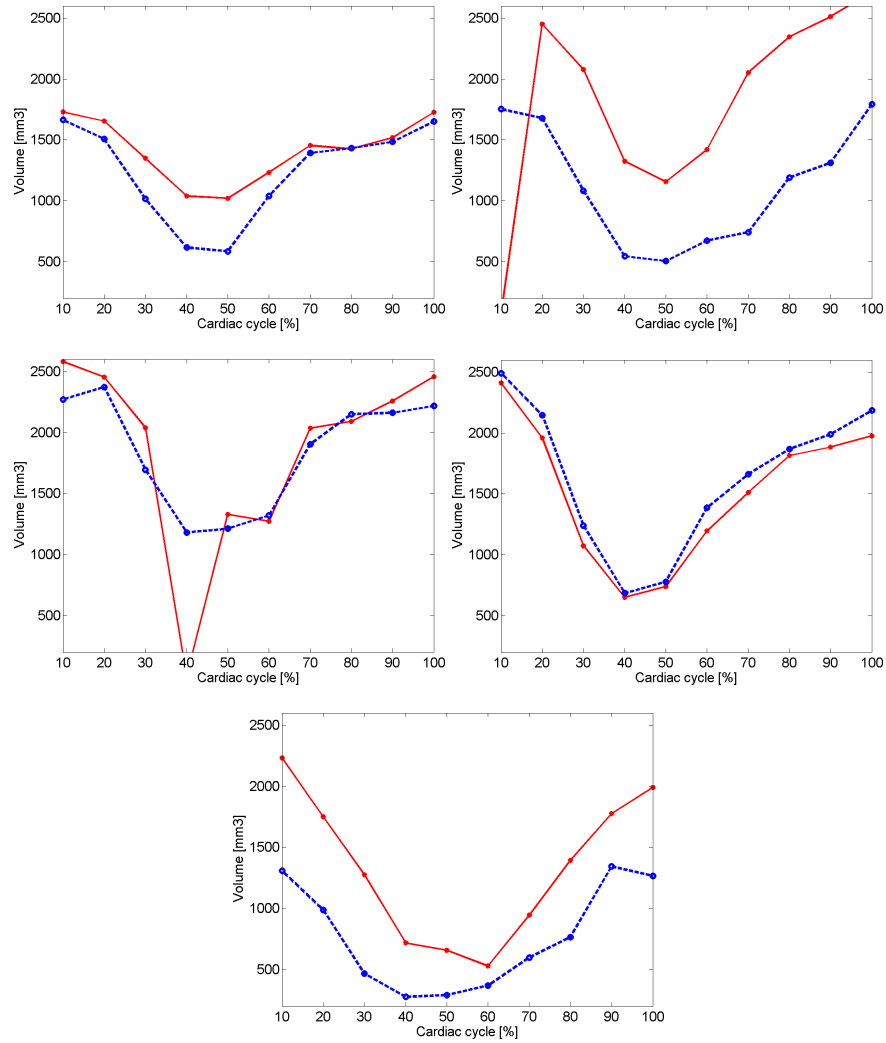


Figure 5.11: Left ventricle volume comparison against manual contour (blue). Each column belongs to a different patient. The method (red) is: BRINT + GRAY.

5.1 Texture descriptor approaches to level set segmentation in medical images

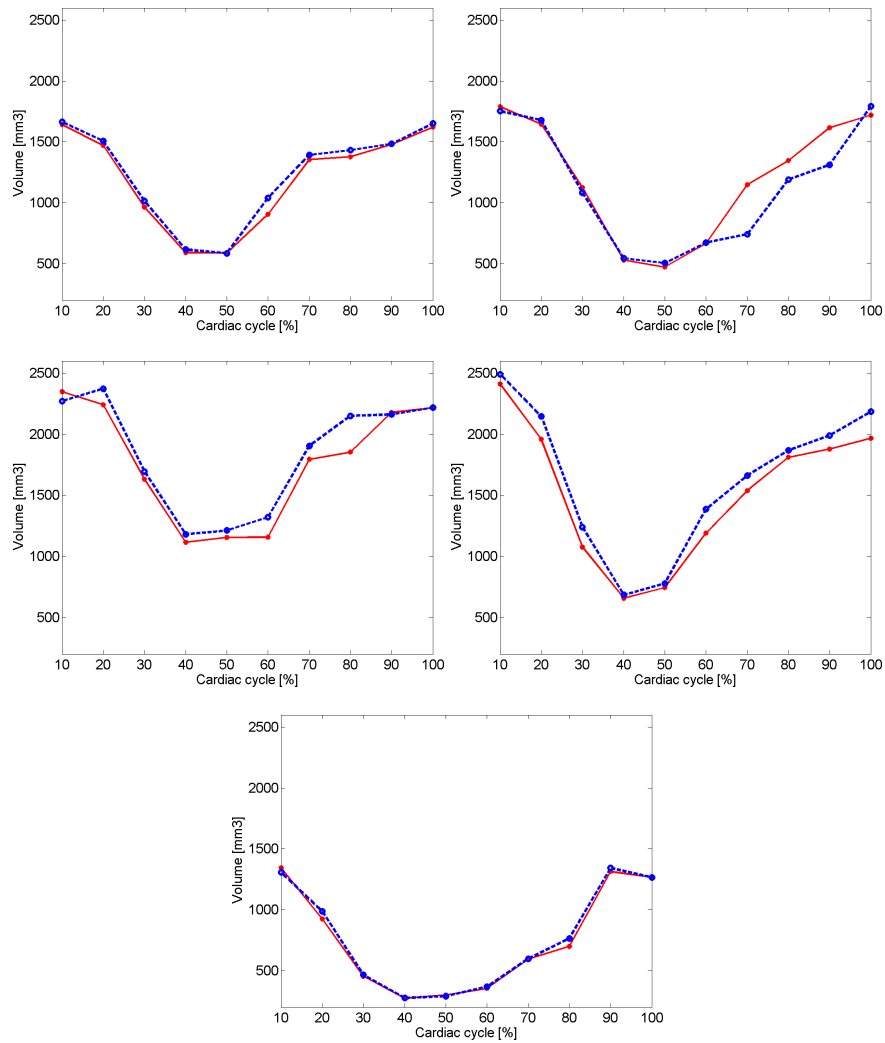


Figure 5.12: Left ventricle volume comparison against manual contour (blue). Each column belongs to a different patient. The method (red) is: Image derivatives + GRAY.

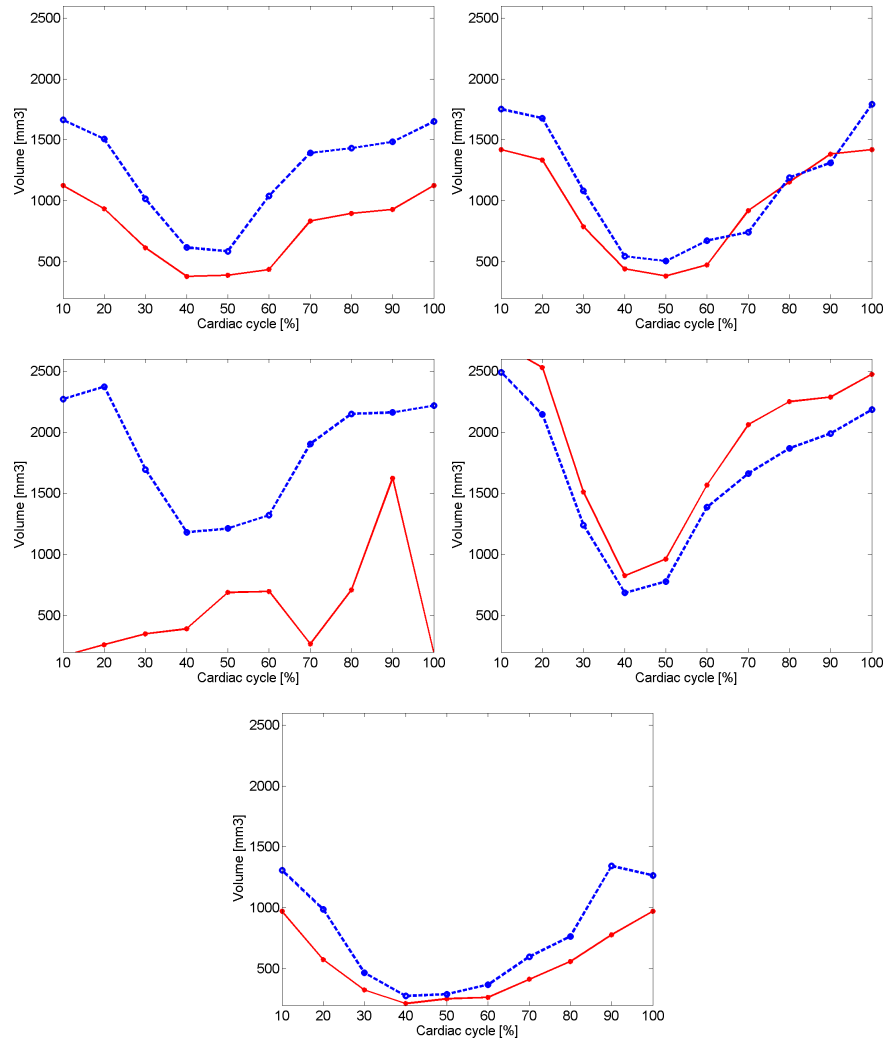


Figure 5.13: Left ventricle volume comparison against manual contour (blue). Each column belongs to a different patient. The method (red) is: Hounsfield values + GRAY.

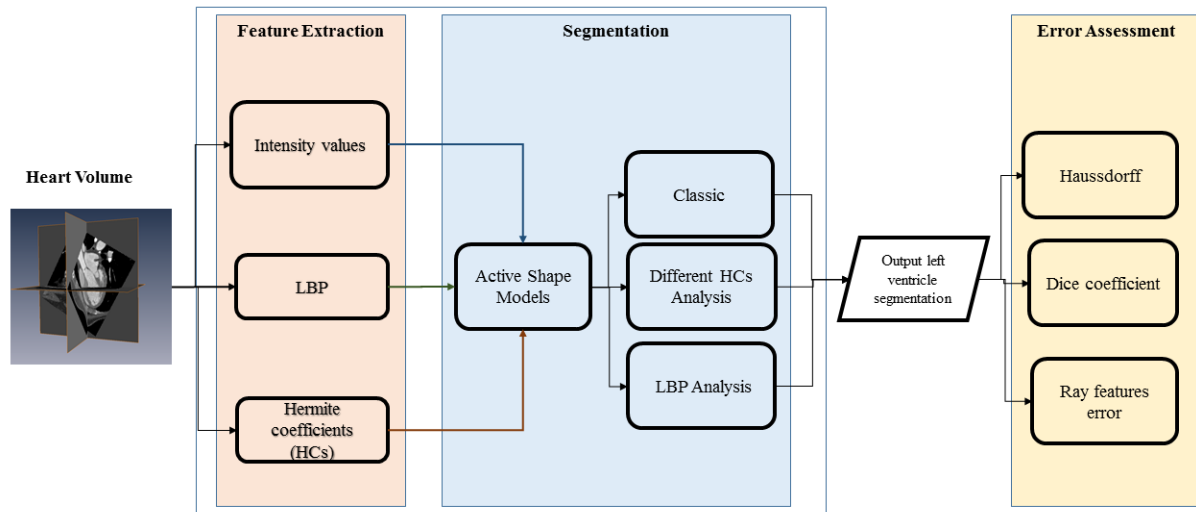


Figure 5.14: Overview of the experiments conducted in this study. First, feature extraction is performed and then incorporated into ASMs method to improve segmentation of cardiac walls. The assessment is conducted with three metrics: Hausdorff, Dice, and, Ray Feature error.

5.2 Contour-based Hermite segmentation of heart's left ventricle

The goal of this study is to identify endocardial and epicardial walls that contain myocardium with better precision. In the dataset, the endocardium possesses good contrast, while the epicardium is not always well-defined. Several attempts to segment such structures have been made, such as the ones mentioned in the previous section 5.1, but still better techniques are needed to improve results.

It is suggested taking advantage of the SHT to characterize important tissue structures and incorporate the information from the Hermite Coefficients (HCs) into the ASMs and LS schemes to improve the segmentation.

Two block diagrams resume the proposal in Figures 5.14 for ASM method and 5.15 for LS method.

The first step is to seed a suitable initialization for the ASM and LS algorithms. This is accomplished by estimating the position of the centroid of the LV blood pool during the diastole phase using a compactness metric similar to Lu et al. [61], (see Figure 5.16). This is a simple yet effective way to compute the initial pose. This step is performed on a slice from the mid-third or mid-cavity of the heart volume [3, 72]. A limitation of this step is that in the case of failure the LV cavity center must be manually specified.

5.2.1 COMBINING ACTIVE SHAPE MODELS WITH LBPs AND HCS

In [28], the authors proposed to combine ASMs and LBPs by considering only landmark profiles (see Figure 5.17(a)). Here, we extend the area of analysis and propose to combine ASMs with

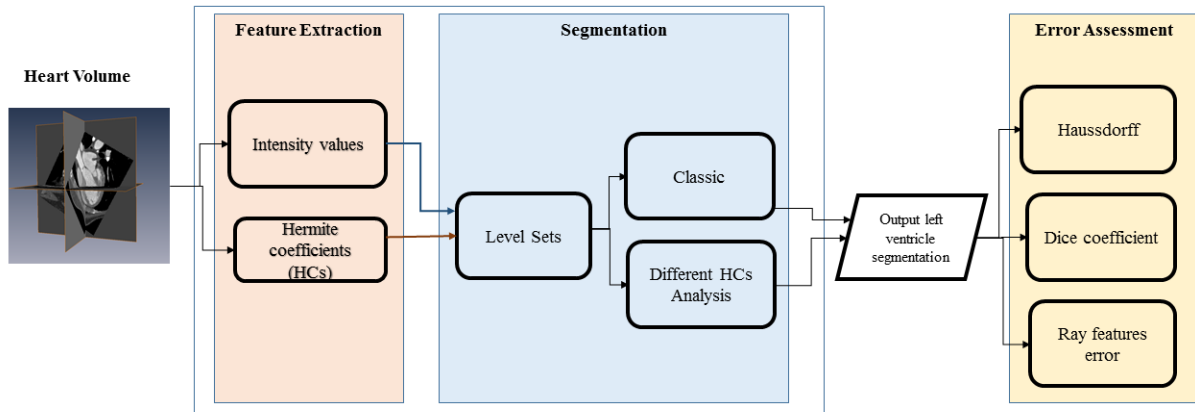


Figure 5.15: Overview of the experiments conducted in this study. First, feature extraction is performed and then incorporated into LS method to improve segmentation of cardiac walls. The assessment is conducted with three metrics: Hausdorff, Dice, and, Ray Feature error.

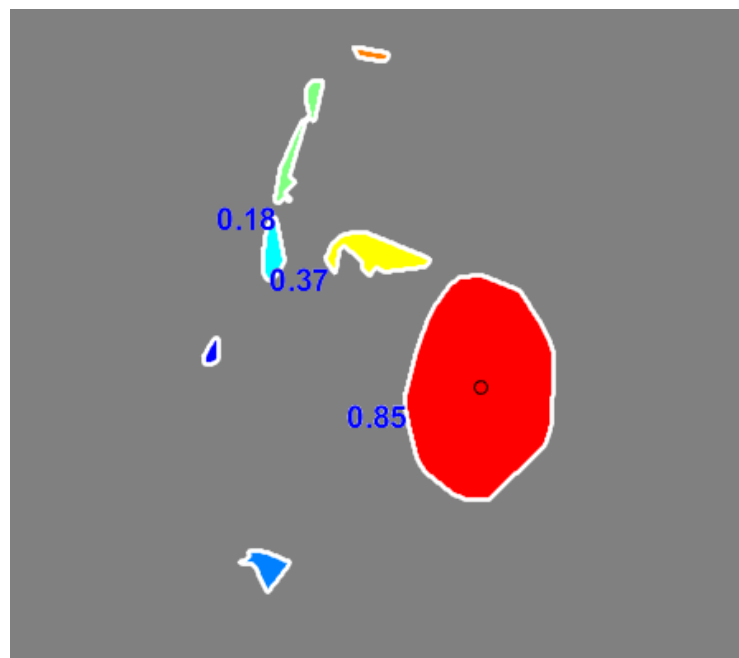


Figure 5.16: Metric of compactness. The blue numbers indicate the compactness value. A value of 1 means that the shape of the object is closer to a circle. During this step, the object with the largest compactness value is retained.

LBP, and ASMs with HCs to improve the segmentation of the IV. In addition, changes are made to the original ASM algorithm and four methods are explored: ASM-Quadratic with LBPs, ASM with HCs, ASM-Profile with HCs and ASM-Quadratic with HCs.

For all the cases, the initial parameters are set to: number of landmarks = 70, normal profile length = 11, and iterations = 60. These values were chosen based on the results of the experiments. Different combinations were evaluated like the number of landmarks, profile length, and number of iterations. In the case of the level sets approach 60 iterations are used, based on the reported performance for each error index.

ASM/QUADRATIC-LBP (ASM/LBP)

This is the method used in the midbrain segmentation chapter. As previously described, during the training phase, the LBPs are calculated over four square regions of 5×5 pixels around every landmark based on the approach presented in [28]. Then, a histogram that describes the corresponding landmark is constructed by concatenating the four local histograms (see Figure 5.17(b)). LBP is a simple but powerful method to characterize textures. Despite the fact there are quite a few versions [73], the original LBP is used due to its good performance and simplicity.

The histograms obtained during the recognition phase are compared against the trained histograms of the corresponding landmarks, so that, the closest point to the boundary is the one with the smallest histogram distance. We used the Chi-square distance. This distance can be used as a measure of dissimilarity between distributions, specifically between two histograms. It has also been used in applications such as texture and object classification and image retrieval [74]. A diagram with the description of the method is shown in Figure 5.17.

ASM/HCs

First, the steered HCs are computed with Eq. (3.7) and incorporated into the ASM in a multi-spectral fashion. Namely, every steered Hermite coefficient vector $\{L_k|k = 0, \dots, 3\}$ is considered a multi-spectral band. Thus, the multi-spectral values of the landmarks and profiles, g_i , are defined as follows:

$$g_i = \left[g_{pL_0}(x_p, y_p : L_0), g_{pL_1}(x_p, y_p : L_1), \dots, \right. \\ \left. g_{pL_2}(x_p, y_p : L_2), g_{pL_3}(x_p, y_p : L_3) \right] \quad (5.6)$$

where g_{pL_k} are the gray values at the position (x_p, y_p) that correspond to the profile p of the Hermite coefficients L_0, L_1, L_2 , and L_3 respectively, so each profile position has four numbers correspondent each coefficient. Here, the Mahalanobis distance calculates the closest point to each landmark.

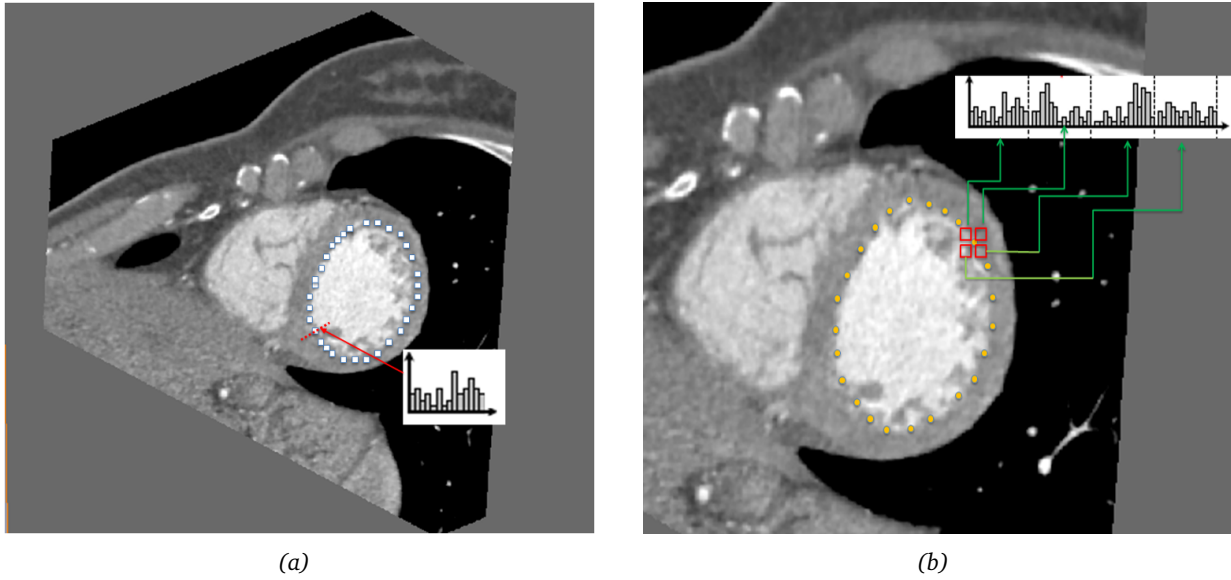


Figure 5.17: Two different techniques to combine ASMs and LBPs. (a) For every landmark, the LBP histograms are computed on all points of the corresponding profile of length n . (b) Quadratic-LBP histogram computes LBPs on four square regions of 5×5 pixels around each landmark, then a histogram is built by concatenating the four local histograms one after another.

ASM/PROFILE-HCs (ASM/PHCs)

Similar to ASM/LBP, for every landmark and its corresponding profile, the HCs are computed over a 9×9 pixel window (see Figure 5.18). The Hermite coefficients are computed only around the landmarks in order to speed up the process. The final histogram is created by concatenating the histograms of the HCs as follows:

$$p(r_{kL_n}) = \{n_{kL_0}, n_{kL_1}, n_{kL_2}, n_{kL_3}\} \quad (5.7)$$

where n_k represents a k -bin histogram of the Hermite coefficients L_0 , L_1 , L_2 , and L_3 that correspond to the profile p . r_{kL_n} is the final histogram of the L_n coefficients that is normalized by the size of the image M (rows) and N (cols). Finally, the landmark position is adjusted by computing the smallest distance between the training landmark histogram and the profile's histograms of the new image according to the Chi-squared function.

ASM/QUADRATIC-HCs (ASM/QHCs)

This proposal computes HCs over four square regions defined by a 7×7 pixel window around the landmarks. This is similar to the quadratic region used in ASM/LBP (see Figure 5.19) but here the

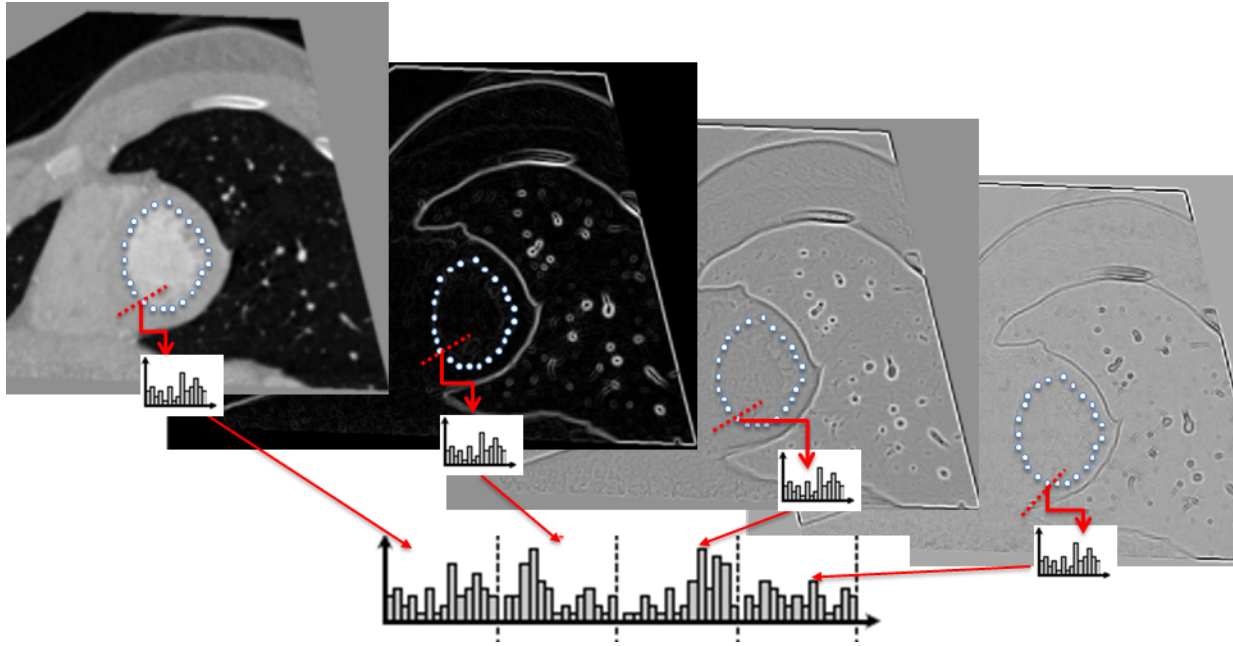


Figure 5.18: ASM/Profile-HCs scheme. The diagram shows the construction of the histograms for each landmark. For a given point in a profile, the four histograms of the corresponding Hermite coefficients are concatenated.

information from the HCs L_0 , L_1 , L_2 , and L_3 is included.

$$p(r_{QkL_n}) = \{n_{QkL_0}, n_{QkL_1}, n_{QkL_2}, n_{QkL_3}\} \quad (5.8)$$

where Q stands for quadratic region.

5.2.2 COMBINING FAST LEVEL SETS WITH HCS

Level sets are an efficient method for segmenting organ tissue when the borders possess good contrast (e. g. endocardium). However, the main bottleneck is the computation time. Thus, fast level sets in combination with the Hermite coefficients are used. After testing several iteration values, also the behavior of the number of iterations against the error indexes in order to obtain the best value were reviewed. The final value for the number of iterations is 60.

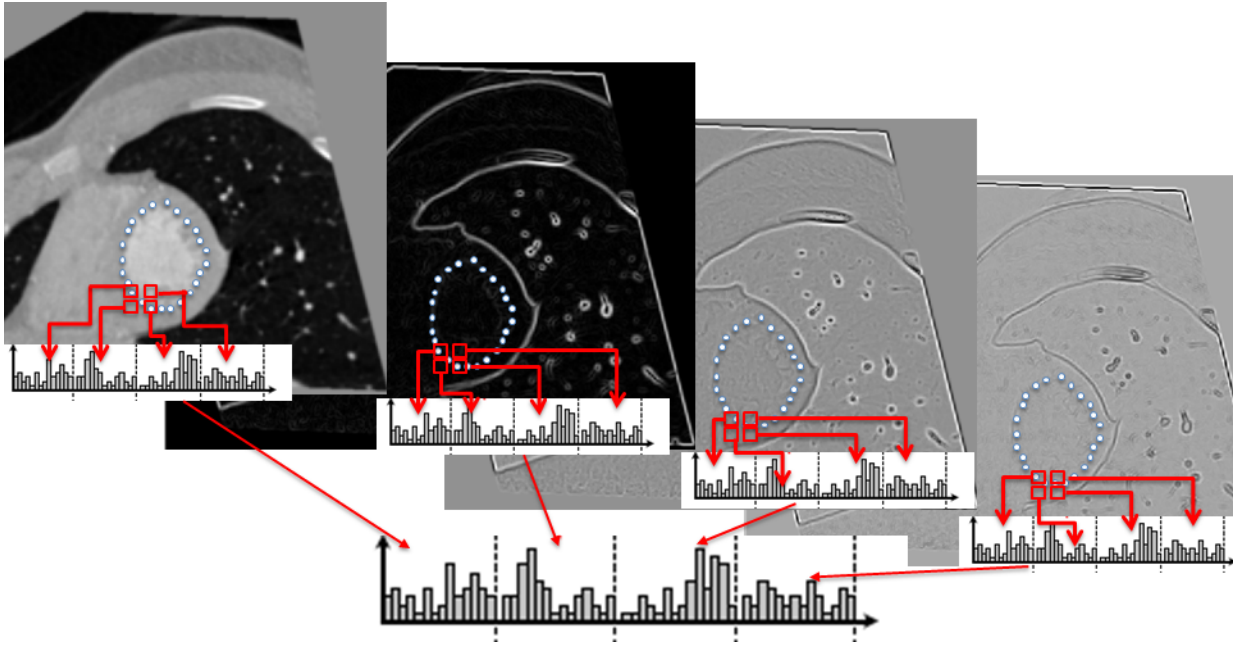


Figure 5.19: ASM/Quadratic-HCs scheme. The diagram shows the construction of the histogram. For a given point, four regions around a landmark are computed. This procedure is performed on every Hermite coefficient.

FLS/HCs

The steered Hermite coefficients are used as a simplified vector model from equation 2.9 that defines the initial velocity field as follows:

$$\begin{aligned}
 \phi^{n+1} = \phi^n - \Delta t \left[\delta_\epsilon \left[\mu \operatorname{div} \left(\frac{\nabla \phi}{|\nabla \phi|} \right) - \frac{1}{4} \left\{ \lambda_0^+ (L_0 - c_0^+)^2 + \lambda_1^+ (L_1 - c_1^+)^2 \right. \right. \right. \\
 \left. \left. \left. + \lambda_2^+ (L_2 - c_2^+)^2 + \lambda_3^+ (L_3 - c_3^+)^2 \right\} \right. \right. \\
 \left. \left. + \frac{1}{4} \left\{ \lambda_0^- (L_0 - c_0^-)^2 + \lambda_1^- (L_1 - c_1^-)^2 \right. \right. \right. \\
 \left. \left. \left. + \lambda_2^- (L_2 - c_2^-)^2 + \lambda_3^- (L_3 - c_3^-)^2 \right\} \right] \right]
 \end{aligned} \tag{5.9}$$

where L_x are the HCs, c_x^- and c_x^+ are the average values inside and outside the curve respectively.

And recalling the simplification of the algorithm, it is defined as:

$$v(x) = \begin{cases} 1 & \text{if } -\frac{1}{4}\left\{\lambda_0^+(L_0 - c_0^+)^2 + \lambda_1^+(L_1 - c_1^+)^2\right. \\ & \left. + \lambda_2^+(L_2 - c_2^+)^2 + \lambda_3^+(L_3 - c_3^+)^2\right\} \\ & + \frac{1}{4}\left\{\lambda_0^-(L_0 - c_0^-)^2 + \lambda_1^-(L_1 - c_1^-)^2\right. \\ & \left. + \lambda_2^-(L_2 - c_2^-)^2 + \lambda_3^-(L_3 - c_3^-)^2\right\} + \frac{1}{K} \sum_{i=1}^K \lambda_i^-(I_i(\bar{x}) - c_i^-)^2 \geq 0 \\ -1 & \text{if } -\frac{1}{4}\left\{\lambda_0^+(L_0 - c_0^+)^2 + \lambda_1^+(L_1 - c_1^+)^2\right. \\ & \left. + \lambda_2^+(L_2 - c_2^+)^2 + \lambda_3^+(L_3 - c_3^+)^2\right\} \\ & + \frac{1}{4}\left\{\lambda_0^-(L_0 - c_0^-)^2 + \lambda_1^-(L_1 - c_1^-)^2\right. \\ & \left. + \lambda_2^-(L_2 - c_2^-)^2 + \lambda_3^-(L_3 - c_3^-)^2\right\} \leq 0 \end{cases} \quad (5.10)$$

5.2.3 MATERIALS

A dataset of 28 annotated tomographic cardiac studies was acquired from healthy subjects with a CT Siemens dual source scanner (128 channels) at Hospital Ángeles Pedregal México. The heart volumes were captured in signed 12-bits DICOM format. The age of subjects range from 17 to 81 with an average age of 55. 16 studies belong to males and 12 studies belong to females. All patients present low risk for coronary artery disease and atypical chest pain.

Each study belongs to a single subject and consists of 10 volumes taken at different times during the electrocardiography (ECG)-synchronized cardiac cycle. This method is called ECG-gating, where a volume is acquired only during certain consecutive period of the cardiac cycle being retrospectively reconstructed. It covers systolic and diastolic cardiac phases.

The studies start on a final diastolic (relaxing) phase, go throughout the systolic (contraction) phase and return to the diastolic phase, providing images at 0%, 10%, 20%, 30%, 40%, 50%, 60%, 70%, 80% and 90% of the cardiac cycle. The spatial resolution values range from $0.302734 \times 0.302735 \times 1.5$ [mm] to $0.433593 \times 0.433593 \times 1$ [mm].

Since the volumes are oriented on different angles, a manual alignment with the short axis view was performed. This step was reviewed by experienced physicians. Furthermore, due to the fact that modern CT scanners have a wide range of Hounsfield units (HU), the volumes were mapped into a more suitable range from -1024 HU to 2200 HU. Then, a normalization step was applied to avoid negative values.

5.2.4 EXPERIMENTAL RESULTS

The aforementioned algorithms were validated against manual annotations made by an expert physician and one assistant in 28 studies throughout the entire cardiac cycle from healthy subjects.

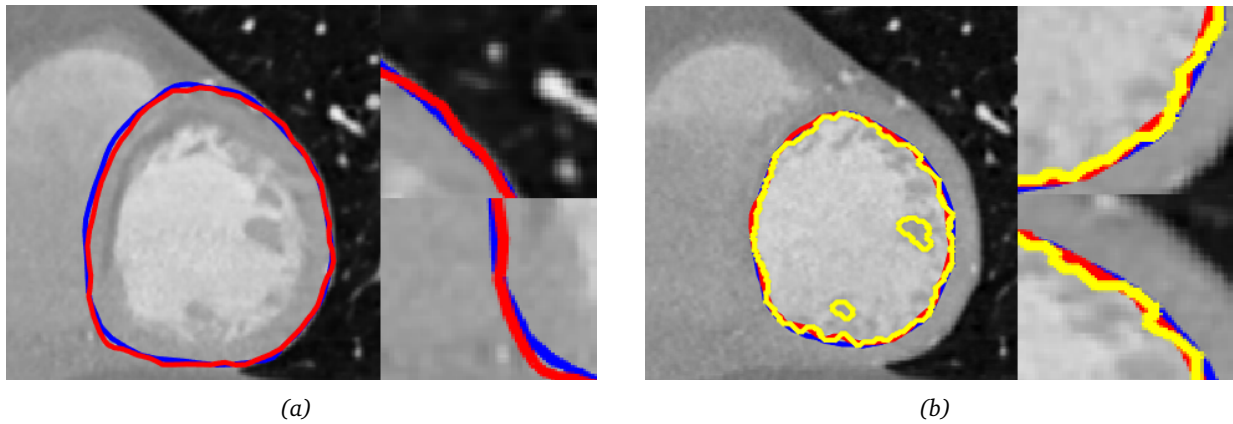


Figure 5.20: Segmentation details. Ground-truth boundary (red), experimental segmentation (blue). The best segmentation cases for (a) ASM/QHCs on the epicardium and (b) FLS/HCs on the endocardium. Papillary muscles are delineated on yellow.

Middle slices of the volumes are used, so that every study is composed of ten images that cover diastole and systole phases. It is also identified each slice with the percentage of the cardiac cycle [0%, 10%, 20%, ..., 90%]. A total of 280 different images were tested on a 2D slice-by-slice scheme. For the proposed initialization, good results were obtained on 22 of the 28 slices. The evaluation started with images at 0% cardiac cycle per subject. The same initialization was used throughout the cycle.

In order to reduce bias, four-fold cross-validation is used to train the ASM. Every fold was chosen randomly. Our experiments were divided into two groups: endocardium (Section 5.2.4) and epicardium segmentation (Section 5.2.4).

The experiments with FLS include an expansion of the resulting contour that encloses the cavity segmentation. The procedure segments papillary muscles followed by a convex hull in order to generate a rounded envelope to enfold them. This step represents a refinement that allows the segmentation to resemble boundaries manually drawn by clinicians.

Regarding epicardium segmentation, an example using ASMs is shown in Figure 5.20(a). The experimental contour in blue is compared against the ground-truth boundary in red. With respect to the steered Hermite coefficient computation, different window sizes were evaluated. A window size of 9×9 pixels achieved better quantitative results in most of the cases, including the endocardium wall (see Figure 5.20(b) where papillary muscles are also segmented in yellow.)

For the Gaussian sigma values, we used different values on endocardium and epicardium given the differences of the zones to be segmented. They are shown on Table 5.3.

A quantitative analysis is performed using three metrics: Hausdorff distance (HD), Dice index (DI), and Ray Feature error (RFE). The latter is a novel metric for segmentation evaluation based on ray features [75]. It allows us to measure in a simple, robust way shape similarities between two overlapping objects. The method is introduced in Appendix. Examples of the best segmentations

5.2 Contour-based Hermite segmentation of heart's left ventricle

Table 5.3: *Sigma values for Active Contour methods.*

| Method | σ values | |
|-------------|-----------------|------|
| | ASMs | FLSs |
| endocardium | 5 | 9 |
| epicardium | 7 | 29 |

for endocardium and epicardium are shown in Figure 5.20.

In order to evaluate the segmentation performance of the different approaches presented, ANOVA analysis was run. The p -values are shown in Figures 5.22 and 5.23 for endocardium and pericardium respectively.

ENDOCARDIUM SEGMENTATION

In order to segment the endocardium, seven different schemes were computed. Two methods are based on fast level sets, FLS and FLS/HCs, and the rest of the methods are based on ASMs: ASM, ASM/HCs, ASM/PHCs, ASM/QHCs, and ASM/LBP. As expected, segmentation during systole is a more challenging task but it can be observed that in most cases the best results were achieved with FLS and FLS/HCs, while ASM/LBP presented the worst result.

Since the performance of the level set-based algorithms strongly depends on the number of iterations, a comparison of the best two cases and their behavior when the number of iterations changes were included (see Figure 5.21). Average results are summarized in Figure 5.22 using HD, DI, and RFE. Note that RFE shows clearer differences among algorithms and seems more consistent with DI than with HD.

EPICARDIUM SEGMENTATION

In order to segment epicardium, six approaches were computed: FLS/HCs, ASM, ASM/HCs, ASM/PHCs, ASM/QHCs, and ASM/LBP. In this section, FLS approach was not included because the algorithm did not converge due to the lack of contrast in the tissue that surrounds the epicardium.

In general, throughout the cardiac cycle the ASM-based methods show good results, especially those methods that include texture information like ASM/QHCs and in some percentages ASM/LBP, whereas ASM/HCs achieved the poorest results. It is important to observe that FLS/HCS also presents good performance. The average results are summarized in Figure 5.23. Also in this case, RFE is more consistent with DI than with HD. Consider for instance that HD changes the rank order of the best performing algorithms ASM, ASM/QHCs, and ASM/LBP throughout the cardiac cycle in comparison with DI and RFE.

Segmentation of the endocardium and the epicardium throughout the cardiac cycle is presented

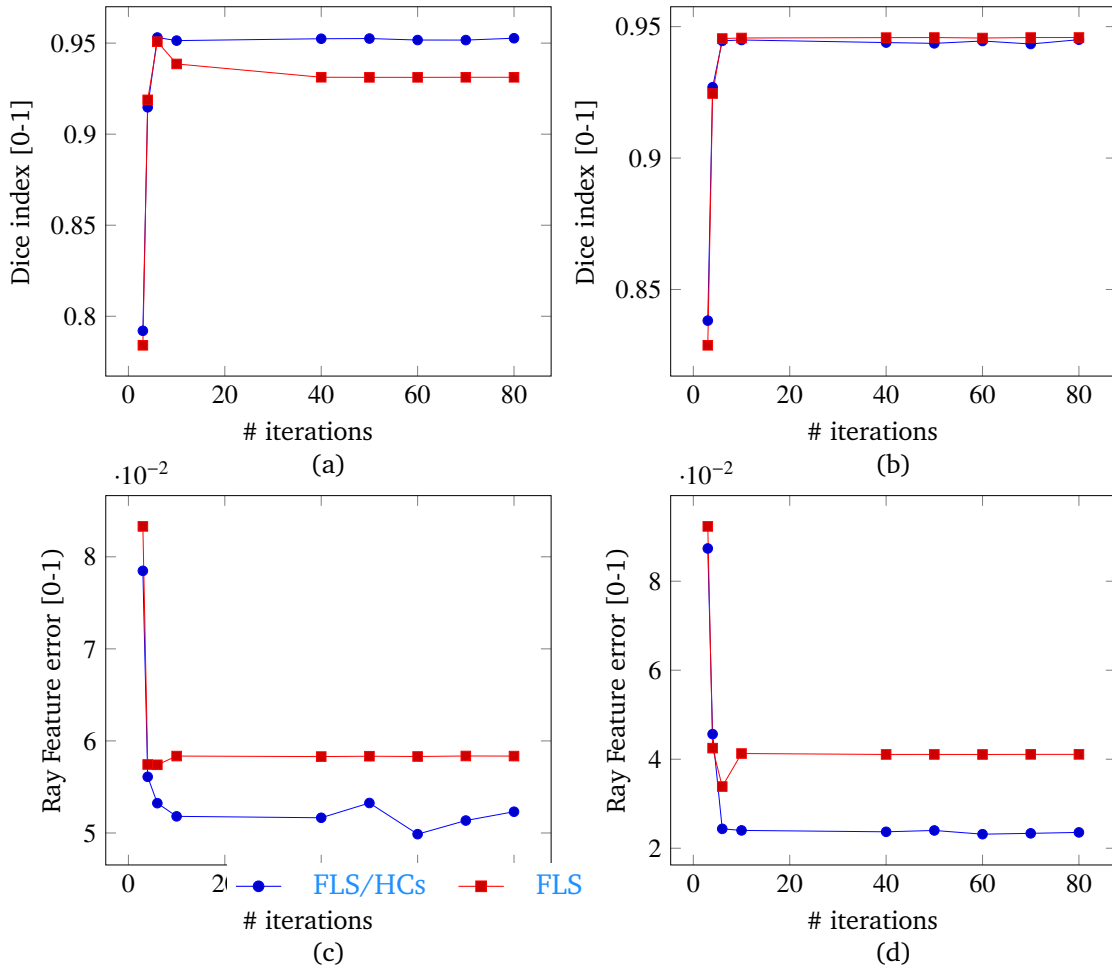


Figure 5.21: Plots depict the performance of FLS and FLS/HCs endocardium segmentation against the number of iterations measured with Dice index (upper row) and Ray Feature error (lower row). Dice index is between 0 and 1, values close to 1 indicate similar contours. Ray Feature error is between 0 and 1; values close to 0 indicate similar contours. The values were taken during (a) 0%, (b) 60%, (c) 20%, and (d) 90% of the cardiac cycle.

5.2 Contour-based Hermite segmentation of heart's left ventricle

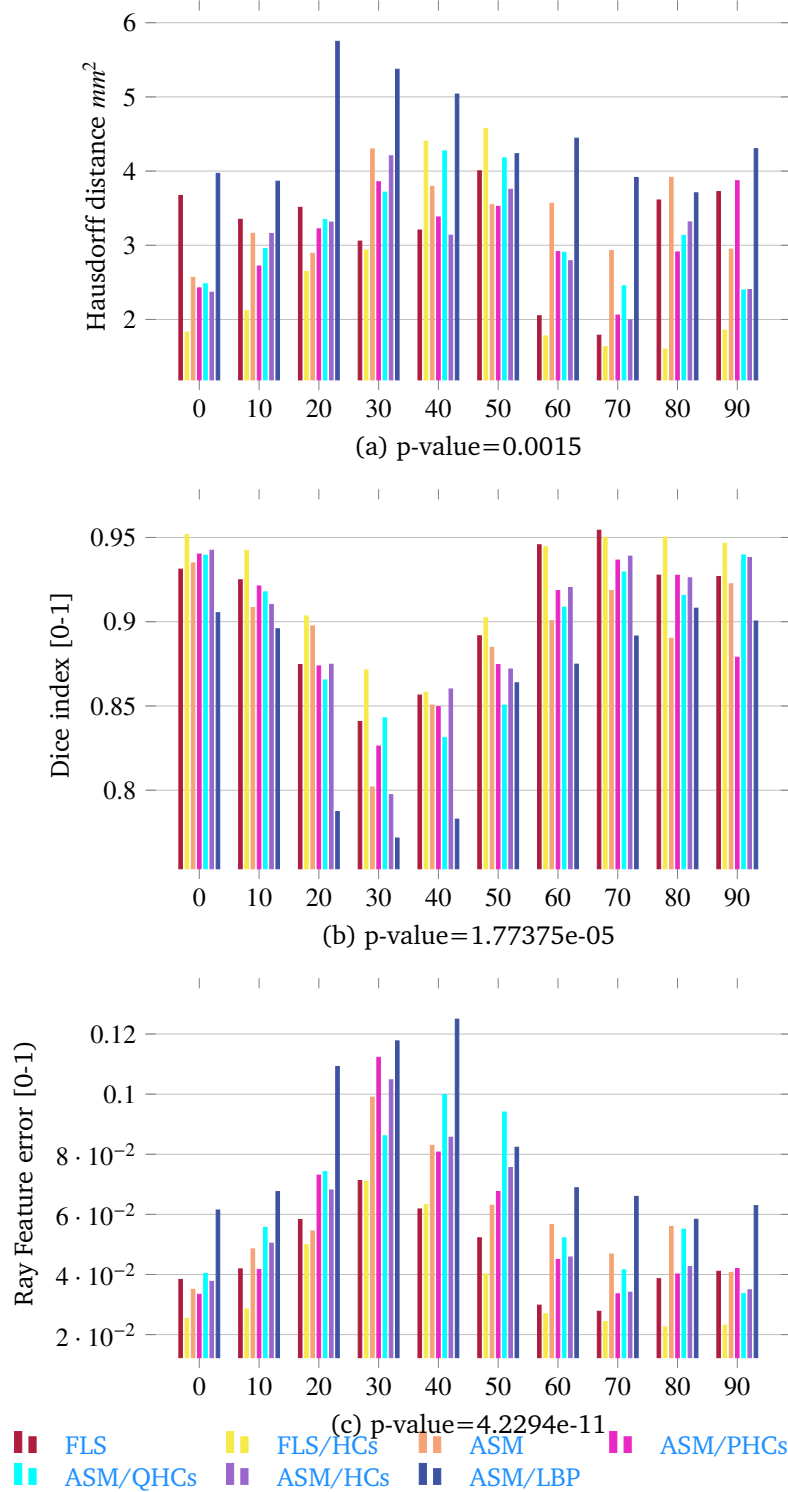


Figure 5.22: Average distances between the experimental and the expert contours with Hausdorff distance (lower values indicate more alike boundaries), Dice coefficient (values close to 1 indicate more similar contours) and Ray Feature error (values close to 0 indicate more similar contours) for endocardium segmentation. X-axis represents the percentages of the cardiac cycle (diastole-systole).

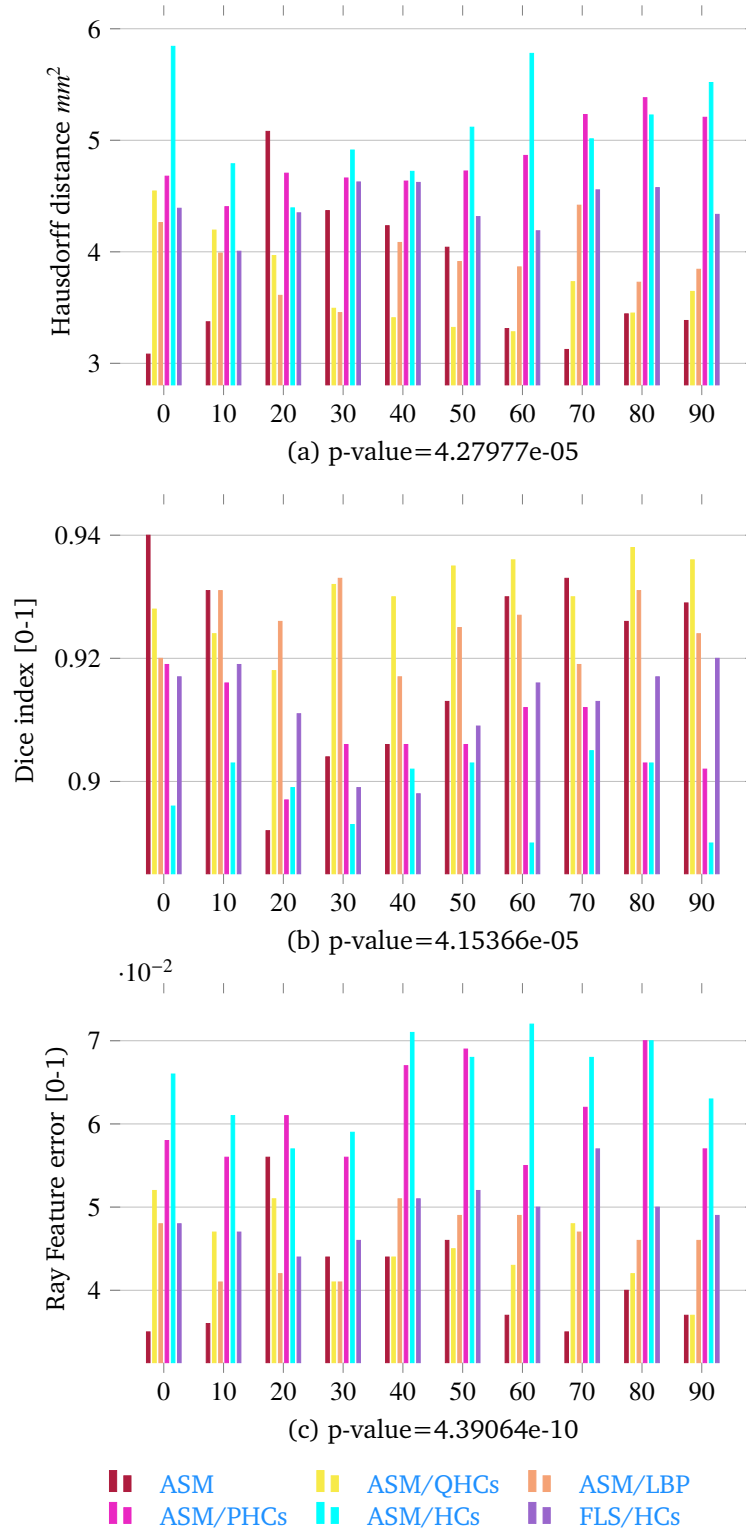


Figure 5.23: Average distances between the experimental and the expert contours with Hausdorff distance (lower values indicate more alike boundaries), Dice coefficient (values close to 1 indicate more similar contours) and Ray Feature error (values close to 0 indicate more similar contours) for epicardium segmentation. X-axis represents the percentages during the cardiac cycle (diastole-systole).

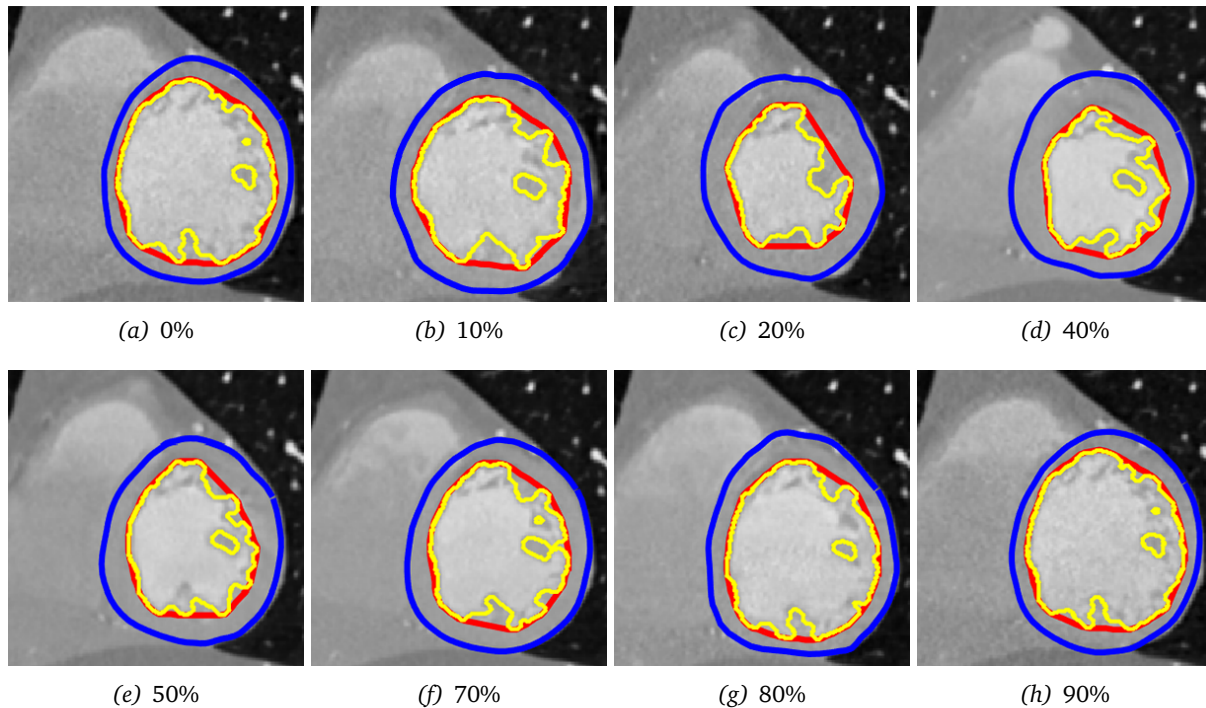


Figure 5.24: Final segmentations of endocardium (red) using FLS/HCs method, epicardium (blue) using ASM/QHC method, and papillary muscles (yellow) throughout the cardiac cycle.

in Figure 5.24 using FLS/HCs for endocardium and ASM/QHC for epicardium.

EVALUATION OF SEGMENTATION ON NOISY IMAGES

In order to assess how the addition of Hermite coefficients adds robustness to the segmentation, the approaches FLS and FLS/HCs were evaluated in the endocardium segmentation by adding Gaussian noise with zero mean and incrementing the variance gradually. Comparison results are shown in Figure 5.25. Notice that FLS/HCs shows a better performance in comparison with FLS.

5.2.5 DISCUSSION

From the results (see Figure 5.21 and Figure 5.22), fast level sets in combination with HCs was considered as the first option when the endocardium is segmented. The reason is that the information provided by HCs improves the convergence and velocity of our method. The results remain consistent when comparing the three metrics: Dice, Hausdorff, and Ray Feature error.

The image expansion computed with the steered Hermite transform permits the extraction of features based on Gaussian derivatives that highlight salient visual cues. The SHT enhances segmentation because it adapts to local orientation content. The window of analysis used to compute the steered Hermite coefficients was set to 9×9 . Also different sizes were evaluated: 5×5 , 7×7 , and 11×11 with not as good results as the ones of the 9×9 , it gets a better segmentation

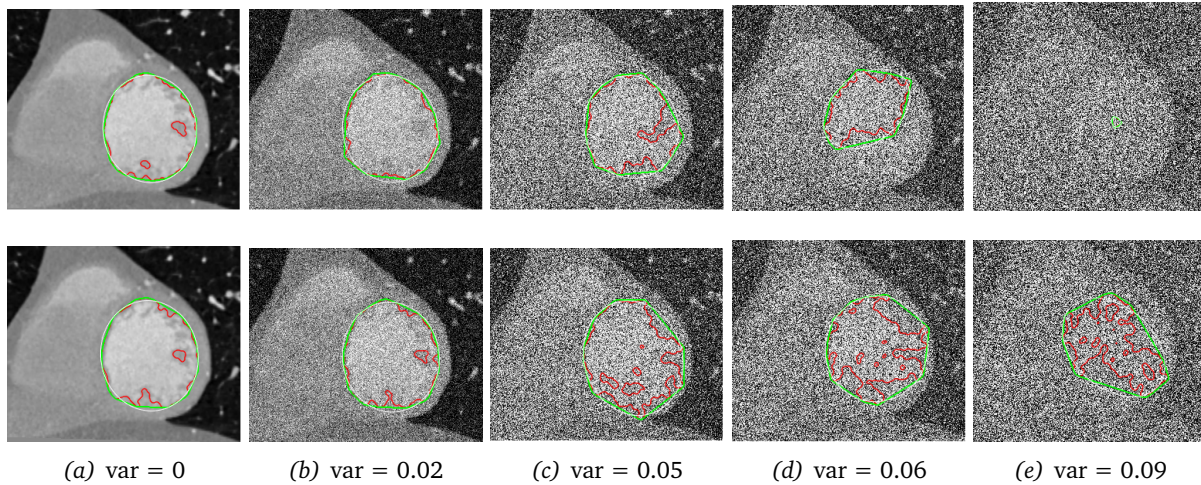


Figure 5.25: Comparison of segmentation results between FLS (upper row) and FLS/HCs (lower row) on the endocardium (red contour) adding Gaussian noise with zero mean and increasing variances (var).

result on most of the data. However, the window size of analysis used in SHT is not related to the window used with LBPs because the approaches belong to a different analysis. The LBPs window size was previously evaluated in [28] where multiple variations of LBPs were studied. According to the results, the method ASM/QHCs outperforms ASM/LBP.

In the case of epicardium segmentation the lack of tissue contrast that surrounds the epicardium hampered the segmentation with FLS. Nevertheless, the joint model FLS/HCs converged in spite of the poor border definition. The combination of HCs and ASMs also enhanced the segmentation performance on the epicardium. Consequently, the limitation of the shape restriction inherent to the method was overcome. It is important to mention that with other variations of ASMs, as in the case of adding Hermite coefficients and LBP information, the segmentation improved. When using approaches based on local features such as ASM/QHCs and ASM/LBP, the final results also achieved better segmentations, which suggests that including both local and global information may lead to better results.

From the endocardium results (see Figure 5.22), it is possible to infer that the segmentation performance of all the methods varies along the cardiac cycle, with systole being the most difficult phase to segment. However, the algorithm rank performance remains with no changes. On the other hand, when attempting to segment the epicardium, contrast differences are low. This implies that in addition to the borders, texture information must be taken into account. The Hermite coefficients obtained from Gaussian derivative operators include relevant texture information and can therefore improve segmentation.

When ASM/QHCs was used for segmenting the epicardium, (see Figure 5.23), the results obtained were consistent with good scores. ASM/LBP ranks in the first places in some of the initial percentages cycle: around 20% and 30%. Note how ASM decreases its performance in systole

5.2 Contour-based Hermite segmentation of heart's left ventricle

reaching third and fourth places in the subsequent phases compared to the initial percentages 0% and 10% of the cardiac cycle. FLS/HCs also has a satisfactory performance considering that FLS did not converge on epicardium segmentation. The best results were achieved with ASM, ASM/QHCs, ASM/LBP, and FLS/HCs. Two of these methods include information from the HCs. No previous training is required regarding FLSs-based approaches, so they have a substantial advantage over the other methods especially in time and computational work.

6

A perspective on the study of Heart failure

According to the World Health Organization, cardiovascular diseases rank number one as cause of death worldwide and were responsible for 31% of all deaths in 2012 [76]. Regarding heart failure, it is a serious condition although it does not necessarily mean cardiac arrest. Tobacco, unhealthy diet, and obesity represent major risk factors for heart failure [77]. About 5.7 million adults in the United States have suffered from heart failure and about half of the people who develop heart failure die within 5 years of diagnosis [78]. Every year, approximately 500,000 new heart failure cases are diagnosed; this represents an estimated cost of \$30.7 billion in health care [79].

In the case of left ventricular systolic dysfunction, the most pressing consideration is to determine if coronary artery disease, valvular disease, or any other etiology is responsible [80]. Whenever heart failure occurs, the heart shows reduced function. This may cause the left ventricle (LV) to lose its ability to contract or relax normally. In response, LV compensates for this stress by modifying its behavior, which creates hypertrophy that causes enlargement and hardening of the LV muscles and progresses to congestive heart failure [81].

Non-invasive imaging evaluations and clinical controls increase the probability of the survival of patients. They are also very important in the initial assessment of patients with new-onset heart failure [82]. Information about the current condition of the anatomical structures of the heart is needed for an early and accurate diagnosis. In the case of suspected heart failure, the most common image modality is the ultrasound-echocardiography due to its low cost and good spatial resolution. However, the reproducibility of quantitative measurements is user dependent and can be variable [80]. Magnetic resonance imaging (MRI) has also been used as a reference method [1].

It is useful for scanning and detecting abnormalities in soft organs and there is no involvement of any kind of radiation, yet it is expensive and presents limited availability compared with computed tomography (CT) [83].

In the case of heart failure along with coronary artery disease, CT imaging provides insights and detailed information of the heart that support and tailor treatments. Furthermore, heart examination using CT generates 2D and 3D high-resolution images throughout the entire cardiac cycle, which are useful for segmentation tasks. Although CT imaging does not provide suitable contrast resolution in comparison with MRI, it is more accessible and has enough spatial resolution to distinguish adjacent organs [58]. In addition, the use of contrast agents can improve endocardial border definition.

Cardiac segmentation is still a challenging task due to biological aspects that depend on the diverse organ anatomy and physical issues that image modalities must face. These include for example, noise due to unwanted movements, also from the respiratory system, cardiac synchronization, and differences in anatomy when a pathology occurs.

In order to create tools helpful for clinical decisions concerning diagnosis and treatment, the integration of visual information concerning different anatomical and dynamic characteristics of the left ventricle is a crucial task. This chapter intends to show a perspective with clinical applications of great relevance for the algorithms previously described, and trace some impressions of the tasks to be developed. We discuss in this chapter the following ones.

- Volume segmentation over the whole left ventricle.
- Motion estimation of segmented ventricle.

6.1 Volume segmentation over the whole left ventricle.

Chapter 5 exposed segmentation results validated with experimentation under optimal parameter settings.

In order to obtain a complete volume reconstruction and visualization from our segmentation results, it is necessary to segment the endocardium and epicardium on all the left ventricle' slices.

The best performing algorithm in this case was fast level sets with Hermite coefficients. Figure 6.1 displays the volume reconstruction obtained from the segmented ventricle slices.

In terms of accuracy and speed, this volume reconstruction may allow clinicians to measure important indices such as volume, mass, and ejection fraction.

6.2 Motion estimation of segmented ventricle

Because of the importance of understanding the left ventricle behavior, motion estimation is also a matter of study, and a way to obtain it is through the analysis of optical flow. Sequences of ordered

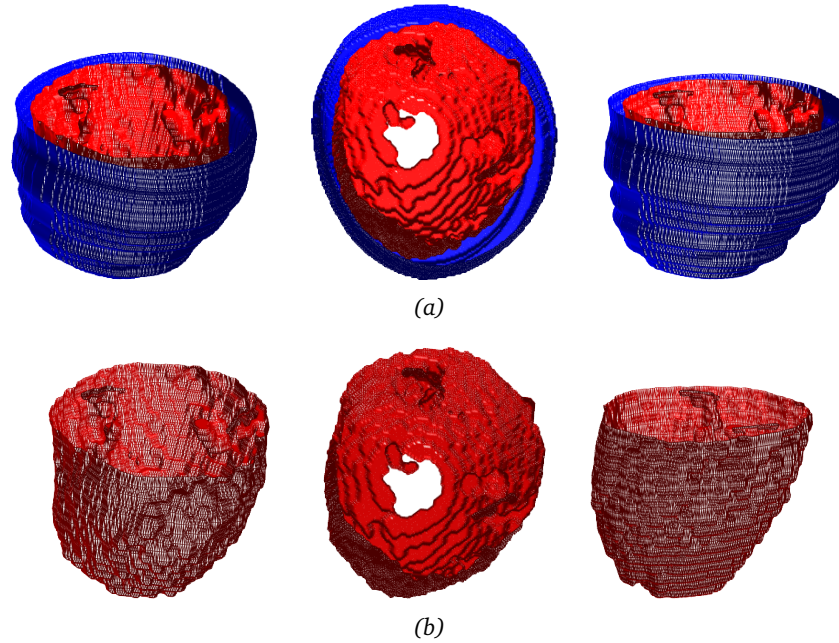


Figure 6.1: Volume segmentation of endocardium (red) and epicardium (blue) in (a) and only the endocardium in (b) using FLS/HCs.

images allow the estimation of motion as either instantaneous image velocities or discrete image displacements[84].

The analysis of optical flow is studied on the heart wall, it can be estimated over successive images corresponding to a certain cardiac cycle, as patterns of apparent motion of objects, or on the complete volumes.

The concept of optical flow was introduced by psychologist James J. Gibson in the 1940s who described the visual stimulus provided to animals moving through the world [85], and Horn and Schunck [86] showed an analysis of differential approximation of optical flow and how to determine it.

The method for motion estimation used in this thesis was developed by Ernesto Moya et al [8]. It takes advantage of a differential method in combination with the Hermite Transform. The model is based on Papenberg's work [87], who assumes a motion smoothed flow, that incorporates image operators within its functional, such as Laplacian derivatives. Instead of these derivatives, the Hermite descriptors are employed on a multiresolution basis for larger displacements. Let $L(x, y, t)$ be an image sequence where x, y represent image coordinates on a domain Ω , and $t \in [0, \tau]$ is used to denote time. Let u and v be a pixel displacement in the (x, y) position between one image on

time t and another image on time $t + 1$. Now the following relations can be defined:

$$\begin{aligned} W &: (u, v, 1)^T; & |\nabla W|^2 &= |\nabla u|^2 + |\nabla v|^2; & |\nabla_3 W|^2 &= |\nabla_3 u|^2 + |\nabla_3 v|^2 \\ \nabla_u &= (u_x, u_y)^T; & \nabla_{3u} &= (u_x, u_y, u_t)^T; & \Delta_u &= (u_{xx}, u_{yy})^T \\ X &= (x, y, t)^T; & L_* &= \frac{\partial L}{\partial_*}; & \nabla_3 L &= (L_x, L_y, L_t) \end{aligned} \quad (6.1)$$

Optical flow estimation is determined by the next characteristics that includes the Hermite Transform:

- A constant intensity constraint, that considers linear displacements of the studied object. It includes the zero order coefficient of the Hermite transform L_{00} .
- A constant gradient constraint, for the case of non constant intensity between one image and the next one. For this term the steered HCs are used $l_{n,\theta}$ where $n = 1, 2, \dots, N$ order, and θ is the maximum energy angle for position (x, y) .
- A smoothness constraint, that assumes the apparent speed of the intensity pattern to fluctuate smoothly, in other words, adjacent points of the objects have similar velocities. This constraint assumes a penalization function ψ for abrupt motion changes, and ∇ is the gradient operator that makes use of the Hermite transform once more.

For more information refer to Moya et al [8]. An energy functional for the optical flow, including Hermite Transform, is defined as:

$$E(u, v) = \int_{\Omega} \psi \left(|L_0(X + W) - L_0(X)|^2 + \gamma |l_{n,\theta}(X + W) - l_{n,\theta}(X)|^2 \right) dX + \alpha \int_{\Omega} \psi \left(|\nabla u|^2 + |\nabla v|^2 \right) dX \quad (6.2)$$

where γ and α are weight parameters for the steered Hermite coefficients, and ψ is an optimization function of the norm l^1 . This energy function is minimized through variational calculus, resulting in an iterative equation. This result contains the specific motion vectors. Figure 6.2 shows some results of motion estimation obtained from the left ventricle.

6.3 Heart Failure example

Figure 6.3 presents an initial test on a patient with infarction on the anterior wall. Note that the wall does not contract and expand as much as the rest of the myocardial tissue. In this case, the FLS/HCs algorithm achieved the best performance to segment epicardium and endocardium. From both segmentations the cardiomyopathy is clear, thickness of the anterior ventricular wall remains approximately constant along the cardiac cycle.

Adding the previous segmentation results to the optical flow, we obtain images shown in Figure 6.4.

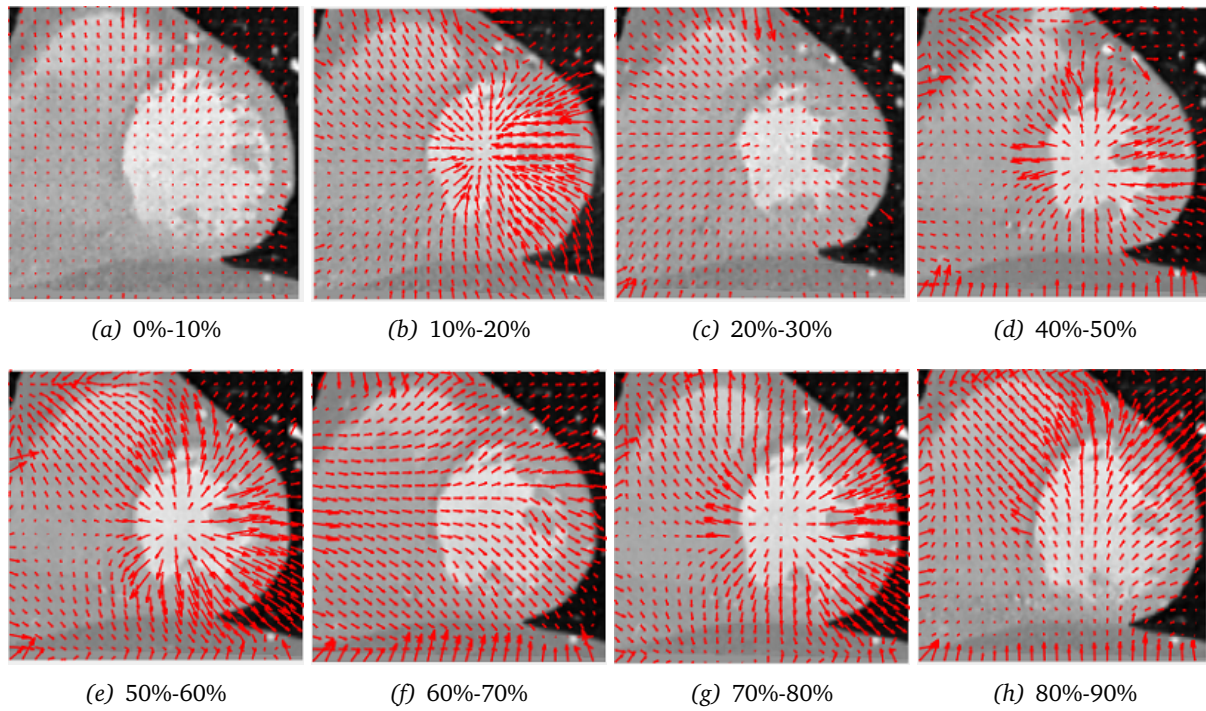


Figure 6.2: Motion estimation in one cardiac cycle going from systole to diastole.

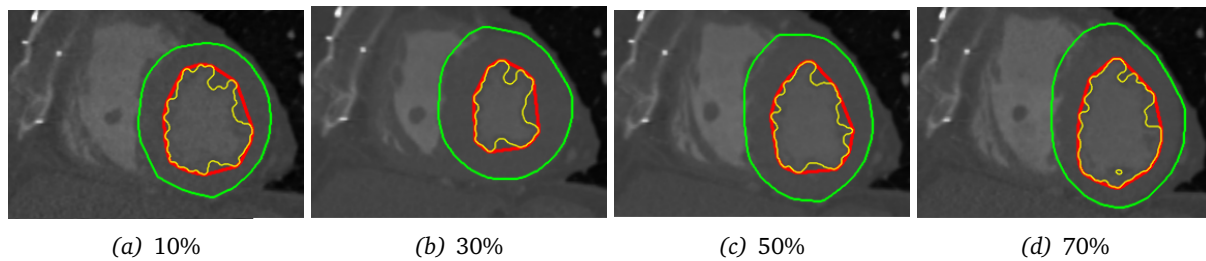


Figure 6.3: Segmentation of endocardium (red), epicardium (green) and papillary muscles (yellow) of a patient with infarction, using FLS/HCs at different percentages of the cardiac cycle.

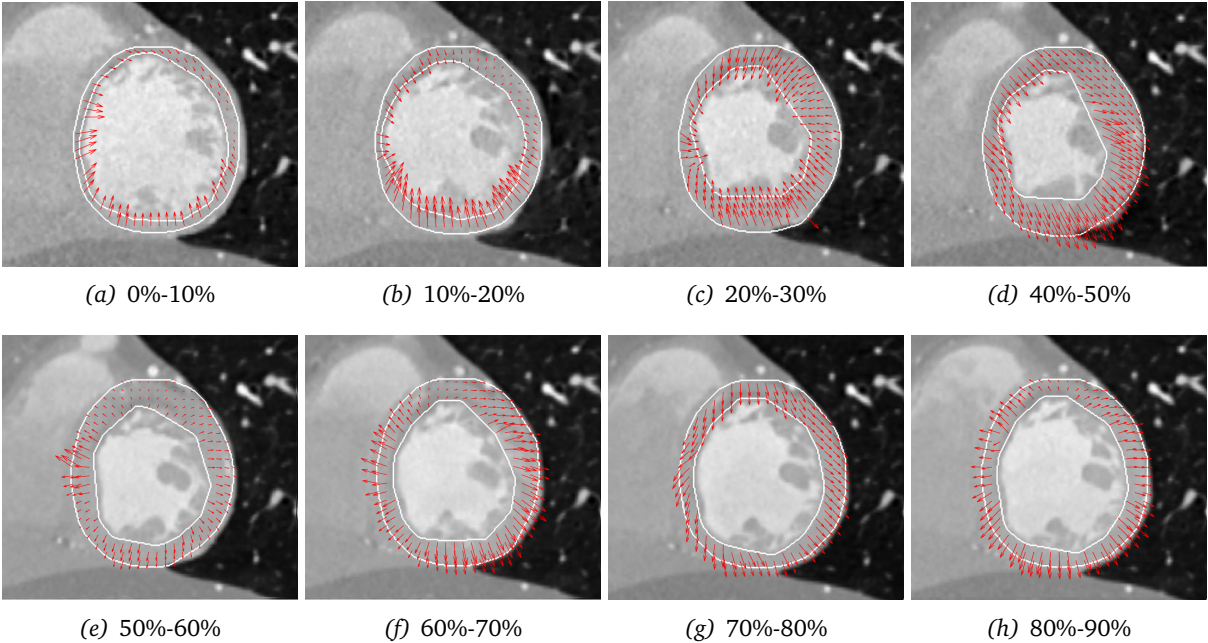


Figure 6.4: Segmentation of cardiac muscle with overlaid motion estimation, going from systole to diastole.

7

Conclusions

In the last years medical image segmentation has had a considerable development, and a large variety of methods have been proposed, many of them based on deformable models .

Several techniques that have being developed for human organ segmentation include those based on atlases, deformable models, pixel classification, region and edge detectors, and active shape models. Being some of the most used active contours and deformable models. However, most of these methods are mainly focused on MRI technology. On the other hand CT has been shown to be an affordable technique with good image quality results and despite it does not have the same image resolution as in the case of MRI. CT technology is being constantly improved in order to get better image resolution in time and space.

This document presented new advances in image segmentation based on deformable models, introducing textural cues, such as LBPs and the Hermite transform.

ASMs and deformable models based on level sets, especially the Chan Vesse algorithm and the Fast Level set segmentation were used. In the case of ASMs we used two different image modalities, namely MRI, to segment midbrain, and CT to segment the heart's left ventricle. In the case of the left ventricle we tested ASMs, Chan Vesse and Fast Level set methods. It is important to note that the image quality of the heart's left ventricle varies widely between human studies. In some scans the epicardium is hardly visible due to noise or smoothing.

In both cases the new methods included local textural information given by LBPs and HCs, and this information was incorporated in the segmentation algorithms to create various schemes. The performance of the methods was tested with common metrics such as Hausdorff distance and Dice

index. Moreover a new evaluation metric based on ray feature distances was introduced.

In the case of midbrain segmentation the accuracy of the MR images improved in a visible way when LBP textural information was included. The LBP + ASM approaches were implemented in a semiautomatic method for the left ventricle on the short axis view through the cardiac cycle. The level set method evolves an active contour and includes texture descriptors as extra components of an image vector. The objective is to improve the boundary search by adding texture descriptors and enhance the performance.

In the case of left ventricle's CT images, a semi-automatic segmentation method was implemented for the short axis view throughout the cardiac cycle. Two approaches are presented using the steered Hermite transform as a Human Vision model. The first one takes the HT as a texture descriptor that performs a decomposition of the image into visual patterns, relevant to the human vision system. These descriptors were added to the level set Chan Vese vector-value algorithm. The results achieved with the Hermite filters were more precise since they detected boundaries even in the presence of noise. This study demonstrates that the proposed image segmentation algorithm accurately quantifies clinically relevant parameters such as blood volume with minimal user input. Other texture descriptors like LBPs, however, generate a lot of information and prevent the algorithm from converging to a well defined contour. This proposal detects not only endocardial contours but also the papillary muscles.

In a second study, various approaches were tested. The performance of two types of deformable models was explored: Active shape models and level sets. The main contribution of this second approach is the inclusion of Hermite features and local information in order to improve the segmentation performance, especially when dealing with noisy images and lack of contrast.

The automatic localization used for the left ventricle, helped improve the ASM results. The methods show better accuracy when adding the HCs, in the case of endocardium segmentation. For the epicardium the AMSs and Fast level set methods present an evident accuracy increase when adding the HCs.

The segmentation schemes of the left ventricle presented in this work contribute to the understanding of complex heart dynamics. The results obtained resemble manual clinical delineations in CT imaging and prove that the methods proposed here may help reduce bias in diagnosis and treatment procedures. The joint approach FLS/HCs is a reliable option for segmenting LV, because it is able to differentiate between endocardium and epicardium borders. Another advantage of this approach is the fact that it does not need previous training.

In the last part of this paper, a novel method to assess contour-based segmentation called Ray Feature error is introduced. The results provided by Ray Feature error in epicardium and endocardium segmentation are consistent with the results provided by Dice index and Hausdorff distance (see Fig. 5.22 and Fig. 5.23). In addition, two synthetic cases where Dice index and Hausdorff distance fail are presented, whereas Ray Feature error rates segmentation performance in a better way. Ray Feature error represents a simple way to estimate segmentation error in a

range [0, 1). Since the error is anywhere between zero and one, it provides an estimation of its magnitude. RFE measures errors along a circular path using discrete steps; therefore, it is also suited to measure segmentation errors on directions of specific interest.

It is worth to mention about a second accepted paper that incorporates both applications of this thesis [88], it includes midbrain and heart's left ventricle segmentation techniques, most of them already mentioned but also adds level set segmentation with Chan-Vese and Hermite's approach.

Future work must be done with tasks not covered in this study, such as experimentation including more patients with different pathologies and segmentation schemes for the epicardial wall as well. Also the estimation of quantitative LV parameters, like ejection percentage on the whole volume are essential tasks for all imaging techniques and significant supporting physician decisions. More over an extension of the segmentation algorithms to 3D is very relevant.

A

Appendix

A.1 Ray Feature error

Since active contours have become a popular technique frequently used in image segmentation, it is necessary to use a metric that assesses their performance objectively. Here, we propose a fast and solid yet simple method for quantitative evaluation of contour-based segmentation called Ray Feature error (RFE) (see Figure A.1). RFE is based on the original proposal of ray features [75] where the authors computed four image features to characterize irregular shapes: distance difference, distance feature, orientation, and norm feature.

RFE permits the measurement of shape similarities between two overlapping objects as follows:

- Given two closed objects A and B , we define the location C_{AB} as the common centroid of both objects.
- It is possible to calculate the distance from the location p in A to the nearest border in the direction of θ as follows:

$$dA_{\theta}(p, \theta) = \|f(A, p, \theta) - p\| \quad (\text{A.1})$$

where $f(A, p, \theta)$ returns to the location of the nearest border to p in A in the direction of θ and $\|\bullet\|$ is the Euclidean norm.

- The local error between two objects in the direction of θ is obtained as the absolute value of

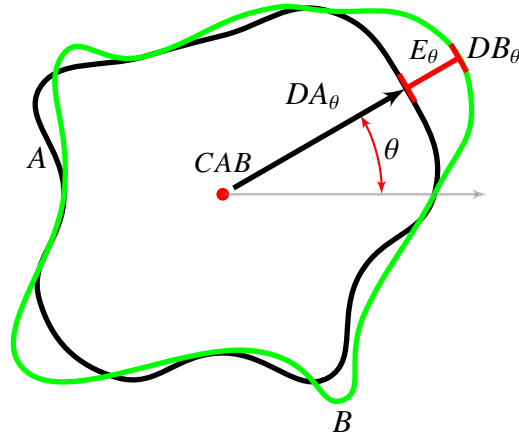


Figure A.1: Ray Feature error (RFE). Given two closed overlapping objects, RFE measures similarities between them by computing and adding E_θ with $\theta = \{0, \dots, 2\pi\}$.

the difference amongst the distances:

$$E(AB)_\theta = |dA_\theta - dB_\theta| \quad (\text{A.2})$$

- Finally, RFE is computed as:

$$RFE(A, B) = \frac{\sum_\theta |dA_\theta - dB_\theta|}{DA + DB} \quad (\text{A.3})$$

where $DX = \sum_\theta dX_\theta$.

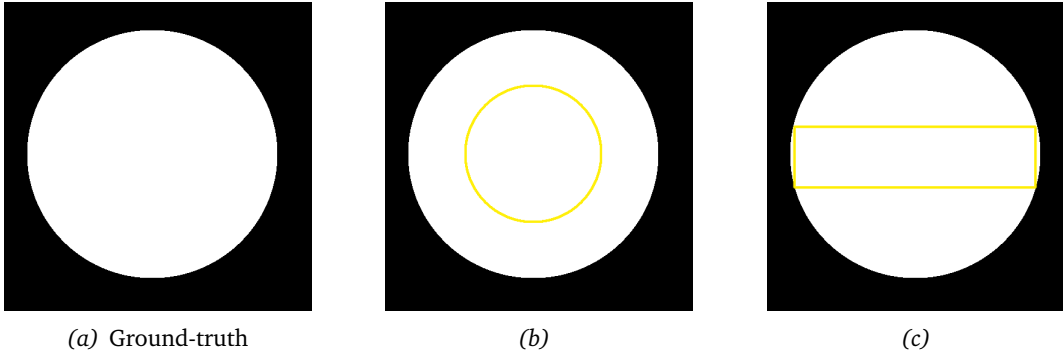
RFE represents a simple and fast way to compare two overlapping closed shapes. It varies within the range $[0, 1)$ and $RFE(A, B) = 0$ if and only if A and B have the closure, $A = B$.

A.1.1 METRIC COMPARISON

Although many methods for left ventricle segmentation have been developed during recent years, the majority of the heart segmentation methods in the literature remain difficult to compare. Furthermore, one of the difficulties when working with medical imaging is the large inter-observer variability even when the observers are considered to be experts.

An objective evaluation is a crucial step to ascertain if the results are acceptable from a medical point of view and is intended to indicate the degree of reliability of the method. Thus, a relevant evaluation method must be able to detect small differences between two segmentation procedures.

Dice index (DI) belongs to a class of region-based evaluation methods and is defined as twice



Segmentation comparison of synthetic shapes. Ground truth is in white and segmentations in yellow. Regions within yellow contours are different in shape but have the same area. Note that in this case, Dice index is not a suitable criterion because the index is the same in both cases.

| Method | (b) | (c) |
|--------------------|-----------------|--------|
| Ray Feature Error | 0.2927 | 0.3529 |
| Hausdorff distance | 104.6614 | 160 |
| Dice index | 0.4588 | 0.4588 |

Figure A.2: Two examples of segmentation. Bold values represent the best results and letters in parentheses represent the corresponding case.

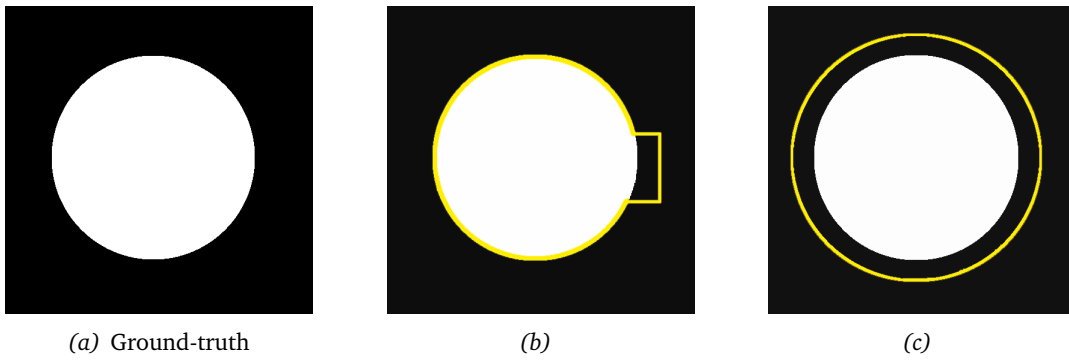
the intersection of two sets X and Y divided by the sum of the cardinality of the two sets, as follows:

$$DI = \frac{2|X \cap Y|}{|X| + |Y|} \quad (\text{A.4})$$

DI is equal to 1 when the two sets are exactly the same, and 0 when the two sets are completely different. However, since it is a metric based on areas, a limitation of this criterion is that several segmentations can arrive at the same result, see Figure A.2.

On the other hand, Hausdorff distance (HD) is a standard metric that measures the distance between two contours A and B . The measurement is the maximum distance among all the minimum distances between A and B . Hausdorff represents a pseudo-distance because $HD(A, B) \neq HD(B, A)$. It therefore, computes the distances twice and since it only considers a maximum value, it is sensitive to local variations, see Figure A.3. Another disadvantage is that the measurement is not bounded so we cannot easily estimate the performance of a segmentation.

We believe our proposal Ray Feature error reflects the quality of the segmentation better and overcomes the previous issues related with DI and HD. Furthermore, it is a real distance and is bounded $[0, 1)$ where 0 represents perfect segmentation. Therefore we can achieve a more accurate understanding of the performance of the segmentation.



Summary of contour comparisons. Since Hausdorff distance is define as the maximum of the minimum distances between two sets of points, it fails in this example. Bold values represent better results. Letters in parentheses represent the corresponding case.

| Method | (b) | (c) |
|--------------------|---------------|---------|
| Ray feature error | 0.0246 | 0.0990 |
| Hausdorff distance | 39.0128 | 39.0128 |
| Dice index | 0.9737 | 0.8026 |

Figure A.3: Two examples of segmentation with the ground-truth in white and the resulted segmentations in yellow. Note that in both cases, Hausdorff distance is the same.

Bibliography

- [1] Kang, D., Woo, J., Slomka, P. J., Dey, D., Germano, G., and Jay Kuo, C.-C., “Heart chambers and whole heart segmentation techniques: Review,” *Journal of Electronic Imaging* **21**(1), 010901–1–010901–16 (2012).
- [2] Petitjean, C. and Dacher, J.-N., “A review of segmentation methods in short axis cardiac MR images,” *Medical Image Analysis* **15**(2), 169–184 (2011).
- [3] Cerqueira, M. D., Weissman, N. J., Dilsizian, V., Jacobs, A. K., Kaul, S., Laskey, W. K., Pennell, D. J., Rumberger, J. A., Ryan, T., and Verani, M. S., “Standardized myocardial segmentation and nomenclature for tomographic imaging of the heart,” *Circulation* **105**(4), 539–542 (2002).
- [4] Faghih Roohi, S. and Aghaeizadeh Zoroofi, R., “4D statistical shape modeling of the left ventricle in cardiac MR images,” *International Journal of Computer Assisted Radiology and Surgery* **8**(3), 335–351 (2013).
- [5] Ma, F., Liu, J., Wang, B., and Duan, H., “Automatic segmentation of the full heart in cardiac computed tomography images using a haar classifier and a statistical mode,” *Journal of Medical Imaging and Health Informatics* **6**(5), 1298–1302 (2016).
- [6] Bugdol, M. N. and Pietka, E., “Mathematical model in left ventricle segmentation,” *Computers in Biology and Medicine* **57**(C), 187–200 (2015).
- [7] Antunes, S., Esposito, A., Palmisano, A., Colantoni, C., Cerutti, S., and Rizzo, G., “Cardiac multi-detector CT segmentation based on multiscale directional edge detector and 3D level set,” *Annals of Biomedical Engineering* **44**(5), 1487–1501 (2016).
- [8] Moya-Albor, E., Escalante-Ramírez, B., and Vallejo, E., “Optical flow estimation in cardiac {CT} images using the steered hermite transform,” *Signal Processing: Image Communication* **28**(3), 267 – 291 (2013).
- [9] Engel, K. and Toennies, K., “Segmentation of the midbrain in transcranial sonographies using a two-component deformable model,” *Annals of the BMVA* **2009**, 1–13 (2009).
- [10] Chen, J., Khan, A. R., Denk, C., Galley, S., Rauscher, A., McKeown, M., and Beg, M., “Multi-structure registration allows group interpretation of midbrain iron content in Parkinson’s,” in [16th Annual Meeting of the Organization for Human Brain Mapping], (2010).
- [11] Kier, C., Cyrus, C., Seidel, G., Hofmann, U. G., and Aach, T., “Segmenting the substantia nigra in ultrasound images for early diagnosis of Parkinson’s disease,” *International Journal of Computer Assisted Radiology and Surgery* **2**, S83–S85 (June 2007).

BIBLIOGRAPHY

- [12] Sørensen, L., Shaker, S., and de Bruijne, M., “Quantitative analysis of pulmonary emphysema using local binary patterns,” *IEEE Transactions on Medical Imaging* **29**(2), 559–569 (2010).
- [13] Becker, B. G., Cosío, F. A., Huerta, M. E. G., and Benavides-Serralde, J. A., “Automatic segmentation of the cerebellum of fetuses on 3D ultrasound images, using a 3D point distribution model,” in [*Annual International Conference of the IEEE Engineering in Medicine and Biology Society.*], 4731–4 (2010).
- [14] Kroon, D. J., *Segmentation of the Mandibular Canal in Cone-Beam CT Data*, PhD thesis, University of Twente (December 2011).
- [15] Kratky, J. and Kybic, J., “Three-dimensional segmentation of bones from CT and MRI using fast level sets,” in [*Proc. SPIE Medical Imaging*], **6914**, 691447–1–691447–10 (2008).
- [16] Kronman, A. and Joskowicz, L., “A geometric method for the detection and correction of segmentation leaks of anatomical structures in volumetric medical images,” *International Journal of Computer Assisted Radiology and Surgery* **11**(3), 369–380 (2016).
- [17] Suri, J., Liu, K., Singh, S., Laxminarayan, S., Zeng, X., and Reden, L., “Shape recovery algorithms using level sets in 2-D/3-D medical imagery: a state-of-the-art review,” *Information Technology in Biomedicine, IEEE Transactions on* **6**(1), 8–28 (2002).
- [18] Kohlberger, T., Uzunbaş, M., Alvino, C., Kadir, T., Slosman, D., and Funka-Lea, G., “Organ segmentation with level sets using local shape and appearance priors,” in [*Medical Image Computing and Computer-Assisted Intervention (MICCAI)*], Yang, G.-Z., Hawkes, D., Rueckert, D., Noble, A., and Taylor, C., eds., *Lecture Notes in Computer Science* **5762**, 34–42, Springer Berlin Heidelberg (2009).
- [19] Cootes, T. F., Taylor, C. J., Cooper, D. H., and Graham, J., “Active shape models: their training and application,” *Comput. Vis. Image Underst.* **61**(1), 38–59 (1995).
- [20] Osher, S. and Paragios, N., [*Geometric Level Set Methods in Imaging, Vision, and Graphics*], Springer-Verlag New York, Inc., Secaucus, NJ, USA (2003).
- [21] Caselles, V., Kimmel, R., and Sapiro, G., “Geodesic active contours,” *Int. J. Comput. Vision* **22**(1), 61–79 (1997).
- [22] Chan, T. and Vese, L., “Active contours without edges,” *IEEE Transactions on Image Processing* **10**(2), 266–277 (2001).
- [23] Gao, S. and Bui, T., “Image segmentation and selective smoothing by using Mumford-Shah model,” *IEEE Transactions on Image Processing* **14**(10), 1537–1549 (2005).
- [24] Huang, C.-L., “Shape-based level set method for image segmentation,” in [*Ninth International Conference on Hybrid Intelligent Systems*], **1**, 243–246 (2009).
- [25] Chan, T. F., Sandberg, B. Y., and Vese, L. A., “Active contours without edges for vector-valued images,” *Journal of Visual Communication and Image Representation* **11**, 130–141 (2000).
- [26] Paragios, N. and Deriche, R., “Geodesic active regions: A new framework to deal with frame partition problems in computer vision,” *Journal of Visual Communication and Image Representation* **13**(1-2), 249–268 (2002).

- [27] Brox, T., Rousson, M., Deriche, R., and Weickert, J., “Colour, texture, and motion in level set based segmentation and tracking,” *Image and Vision Computing* **28**(3), 376–390 (2010).
- [28] Olveres, J., Nava, R., Escalante-Ramírez, B., Cristóbal, G., and García-Moreno, C. M., “Midbrain volume segmentation using active shape models and LBPs,” in [*Proc. SPIE Europe*], **8856**, 88561F–1–88561F–11 (2013).
- [29] Abu-gharbieh, R., Hamarneh, G., and Gustavsson, T., “Review - active shape models - part ii: Image search and classification,” in [*In Proc. Swedish Symposium on Image Analysis*], 129–132 (1998).
- [30] Cootes, T. F., Edwards, G. J., and Taylor, C. J., “Active appearance models,” in [*5th European Conference on Computer Vision, Proceedings, Volume II*], Burkhardt, H. and Neumann, B., eds., 484–498, Springer Berlin Heidelberg (1998).
- [31] Hum, Y., [*Segmentation of Hand Bone for Bone Age Assessment*], SpringerBriefs in Applied Sciences and Technology, Springer Singapore (2013).
- [32] Osher, S. and Sethian, J. A., “Fronts propagating with curvature-dependent speed: Algorithms based on hamilton-jacobi formulations,” *J. Comput. Phys.* **79**, 12–49 (Nov. 1988).
- [33] Mumford, D. and Shah, J., “Optimal approximations by piecewise smooth functions and associated variational problems,” *Communications on Pure and Applied Mathematics* **42**(5), 577–685 (1989).
- [34] Li, C., Kao, C., Gore, J., and Ding, Z., “Implicit active contours driven by local binary fitting energy,” in [*Proceedings of IEEE Conference on Computer Vision and Pattern Recognition (CVPR)*], 1–7 (2007).
- [35] Houhou Nawal, Thiran Jean-Philippe, B. X., “Fast texture segmentation based on semi-local region descriptor and active contour,” *Numerical Mathematics: Theory , Methods and Applications* **2**, 445–468 (2009).
- [36] Bradski, G. and Kaehler, A., [*Learning OpenCV: Computer Vision in C++ with the OpenCV Library*], O’Reilly Media, Inc., 2nd ed. (2013).
- [37] Silván-Cárdenas, J. L. and Escalante-Ramírez, B., “The multiscale Hermite transform for local orientation analysis,” *IEEE Transactions on Image Processing.* **15**(5), 1236–1253 (2006).
- [38] Martens, J.-B., “The Hermite transform-theory,” *IEEE Transactions on Acoustics, Speech and Signal Processing* **38**(9), 1595–1606 (1990).
- [39] Lindeberg, T., “A computational theory of visual receptive fields,” *Biological Cybernetics* **107**(6), 589–635 (2013).
- [40] Young, R., Lesperance, R., and Meyer, W. W., “The gaussian derivative model for spatial-temporal vision: I. cortical model,” *Spatial Vision* **14**(3), 261–319 (2001).
- [41] Martens, J.-B., “The Hermite transform-applications,” *IEEE Transactions on Acoustics, Speech and Signal Processing* **38**(9), 1607–1618 (1990).
- [42] Sakitt, B. and Barlow, H., “A model for the economical encoding of the visual image in cerebral cortex,” *Biological Cybernetics* **43**(2), 97–108 (1982).

BIBLIOGRAPHY

- [43] Freeman, W. T. and Adelson, E. H., “The design and use of steerable filters,” *IEEE Transactions on Pattern Analysis and Machine Intelligence* **13**, 891–906 (1991).
- [44] Yang, B., Flusser, J., and Suk, T., “Steerability of hermite kernel,” *International Journal of Pattern Recognition and Artificial Intelligence* **27**(4), 1354006 (2013).
- [45] Estudillo-Romero, A. and Escalante-Ramírez, B., “Rotation-invariant texture features from the steered Hermite transform,” *Pattern Recognition Letters* **32**(16), 2150–2162 (2011).
- [46] van Dijk, A. M. and Martens, J.-B., “Image representation and compression with steered Hermite transforms,” *Signal Processing* **56**(1), 1–16 (1997).
- [47] Berretta, N., Bernardi, G., and Mercuri, N. B., “Firing properties and functional connectivity of substantia nigra pars compacta neurones recorded with a multi-electrode array in vitro,” *The Journal of Physiology* **588**(10), 1719–1735 (2010).
- [48] Damier, P., Hirsch, E. C., Agid, Y., and Graybiel, A. M., “The substantia nigra of the human brain: I. Nigrosomes and the nigral matrix, a compartmental organization based on calbindin D28K immunohistochemistry,” *Brain* **122**(8), 1421–1436 (1999).
- [49] Sakalauskas, A., Lukosevicius, A., and Lauckaitė, K., “Transcranial echoscopy for diagnostic of Parkinson disease: technical constraints and possibilities,” *Ultragarsas* **65**, 47–50 (2010).
- [50] Shen, L., Farid, H., and McPeck, M. A., “Modeling three-dimensional morphological structures using spherical harmonics,” *Evolution* **63**(4), 1003–1016 (2009).
- [51] Ojala, T., Pietikainen, M., and Harwood, D., “Performance evaluation of texture measures with classification based on Kullback discrimination of distributions,” in [*Proceedings of the 12th International Conference on Pattern Recognition- Conference A: Computer Vision Image Processing (IAPR)*], **1**, 582–585 (1994).
- [52] Ojala, T., Pietikäinen, M., and Mäenpää, T., “Multiresolution gray-scale and rotation invariant texture classification with local binary patterns,” *IEEE Trans. Pattern Anal. Mach. Intell.* **24**(7), 971–987 (2002).
- [53] Ma, Y., “Number local binary pattern: An extended local binary pattern,” in [*2011 International Conference on Wavelet Analysis and Pattern Recognition(ICWAPR)*], 272 –275 (2011).
- [54] Zabih, R. and Woodfill, J., “Non-parametric local transforms for computing visual correspondence,” in [*Proceedings of the third European conference on Computer Vision (Vol.II)*], 151–158, Springer-Verlag New York, Inc., Secaucus, NJ, USA (1994).
- [55] Keomany, J. and Marcel, S., “Active shape models using local binary patterns,” tech. rep., IDIAP (2006).
- [56] Schoepf, U. J., Becker, C. R., Hofmann, L. K., and Kent, Y. E., “Multidetector-row CT of the heart,” *Radiologic Clinics* **42**(3), 635–649 (2004).
- [57] Fischbach, R., “Cardiac and cardiothoracic anatomy in CT,” in [*Multi-slice and Dual-source CT in Cardiac Imaging*], Ohnesorge, B., Flohr, T., Becker, C., Knez, A., and Reiser, M., eds., 23–39, Springer Berlin Heidelberg (2007).

- [58] Halliburton, S., Arbab-Zadeh, A., Dey, D., Einstein, A. J., Gentry, R., George, R. T., Gerber, T., Mahesh, M., and Weigold, W. G., “State-of-the-art in CT hardware and scan modes for cardiovascular CT,” *Journal of Cardiovascular Computed Tomography* **6**(3), 154–163 (2012).
- [59] Gibbons, R. J., “Noninvasive diagnosis and prognosis assessment in chronic coronary artery disease,” *Circulation: Cardiovascular Imaging* **1**, 257–269 (2008).
- [60] Bresson, X., Esedoglu, S., Vanderghenst, P., Thiran, J.-P., and Osher, S., “Fast global minimization of the active contour/snake model,” *Journal of Mathematical Imaging and Vision* **28**(2), 151–167 (2007).
- [61] Lu, Y.-L., Connelly, K. A., Dick, A. J., Wright, G. A., and Radau, P. E., “Automatic functional analysis of left ventricle in cardiac cine MRI,” *Quantitative Imaging in Medicine and Surgery* **3**(4) (2013).
- [62] Turco, D. and Corsi, C., [*Advanced PDE-based Methods for Automatic Quantification of Cardiac Function and Scar from Magnetic Resonance Imaging. Series in Computer Vision in Medical Imaging. Computer Vision: Volume 2.*], World Scientific Publishing Company, University of Massachusetts, USA (2013).
- [63] Juan J. Cerrolaza, A. V. and Cabeza, R., [*On Hierarchical Statistical Shape Models with application to Brain MRI. Series in Computer Vision in Medical Imaging. Computer Vision*], vol. 2, World Scientific Publishing Company, University of Massachusetts, USA (2013).
- [64] Kawa, J. and Pietka, E., “Kernelized fuzzy c-means method in fast segmentation of demyelination plaques in multiple sclerosis,” in [*29th International Conference of the IEEE Engineering in Medicine and Biology Society.*], 5616–5619, IEEE (2007).
- [65] Dolz, J., Kirişli, H. A., Fechter, T., Karnitzki, S., Oehlke, O., Nestle, U., Vermandel, M., and Massoptier, L., “Interactive contour delineation of organs at risk in radiotherapy: Clinical evaluation on NSCLC patients,” *Medical Physics* **43**(5), 2569–2580 (2016).
- [66] Olveres, J., Nava, R., Moya-Albor, E., Escalante-Ramírez, B., Brieva, J., Cristóbal, G., and Vallejo, E., “Texture descriptor approaches to level set segmentation in medical images,” in [*Proc. SPIE Europe*], **9138**, 91380J–91380J–12 (2014).
- [67] Wu, Y. and Shen, J., “Properties of orthogonal Gaussian-Hermite moments and their applications,” *EURASIP Journal on Advances in Signal Processing* **2005**(4), 1–12 (2005).
- [68] Rivero-Moreno, C. J. and Bres, S., “Texture feature extraction and indexing by Hermite filters,” in [*Proceedings of the 17th International Conference on Pattern Recognition*], **1**, 684–687 (2004).
- [69] Olveres, J., Nava, R., Escalante-Ramírez, B., Vallejo, E., and Kybic, J., “Left ventricle hermite-based segmentation,” *Computers in Biology and Medicine* **87**, 236–249 (05 2017).
- [70] Barba-J, L., Moya-Albor, E., Escalante-Ramírez, B., Brieva, J., and Vallejo Venegas, E., “Segmentation and optical flow estimation in cardiac ct sequences based on a spatiotemporal pdm with a correction scheme and the hermite transform,” *Computers in Biology and Medicine* **69**, 189–202 (Feb. 2016).

BIBLIOGRAPHY

- [71] Liu, L., Yang, B., Fieguth, P., Yang, Z., and Wei, Y., “BRINT: A binary rotation invariant and noise tolerant texture descriptor,” in [20th IEEE International Conference on Image Processing (ICIP)], 255–259 (2013).
- [72] Natalia A. Trayanova, P. M. B., “Cardiac arrhythmias: Mechanistic knowledge and innovation from computer models,” in [Modeling the Heart and the Circulatory System], Gellman, M. D. and Turner, J. R., eds., 14, 27–29, Springer International Publishing (2015).
- [73] Nava, R., Cristóbal, G., and Escalante-Ramírez, B., “A comprehensive study of texture analysis based on local binary patterns,” in [Proc. SPIE 8436, Optics, Photonics, and Digital Technologies for Multimedia Applications II], 84360E–1–84360E–12 (2012).
- [74] Pele, O. and Werman, M., “The quadratic-chi histogram distance family,” in [Computer Vision – ECCV 2010: 11th European Conference on Computer Vision, Proceedings, Part II], 749–762, Springer Berlin Heidelberg (2010).
- [75] Smith, K., Carleton, A., and Lepetit, V., “Fast ray features for learning irregular shapes,” in [IEEE 12th International Conference on Computer Vision], 397–404 (2009).
- [76] World Health Organization (WHO), “Cardiovascular diseases (CVDs), fact sheet,” (2015). Accessed: 2016-04-20.
- [77] Ye, S., “Acute myocardial infarction,” in [Encyclopedia of Behavioral Medicine], Gellman, M. D. and Turner, J. R., eds., 27–29, Springer New York, New York, NY (2013).
- [78] Centers for Disease Control and Prevention, “Heart failure fact sheet,” (2016). Accessed: 2017-01-12.
- [79] Mozaffarian, D., Benjamin, E. J., Go, A. S., Arnett, D. K., Blaha, M. J., Cushman, M., Das, S. R., de Ferranti, S., Després, J.-P., Fullerton, H. J., Howard, V. J., Huffman, M. D., Isasi, C. R., Jiménez, M. C., Judd, S. E., Kissela, B. M., Lichtman, J. H., Lisabeth, L. D., Liu, S., Mackey, R. H., Magid, D. J., McGuire, D. K., Mohler, E. R., Moy, C. S., Muntner, P., Mussolino, M. E., Nasir, K., Neumar, R. W., Nichol, G., Palaniappan, L., Pandey, D. K., Reeves, M. J., Rodriguez, C. J., Rosamond, W., Sorlie, P. D., Stein, J., Towfighi, A., Turan, T. N., Virani, S. S., Woo, D., Yeh, R. W., and Turner, M. B., “Heart disease and stroke statistics—2016 update,” (2016).
- [80] Wong, T. C. and Soman, P., “Imaging in the evaluation of the patient with new-onset heart failure,” *Current Cardiovascular Imaging Reports* 5(3), 167–172 (2012).
- [81] Ventura-Clapier, R., [Encyclopedia of Exercise Medicine in Health and Disease], ch. Cardiomyopathies, 175–175, Springer Berlin Heidelberg (2012).
- [82] Leschka, S., Waelti, S., and Wildermuth, S., “Principles of CT imaging,” in [Cardiac CT and MR for Adult Congenital Heart Disease], Saremi, F., ed., Springer, New York (2014).
- [83] Moschetti, K., Muzzarelli, S., Pinget, C., Wagner, A., Pilz, G., Wasserfallen, J., Schulz-Menger, J., Nothnagel, D., Dill, T., Frank, H., Lombardi, M., Bruder, O., Mahrholdt, H., and Schwitzer, J., “Cost evaluation of cardiovascular magnetic resonance versus coronary angiography for the diagnostic work-up of coronary artery disease: Application of the European Cardiovascular Magnetic Resonance registry data to the German, United Kingdom, Swiss, and United States health care systems,” *Journal of Cardiovascular Magnetic Resonance* 14(1), 35 (2012).

- [84] S.S., B. and J.L, B., “The computation of optical flow,” *ACM Computing Surveys* **27**(3), 433–467 (1995).
- [85] Gibson, J. J., “The perception of the visual world,” *The American Journal of Psychology* **64**, 622–625 (1951).
- [86] B. K. Horn, B. G. S., “Determining optical flow,” *Artificial Intelligence* **1**(17), 185–203 (1981).
- [87] Papenberg, N., Bruhn, A., Brox, T., Didas, S., and Weickert, J., “Highly accurate optic flow computation with theoretically justified warping.,” *International Journal of Computer Vision* **67**(2), 141–158 (2006).
- [88] Olveres, J., Carbajal-Degante, E., Escalante-Ramírez, B., Vallejo, E., and García-Moreno, C. M., “Deformable models for segmentation based on local analysis,” *Accepted at Mathematical Problems in Engineering* (2017).